Atomistic Modeling for CO_2 Reduction Using Thermal, Plasma, and Electrocatalysis

by

Francis J. Doherty

A dissertation submitted in partial fulfillment
of the requirements for the degree of
Doctor of Philosophy
(Chemical Engineering)
in the University of Michigan
2022

Doctoral Committee:

Assistant Professor Bryan R. Goldsmith, Chair
Professor Suljo Linic
Assistant Professor Nirala Singh
Professor Paul Zimmerman

Francis Doherty

fdoherty@umich.edu

ORCID iD: 0000-0002-2648-8273

Dedication

For my loving family.

Their guidance, advice, and encouragement made this dissertation possible.

Acknowledgements

I would first like to acknowledge my committee members, who each gave invaluable advice toward the completion of this dissertation. My advisor, Prof. Bryan Goldsmith, has given an immeasurable amount of his time and effort across my PhD, from teaching me the early basics of density functional theory modeling, to the meetings spent designing our modeling experiments, to the countless revisions of each manuscript along the way. Prof. Nirala Singh gave a great deal of encouragement and criticism to make the message within my presentations as clear and accurate as possible, and always brought up a good point that was worth clarifying; Prof. Suljo Linic would always push me further to achieve my best and make sure that my research was aimed at the proper questions; and Prof. Paul Zimmerman made sure I knew the chemistry behind my modeling research and kept my work grounded in basic principles.

I would also like to thank all my lab members throughout my time at University of Michigan, Jacques Esterhuizen, Zixuan Wang, Sam Young, Isaiah Barth, Oluwatosin Ohiro, Ankit Mathanker, and Cameron Gruich. A special thank you goes to our post-doc Jin-Xun Liu who provided a great deal of knowledge and modeling expertise to our young lab. I also graciously appreciate all the undergraduate researchers that I have worked with, especially Eric Musa who had an undying passion for all things machine learning and brought that passion to every one of his projects.

Finally, I would like to thank all my friends and family. My community here in Ann Arbor has made every day a joy and brought the light of Christ into my life in a much deeper way by

their loving example and encouragement. My friends-for-life Cameron and Justin have kept me sane and laughing throughout my PhD years, from near or far. The time I have spent with them has always left a smile on my face. My loving mom and dad (Jere and Frank), have always made their unconditional love for me known, and I have never felt insecure in their support. My sister Meaghan always shows a loving interest in my research (even if the kids do always interrupt my explanation), and her whole family (Brian, Artie, Timmy, Charlie, Lucy, and Grace) bring so many wonderful and energetic experiences to my life. You have all supported me and encouraged me every step of the way.

Table of Contents

Dedication ii

Acknowledgements iii

List of Tables viii

List of Figures ix

Abstract xii

Chapter 1. Introduction....1

1.1 Motivation....1

1.2 Background....5

1.2.1 Dynamic Structural Changes of Nanoclusters and Single-Atom Catalysts....5

1.2.3 Influence of Coordination Environment Changes on Catalytic Performance....12

1.2.3 Catalytic CO_2 Reduction....16

1.2.3.1 Thermocatalytic CO_2 Reduction by Single Atoms and Nanoclusters....16

1.2.3.2 Plasma Enhanced Catalysis for CO_2 Reduction....19

1.2.3.3 Electrocatalytic CO_2 reduction....23

1.3. Research Goals....26

1.4 References....30

Chapter 2. Thermocatalytic Reverse Water Gas Shift Reaction via Rhodium Single-Atom Catalysts Compared to Nanoclusters....37

2.1 Introduction....37

2.2 Computational Methods.....41

2.3 Results and Discussion.....46

2.3.1 Atomically dispersed Rh_1 catalysts for rWGSR.....46

2.3.2 Effect of Nanocluster Size on rWGSR Selectivity.....56

2.4 Conclusions.....61

2.5 References.....63

Chapter 3. Modeling Plasma-Induced Surface Charge Effects on CO_2 Activation by Supported Single-Atom Catalysts.....71

3.1 Introduction.....71

3.2 Computational Methods.....74

3.3 Results and Discussion.....75

3.4 Conclusions.....87

3.5 References.....88

Chapter 4. Electrocatalytic CO_2 Conversion via Molecular Catalyst Cobalt Phthalocyanine.....92

4.1 Introduction.....92

4.2 Background.....95

4.3 Computational Methods.....102

4.4 Results and Discussion.....103

4.5 Conclusions.....107

4.6 References.....110

Chapter 5. Conclusion and Outlook.....114

5.1 Summary.....114

5.2 Extension of Current Research.....116

5.3 Catalyst Structure Explored Through Modeling and Machine Learning.....119

5.4 Final Remarks.....122

5.5 References.....123

List of Tables

Table 2-1. Elementary reaction steps for microkinetic models of $Rh_1/TiO_2(101)$, Rh_1OH/TiO_2 and Rh_1 near O_{3c}vac.....53

Table 3-1. CO_2 adsorption energies, CO_2 dissociation barriers, and Hirshfeld charges of M_1/CeO_2, M_1/TiO_2, and M_1/Al_2O_3.....86

List of Figures

Fig. 1-1. Surface site counts relative to particle size 4

Fig. 1-2. Illustration of three different driving forces for CO_2 reduction 5

Fig. 1-3. Reactant-induced disintegration of nanoclusters into single atoms 7

Fig. 1-4. Transformation between single atoms and nanoclusters 11

Fig. 1-5. Coordination environment changes in response to reactants and the effect on catalytic performance 14

Fig. 1-6. CO_2 reduction activity and selectivity comparison of single-atom and nanocluster catalysts 19

Fig. 1-7. Overview of the key mechanisms and species in the plasma and at the catalytic surface 20

Fig. 1-8. Plasma enhancement effect on catalytic reactions 22

Fig. 1-9. Illustrated depiction of CO_2 electrocatalytic methods 24

Fig. 1-10. Increased catalytic activity of CoPc-A due to less aggregation 25

Fig. 2-1. Illustration of the Rh/TiO_2 catalyst for CO_2 reduction 40

Fig. 2-2. Workflow summarizing the genetic algorithm for the global optimization of supported nanoclusters 43

Fig. 2-3. Rh_1/TiO_2 system geometries 47

Fig. 2-4. Experimental DRIFTS spectroscopy and DFT-predicted CO stretching frequencies under the harmonic approximation for $Rh_1(CO)_2$ systems 49

Fig. 2-5. DFT-predicted free-energy diagrams for reverse water gas shift reaction by (a) $Rh_1/TiO_2(101)$ and (b) $Rh_1OH/TiO_2(101)$ 51

Fig. 2-6. DFT-predicted free-energy diagrams for reverse water gas shift reaction by Rh_1 near O_{3c}vac.....53

Fig. 2-7. Microkinetic modeling results for reverse water gas shift reaction.....55

Fig. 2-8. Most stable configurations of Rh_x/TiO_2 (x = 1–8 atoms) with one CO adsorbed.....57

Fig. 2-9. Rh nanocluster characterization by Bader charge analysis.....58

Fig. 2-10. Binding energies (dashed lines) for gaseous species of interest (CO, H_2, CO_2) on Rh_x/TiO_2 (x = 1–8 atoms) 59

Fig. 2-11. Adsorption and dissociation of H_2 on Rh_1(CO) and Rh_2(CO) supported on $TiO_2(101)$ 61

Fig. 3-1. Model systems of atomically dispersed single atom catalysts (M_1) on different supports.....77

Fig. 3-2. Influence of surface charge on CO_2 binding energy on M_1/support systems.....79

Fig. 3-3. Charge analysis and projected density of states for CO_2 adsorbed on the single atom catalyst systems.....82

Fig. 3-4. Dissociation barrier for $*CO_2$ to *CO + *O for different M_1/support systems.....84

Fig. 3-5. Correlation between Hirshfeld charge, CO_2 adsorption energy, and CO_2 dissociation barrier.....85

Fig. 4-1. Branching mechanism of CO_2 reduction to CH_4, CH_3OH, or C_2H_4.....93

Fig. 4-2. Schemes for CO_2 reduction by different catalytic mechanisms.....94

Fig. 4-3. CoPc and CoPc-A compared for CO_2RR to CO.....97

Fig. 4-4. Possible mechanisms for CO_2RR beyond CoPc-CO^-.....99

Fig. 4-5. CoPc modified by axial ligands.....101

Fig. 4-6. Geometries of CoPc and CoPc-L molecules.....103

Fig. 4-7. Adsorption energy of CO_2 and CO to CoPc and CoPc(L) molecules.....105

Fig. 4-8. Geometries of adsorbed CO_2 and CO on CoPc-L1.....106

Fig. 5-1. Concept of an ultimate multi-scale model of plasma catalysis.....118

Fig. 5-2. Representative structure-search workflow aided by a surrogate machine learning model.....120

Abstract

Carbon dioxide emissions are a defining issue of our time, and how we deal with this problem has far-reaching impacts on our climate and future quality of life. Heterogeneous catalyst research offers promising strategies for converting CO_2 emissions into useful chemical feedstocks, providing an economic incentive for CO_2 conversion. To advance the effort for cost-effective CO_2 reduction, catalysts must be highly active and selective while minimizing the amount of precious metal required. Here, single-atom catalysis offers multiple advantages over larger nanoparticles. Single-atom catalysts are often highly active and selective due to their single-site nature and their unique electronic properties. The work presented in this dissertation focuses on the capabilities of single-atom catalysts to promote the CO_2 reduction reaction using three methods with different energetic driving forces, namely, thermal catalysis, plasma catalysis, and electrocatalysis. These catalyst systems are modeled using density functional theory (DFT) to accurately describe the atomic structure of each catalyst and calculate the thermodynamic and kinetic properties of the reaction mechanism.

Thermal catalytic CO_2 reduction by H_2 (**Chapter 2**) primarily proceeds by one of two possible reaction pathways, either producing methane via catalytic methanation ($CO_2 + 4H_2 \rightleftharpoons CH_4 + 2H_2O$) or carbon monoxide via the reverse water gas shift reaction (RWGSR, $CO_2 + H_2 \rightleftharpoons CO + H_2O$). Atomically dispersed Rh_1 catalysts on TiO_2 show high selectivity toward the rWGSR compared with larger Rh nanoclusters. In this dissertation we report DFT calculations and microkinetic simulations that clarify the Rh_1 active sites and rWGSR pathway on anatase

TiO_2(101), as well as the high rWGSR selectivity of Rh_1 compared with supported Rh_x (x = 2–8 atoms) nanoclusters. Predicted turnover frequencies and apparent activation barriers for Rh_1 indicate preferred reaction involving CO_2 dissociation assisted by a support oxygen vacancy nearby the Rh_1. The single atom catalyst is selective toward CO rather than CH_4 because of the weak adsorption of CO, large barrier for C-O bond dissociation, and the lack of nearby metal sites for H_2 dissociation, in contrast to Rh_x nanoclusters, including Rh_2 dimers.

Low-temperature plasma (LTP) catalysis (**Chapter 3**) offers various synergistic effects for increased activity, yield, or selectivity compared to conventional thermal catalytic approaches. Using density functional theory modeling, we study single-atom catalyst systems to understand the importance of plasma-induced surface charging on CO_2 activation. We analyze six different metals on three different supports to analyze trends across the periodic table. We find that accumulated surface charge on the single atom increases the CO_2 adsorption strength and decreases the CO_2 dissociation barrier for all studied single-atom/support combinations. Our work demonstrates that surface charging should be considered in strong electric fields because it can have a large effect on molecule chemisorption and bond-breaking on catalytic surfaces.

Electrocatalytic reduction of CO_2 (**Chapter 4**) is a frequently studied strategy to convert CO_2 using renewable sources of electricity. Recent work has demonstrated the capability of the molecular catalyst CoPc to convert CO_2 into methanol in a single reaction setup. Modifying the CoPc molecule with axial ligands shows increased effectiveness for CO_2 adsorption, often the rate-limiting step of the reaction. In this dissertation, we investigate the effect of ligand choice on the CoPc binding characteristics for CO_2 and the important CO intermediate. CO_2 adsorption results agree closely with prior literature measurements, and the results for CO adsorption show a reverse trend with respect to ligand electron donation strength compared to adsorption of CO_2. These

findings show that a careful choice of ligand must be made that optimizes for strong CO_2 adsorption and a moderate CO adsorption in order to optimize for methanol selectivity.

Chapter 1

Introduction and Background

Parts of this chapter were adapted from F. Doherty, Hui Wang, Ming Yang, and B. R. Goldsmith, "Nanocluster and Single-Atom Catalysts for Thermocatalytic Conversion of CO and CO_2." *Catal. Sci. Technol.*, 2020, **10**, 5772.

1.1 Motivation

Over the last century, our world has seen a massive advancement in industrial activity and a growth in population. With these advancements, our global energy consumption and emissions of environmental pollutants have grown along with them. One of the biggest potential impacts on our environment has been the steady increase in greenhouse gas emissions, predominantly CO_2 from the industrial and energy sectors. From 1970 to 2014, the global emissions of greenhouse gases measured in CO_2 equivalent (CO_2e) has increased from ~4 gigatons to over 9 gigatons of CO_2e,[1] and the concentration of CO_2 in our atmosphere has reached a historically high level of 420 parts per million (ppm).[2] Clearly CO_2 emissions are a defining issue of our time and are at the center of many of our sustainability efforts, and how we deal with this problem has far-reaching impacts on the world.

In 2007, the U.S. Department of Energy's list of Grand Challenges cited the efficient synthesis of materials by catalysis as one of the top five ongoing technical challenges for the scientific community[3] — this grand challenge remains true today. New catalyst discoveries are

urgently needed to address many of our world's most pressing environmental challenges, including climate change due to the emission of CO_2. Strategies that convert CO_2 emissions into a useful chemical feedstock are especially promising and would provide an economic incentive for CO_2 conversion.[4] Unfortunately, the lack of active and selective catalysts hinders CO_2 conversion to desirable products.

The work presented in this dissertation focuses on this issue of catalyst activity and selectivity for CO_2 conversion. Catalytic CO_2 reduction can proceed by a number of reaction pathways toward a variety of products, for instance, producing methane via catalytic methanation ($CO_2 + 4H_2 \rightleftharpoons CH_4 + 2H_2O$) or carbon monoxide via the reverse water gas shift reaction (RWGSR, $CO_2 + H_2 \rightleftharpoons CO + H_2O$).[5] CO can be used as part of the Fischer-Tropsch process to create a variety of hydrocarbon chemicals,[6] and this makes it a more desirable product compared to CH_4. One major hurdle of the CO_2 reduction reaction is the energy required to convert thermodynamically stable CO_2 molecules into a more useful, but less thermodynamically preferred product such as CO. Furthermore, the variety of products from CO_2 conversion detracts from the yield of the desired CO product and complicates downstream separation. By advancing the capabilities of catalysts to convert CO_2 with higher energy efficiency and more selectivity toward the desired product, we can improve the feasibility of industrial strategies for CO_2 emissions control.

To develop an active and selective catalyst for CO_2 reduction to a single desired product, we must understand the underlying mechanism that determines which reaction pathway is followed (e.g., methanation vs. RWGSR). Although it is difficult to isolate exact structure-activity-selectivity relationships from experiments, computational modeling offers a precise atomistic view of the catalyst surface to help identify trends as well as to interpret and guide experiments. First-principles computational catalysis using density functional theory (DFT) and microkinetic

modeling is a potent strategy to understand catalyst performance and properties (e.g., stability, activity, and selectivity), and it is the predominant strategy used in this research to study the catalyst structure's effect on activity and selectivity.

Precious metals are active catalytic components for the conversion of CO and CO_2, but the high global demand for such reactions requires low catalyst loadings of these metals because of their scarcity and high cost. Nanoclusters (~1 nm) and single atoms (**Fig. 1-1a**) provide nearly 100% atom efficiency for a specified reaction and therefore are desirable from an atom economy viewpoint.[7,8] For many reactions, nanoclusters have higher intrinsic activity than their larger nanoparticle counterparts, in large part due to their undercoordinated nature and increased prevalence of corner and edge sites. **Fig. 1-1b** shows a typical relationship between particle diameter and the fraction of corner, edge, and surface (terrace) atoms in a representative supported particle, highlighting that the fraction of corner and edge sites increases as particle diameter decreases.[9] Additionally, single atoms can display catalytic properties far removed from their nanocluster counterparts because of their unique electronic properties and coordination environment. The discussion of similarities and differences between supported single-atom and nanocluster catalysts has garnered much attention.[8,10–12] Nonetheless, the reasons underlying the differences behind single-atom and nanocluster catalytic properties require further exploration for numerous systems. Unraveling the origin of the catalytic differences between nanoclusters and single atoms is complicated by the possibility of dynamic structural rearrangements of the catalytic species and the support under reaction conditions. Transformations between nanoclusters and single atoms often occur[13] as well as the migration of single atoms to defect locations or step edges during a reaction,[14,15] which changes catalytic performance.

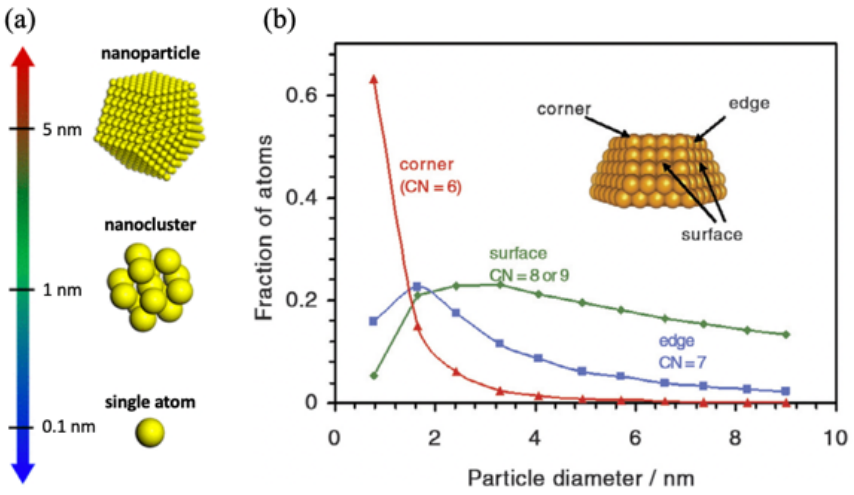

Fig. 1-1. Surface site counts relative to particle size. (a) Typical size range of nanoparticles, nanoclusters, and single atoms. Adapted from ref. 10. (b) Relationship between particle diameter and the fraction of corner, edge, and surface (terrace) atoms in a representative supported Au particle shaped as the top half of a truncated octahedron. CN = coordination number. Adapted from ref. 9.

In addition to the catalyst structure design, researchers also have a choice when it comes to the external driving force of the reaction. As CO_2 reduction is an endothermic reaction, external energy must be supplied to the reaction to drive it forward. The source of this energy could be heat (thermocatalysis), excited plasma (plasma catalysis), or electricity (electrocatalysis), to name a few examples. There are benefits and detriments to each choice. A thermally driven reaction can make use of existing process heat from industrial processes to reduce waste and is much more simple to scale up compared to other reactions, but a further supply of heat is often needed that would likely rely on carbon-emitting sources.[16] There is also a limited variety of products that have been demonstrated by thermocatalysis.[17] Plasma generation allows for many interesting benefits in the area of catalysis, since it is capable of activating very stable molecules like CO_2 and can enable the direct scission of the C-O bond.[18,19] Still, plasma remains very energetically costly to produce and would have to rely on an abundant source of cheap renewable energy. A more immediately realistic use of renewable electricity would be the electrocatalytic reduction of CO_2.[20,21] This often-studied strategy can make use of renewable electricity sources to be net carbon

negative. However, the electrocatalytic reaction typically occurs in the aqueous phase, and therefore requires a solvated source of CO_2 and a large amount of liquid for scaled up reactors. While each method has its challenges, each also shows a great deal of potential for future advancement. This dissertation will explore each driving force using computational modeling methods and density functional theory, depicted in **Fig. 1-2**.

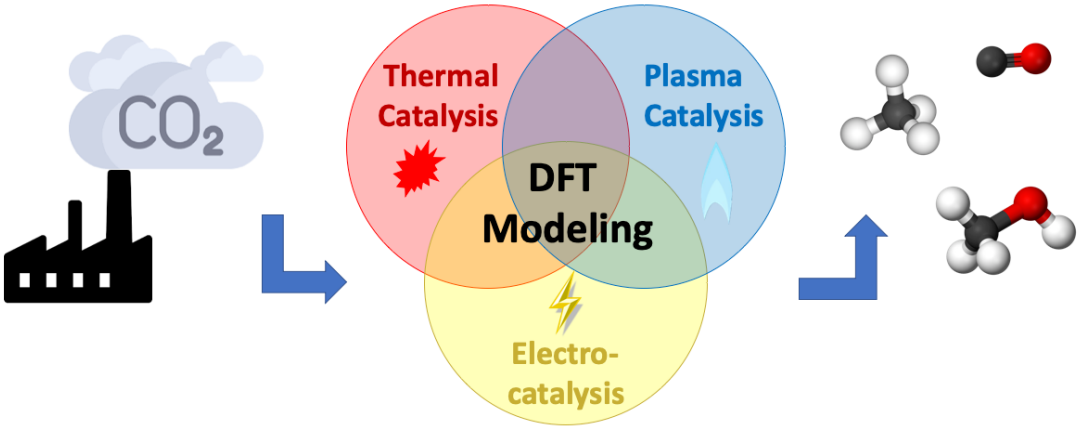

Fig. 1-2. Illustration of three different driving forces for CO_2 reduction. We will explore the uses of thermal catalysis, plasma catalysis, and electrocatalysis for conversion of CO_2 into value added chemicals such as CO, CH_4, and CH_3OH.

1.2 Background

This section will provide experimental and theoretical background on single atom and nanocluster catalysts from relevant literature sources. Section 1.2.1 discusses the structural changes that occur dynamically among nanocluster and single-atom catalysts that impact catalytic properties. Section 1.2.2 details the effects of coordination environment on the catalytic performance. Section 1.2.3 provides an overview of current research in the areas of thermocatalysis (1.2.3.1), plasma catalysis (1.2.3.2) and electrocatalysis (1.2.3.3).

1.2.1 Dynamic Structural Changes of Nanoclusters and Single-Atom Catalysts

As mentioned previously, the CO_2 reduction reaction activity and selectivity are highly dependent on the structure of the catalyst at the atomic scale. Understanding the dynamic structural response of nanoclusters and single atoms under reaction conditions is of broad importance

because these structural changes can affect their catalytic properties. Under relevant operating conditions for emissions control, the presence of reactants can induce aggregation of single atoms into nanoclusters,[22] or cause disintegration of supported nanoclusters to single atoms.[23–25] Knowledge of the behavior and mechanism of these structural changes in regulating catalytic performance will guide the design of more efficient catalysts for emissions control.

A thermodynamic model was developed to predict the conditions for which reactants induce sintering of smaller particles into larger particles via Ostwald ripening and disintegration of particles into single atoms.[23] This thermodynamic model incorporates how the reaction environment, metal-support interaction, and particle size affects the surface energy of the catalytic species and the Gibb's free energy of particle formation or disintegration. Typically, increasing the reactant partial pressure, lowering the temperature (without kinetically hindering disintegration), and decreasing particle size will increase the thermodynamic driving force for particle disintegration. Although coordinatively unsaturated single atoms on surfaces (adatoms) are often unstable, adsorbates can stabilize the adatoms by complexation. The energy diagram in **Fig. 1-3a** illustrates how it would be thermodynamically unfavorable for a bare metal atom to detach from a metal nanocluster. In contrast, adsorption of CO lowers the thermodynamic driving force for nanoparticle disintegration to form single-atom complexes, which is relevant to the CO_2 reduction reaction as CO is a major product formed. This thermodynamic model predicted that $Rh/TiO_2(110)$ nanoclusters were more susceptible to CO-induced disintegration into single atoms than $Pd/TiO_2(110)$ and $Pt/TiO_2(110)$ nanoclusters because of the highly exothermic formation energy of the stable Rh-dicarbonyl complexes ($Rh_1(CO)_2$) compared with Pd- and Pt-carbonyl complexes, consistent with experimental observations.[24] This phenomenon is illustrated in **Fig. 1-**

3b for Rh/TiO_2, where the Rh nanocluster disintegrates to form stable $Rh_1(CO)_2$ complexes, and these single-atom species can catalyze CO_2 reduction to CO with high selectivity.[26]

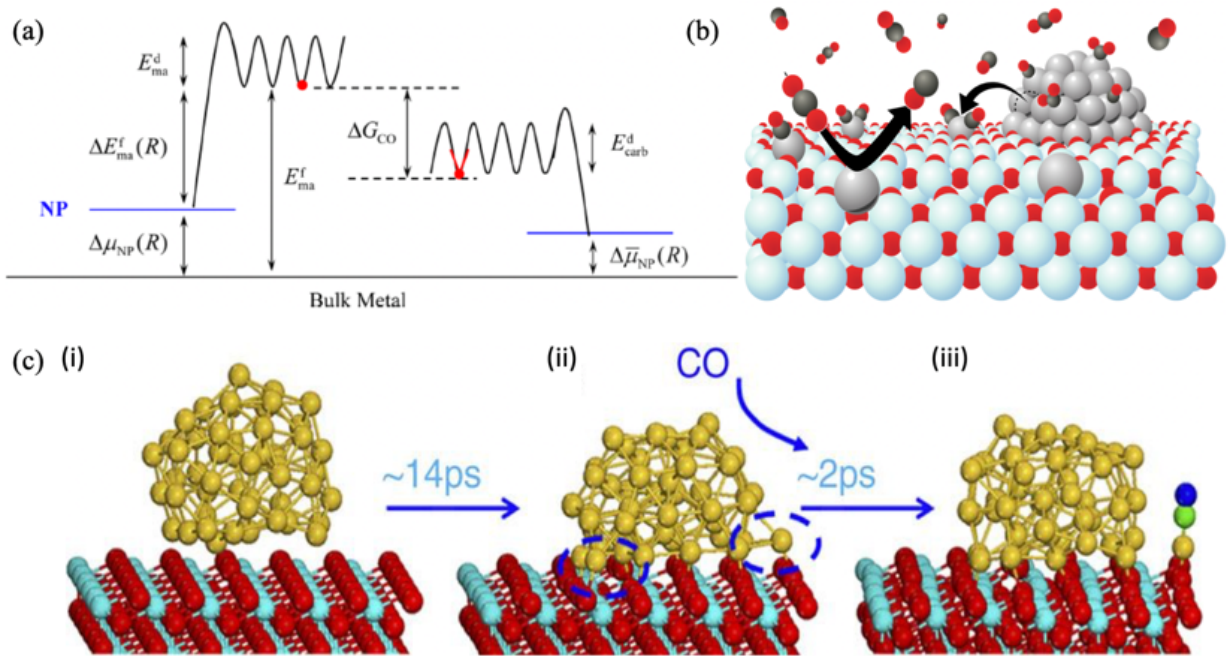

Fig. 1-3. Reactant-induced disintegration of nanoclusters into single atoms. (a) Energy diagram showing how the presence of CO stabilizes a single atom (red dot) by forming a single-atom carbonyl complex with lower formation energy compared with the bare single atom. $\Delta\mu_{NP}(R)$ and $\Delta\bar{\mu}_{NP}(R)$ are the chemical potentials of supported nanoparticles (NPs) without and with reactants present, E^{f}_{ma} ("ma" refers to a bare metal atom) and $\Delta E^{f}_{ma}(R)$ are single-atom formation energies on the support with respect to infinite and finite nanoparticle radii (R), ΔG_{CO} is the Gibbs free energy of adsorption of CO on the single atom, and E^{d}_{ma} and E^{d}_{carb} ("carb" refers to the carbonyl complex) are the diffusion barriers of single atoms on support. Adapted from ref. 23. (b) Schematic of a Rh nanocluster on TiO_2 that is disintegrating in the presence of gaseous reactants (CO, CO_2, H_2) to form a stable Rh-dicarbonyl complex. The Rh_1 species can selectively reduce CO_2 to CO and water. Hydrogen and water are not shown. Color legend: light blue = Ti; gray = Rh; red = O; black = C. (c) Geometry snapshots from a molecular dynamics simulation of $Au_{50}/CeO_2(111)$. (i) The initial configuration of $Au_{50}/CeO_2(111)$; (ii) $Au_{50}/CeO_2(111)$ after 14 ps of simulation at 700 K, where a low-coordination number gold atom is formed at the metal/support interface (highlighted within the blue circle); (iii) After CO adsorption at the low-coordination gold atom, it separates to form an isolated Au_1^+-CO cationic species. Color legend: yellow = Au; teal = Ce; red = O (within ceria); green = C; blue = O (within CO). Adapted from ref. 27.

Nanocluster disintegration into smaller clusters or single atoms can occur spontaneously under reaction conditions and may either be desired or undesired depending on the application. Volatile single-atom species (e.g., Ni-carbonyl complexes) form from nanoparticles and cause catalyst deactivation.[28,29] In other cases, reactant-induced disintegration has been used to

redisperse (and thus reactivate) sintered catalysts for CO oxidation[25,30] and CO_2 conversion.[26] A recent study predicted that the dynamic creation of single-atom active sites from Au nanoclusters is essential to catalytic CO oxidation. Single gold cations were simulated by *ab initio* molecular dynamics to break away from the interface of gold nanoparticles on ceria under reaction conditions to catalyze CO oxidation, **Fig. 1-3c**.[27] A cationic Au_1^+-CO species forms that interacts with the reducible ceria support and consequently has low activation barriers for CO_2 formation and desorption. After a catalytic turnover has occurred, the Au_1 single atom may recombine with the Au nanoparticle. These simulations suggest the true catalytic species exist transiently under reaction conditions for Au/CeO_2. The separation of Au_1 single atoms from nanoclusters supported on amorphous carbon was recently confirmed by *in situ* high-resolution TEM and HAADF-TEM[31] while catalyzing CH_4 pyrolysis. This finding corroborates the prevalence of nanocluster transformations to single-atom active sites under reaction conditions. The creation of transient adatoms induced by reactant adsorption at the nanocluster interface may be an often overlooked but critical phenomenon in catalytic systems of relevance to emissions control.

The transformation between Pt single atoms and nanoclusters is often reversible, depending on the catalyst-support interactions. This reversible transformation was elucidated in high-silica chabazite zeolite,[32] where Pt oxide nanoclusters (~1 nm) were initially encapsulated within the zeolite. Using *operando* EXAFS and HAADF-STEM characterizations, the Pt nanoclusters were detected to fragment into single atoms in 20% O_2/He between 450–650 °C, but the Pt nanoclusters reformed in the presence of 4% H_2/He between 150–650 °C. Smaller Pt nanoclusters (0.8–1 nm) were more easily fragmented in an oxidative atmosphere than larger nanoclusters (1–1.5 nm).

Similar oxidative redispersion phenomena were also found on a Pt/CeO_2 catalyst,[33] as shown in **Fig. 1-4a**. *In situ* environmental transmission electron microscopy monitored structural

changes of the Pt/CeO_2 catalyst induced by oxidative/reductive treatment. Small Pt nanoclusters (< 2 nm) were observed after reduction in H_2 at 250 °C, but redispersion into single atoms occurred after oxidizing in O_2 at 400 °C. Larger nanoclusters remained intact because they require higher temperatures to redisperse. After another round of reduction in H_2 at 250 °C, the Pt nanoclusters reformed from the isolated Pt adatoms. Therefore, the reversible transformation of Pt nanoclusters into single atoms can be achieved by tuning the reducing/oxidizing conditions on ceria. Pd nanoparticles (7.9±0.6 nm) at 0.007 wt.% loading on Al_2O_3 were also reported to disintegrate into single atoms after aging in dilute oxygen at 775 °C for one hour.[29]

Besides nanoparticle-to-single-atom transformations induced by oxidative/reductive treatment, there are reports demonstrating nanoparticle dispersion into single atoms or small clusters by reactant-induced ligand effects.[34–36] For example, Rh nanoclusters (1.0–2.5 nm) on TiO_2 are stable under CO_2:$4H_2$ reaction conditions,[26] but dispersed to Rh_1 atoms under H_2-lean gas mixture ($10CO_2$:H_2), even though CO_2 is a relatively weak oxidant. Generally, strongly adsorbing reactants (strong ligands) induce nanoparticle redispersion to single atoms. Nanoparticles of Ru, Rh, Pd, Ag, Ir, and Pt supported on activated carbon (AC) were dispersed to single atoms by reacting with a CH_3I and CO gas mixture.[37] Taking Rh/AC as an example, the dispersion of Rh/AC sample was examined in the presence of a mixture of CO and CH_3I for different durations. Rh nanoclusters remained unchanged at 4–5 nm after two minutes on stream. However, after 15 minutes of treatment, smaller clusters became the predominant species. The *operando* EXAFS results suggest that the Rh-Rh coordination number decreases while the Rh-CO and Rh-I coordination numbers increase with time on stream. These results imply the gradual shrinkage of Rh nanoparticles due to the substitutional coordination by CO and I• free radicals. The atomic dispersion process of Rh nanoparticles by CO and I• ligands was modeled by DFT calculations,

Fig. 1-4b. A one-by-one mechanism was postulated in which ligands sequentially attach to a Rh atom and promote separation from the nanocluster. This mechanism was rationalized by the effective atomic number (EAN) and reaction energy for each step. The EAN is defined as the number of electrons around an atomic nucleus, including those from bonded ligands. From the "EAN rule" based on a filled valence shell, the complex will be most stable with an EAN of 18 (filled *s*, *p*, and *d* shells),[38] although exceptions to this rule exist for other metallic complexes (e.g., square-planar Pt complexes).[39] By this mechanism, the original Rh nanoparticles (4–5 nm) disperse into Rh_1 species as $Rh(CO)_2I_3$(O-AC) and $Rh(CO)I_4$(O-AC) structures. This work clarifies how nanoparticles disintegrate into single atoms through strong interaction with ligands.

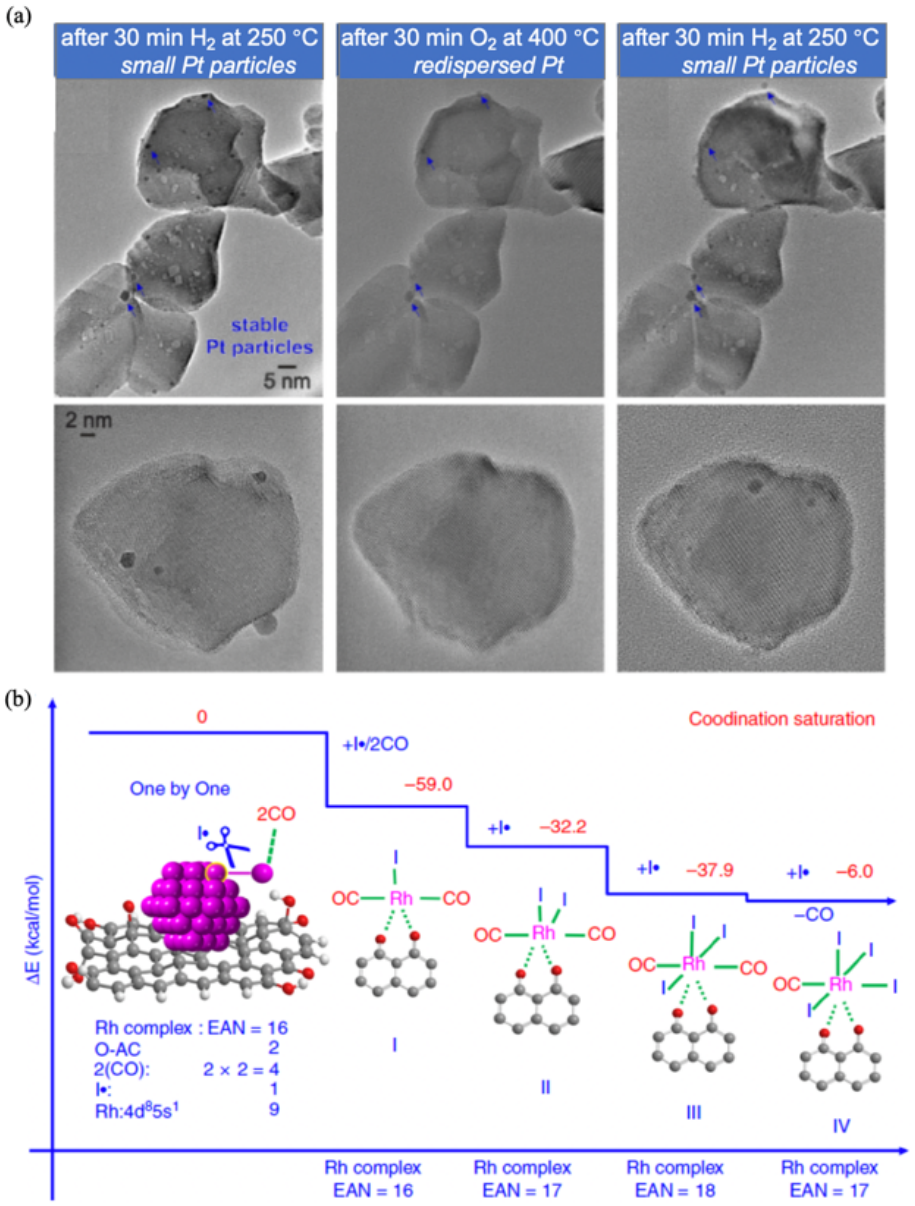

Fig. 1-4. Transformation between single atoms and nanoclusters. (a) Environmental transmission electron microscopy images of Pt/CeO_2 captured at three representative areas after reductive treatment by H_2 (Pt nanocluster formation), followed by oxidative treatment (Pt redispersion) and by another reductive treatment (Pt nanocluster reformation). Adapted from ref. 33. (b) Atomic dispersion model of Rh nanoparticles on activated carbon with CO and I• as ligands via a one-by-one mechanism. The values above every Rh complex model are changes in system energy in kcal/mol. Adapted from ref. 37.

Although nanoparticle disintegration to single atoms occurs for many systems under reaction conditions, a more pervasive phenomenon is single atoms sintering to larger nanoclusters, resulting in the overall loss of catalytically active metal surfaces. For example, single atoms of Ni_1 in $Ni_xMg_{1-x}O$ formed Ni particles up to 10 nm after eight hours of reacting with a $4H_2$:$1CO_2$ gas

mixture at 350 °C and 3 MPa.[40] The reductive reactants and high pressure are driving forces to induce the transformation of single atoms to large nanoclusters. One strategy to improve the sintering resistance of single atoms during CO_2 reduction is to limit diffusion on the support surface through strong metal-support interactions.[41] Uniform Pt_1/CeO_2 with low Pt loadings (< 0.1 wt.%) exhibit resistance to reduction and sintering up to 500 °C in 0.05 bar H_2,[42] because the Pt_1 single atoms adopt thermodynamically stable adsorption sites during the anchoring process at low metal loadings. A DFT study of Pt_1/CeO_2, along with a variety of 3*d* (Fe, Co, Ni, Cu), 4*d* (Ru, Rh, Pd, Ag), and 5*d* (Os, Ir, Au) transition metals on ceria, was conducted to examine the sintering resistance of single-atom catalysts.[43] By studying the adsorption energy of different metal cations on a model 79-atom nanocluster of the same metal versus a cuboctahedral $Ce_{40}O_{80}$ nanocluster, the likelihood of sintering for the metal atoms was predicted. All studied cations had stronger binding energy to the ceria cluster than to their own metal clusters, suggesting that single atom dispersion on ceria is preferred over forming metallic particles. However, the resistance to sintering had different magnitudes based on metal identity. Platinum group metals (i.e., Pt, Pd, Ni) and cationic Fe, Os, and Co exhibited high single-atom stability, and therefore a large barrier for sintering, whereas cationic Ag, Au, and Ir were less resistant to agglomeration. The high sintering resistance of the platinum group metals was attributed to the stable square-planar coordination available to d^8 metal centers.

1.2.3 Influence of Coordination Environment Changes on Catalytic Performance

Understanding how the coordination environment of single atoms and nanoclusters change under reaction conditions and their effect on catalytic performance is important for catalyst design and mechanistic understanding. Advances in *in situ* spectroscopy under reaction conditions have led to many insights into how the structure of heterogeneous catalysts on stream affects their

activity, selectivity, and stability. *In situ* EXAFS enables detailed studies of the nanocluster and single-atom coordination environment in response to reactants.[44]

The coordination changes for nine different $Rh_1/TiO_2(110)$ structures under H_2, CO, and RWGS conditions were studied in a joint experimental-computational study.[13] Rh_1 single atoms were modeled by *ab initio* thermodynamics (**Fig. 1-5a**) to understand whether they substitute for Ti (**Fig. 1-5b**) or bind onto the $TiO_2(110)$ surface (**Fig. 1-5c**). By varying the oxygen chemical potential ($\mu(O)$) of the environment surrounding the Rh_1/TiO_2 system, the favored arrangement of the Rh atom placement and TiO_x stoichiometry can be influenced, thereby affecting the catalytic reactivity. Following the line of the lowest chemical potential in **Fig. 1-5a**, the preferred structure passes through three possible configurations. Under oxygen-rich conditions (high $\mu(O)$), Rh_1 prefers to substitute at the six-fold coordinated Ti site on a clean TiO_2 surface. As oxygen chemical potential decreases, oxygen vacancies form near Rh_1, and as oxygen chemical potential decreases further, the Rh atom instead prefers to adsorb above a three-fold coordinated oxygen vacancy. The experimental observations from CO infrared spectroscopy and scanning transmission electron microscopy confirmed the DFT-predicted response of Rh single atoms under O_2 gas (high $\mu(O)$) and H_2 and CO gas (low $\mu(O)$).

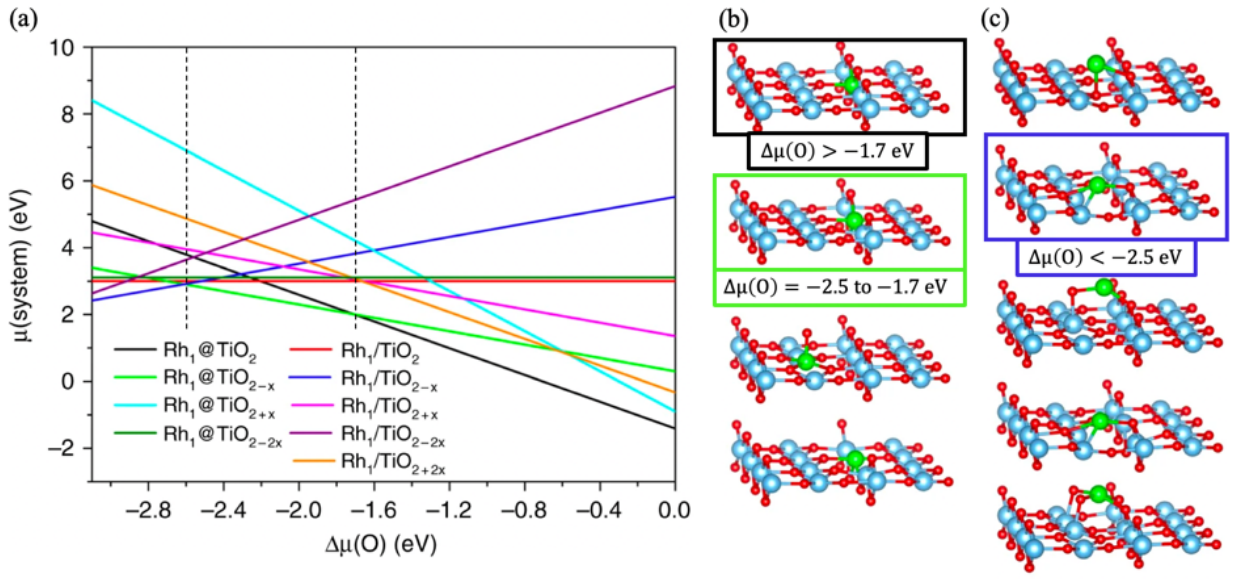

Fig. 1-5. Coordination environment changes in response to reactants and the effect on catalytic performance. (a) Stability trends of different Rh_1 single atom binding locations on rutile $TiO_2(110)$ at substitutional (@) and supported (/) sites relative to oxygen chemical potential ($\Delta\mu(O)$). The study includes stoichiometric TiO_2, oxygen-deficient TiO_{2-x}, and excess oxygen TiO_{2+x}. The optimal structures for (b) substitutional and (c) supported Rh_1 single atoms on the rutile $TiO_2(110)$ surfaces. Here the Rh_1 species adopt different preferred sites based on changing oxygen chemical potential, with $Rh_1@TiO_2$ (black) preferred under oxygen-rich conditions ($\Delta\mu(O) > -1.7$ eV), $Rh_1@TiO_{2-x}$ (light green) under moderate conditions (-2.5 eV $< \Delta\mu(O) < -1.7$ eV), and Rh_1/TiO_{2-x} (blue) under oxygen-poor conditions ($\Delta\mu(O) < -2.5$ eV). Color legend: red = O; blue = Ti; green = Rh. Figures (a)–(c) were adapted from ref. 13.

Besides the coordination changes in response to reactants for CO_2 reduction, the correlation between the single-atom coordination structure and catalytic performance has also been elucidated for other reactions. The activity of Pt_1/Fe_2O_3 as a function of coordination structure was clarified for chemoselective hydrogenation of 3-nitrostyrene to 3-vinylaniline.[45] In that work, a series of Pt_1/Fe_2O_3 samples with gradually decreasing Pt-O coordination numbers were obtained by increasing the rapid thermal treatment temperature. Samples with a smaller Pt-O coordination or a lower oxidation state of the Pt_1 species correlated with higher catalytic activity for chemoselective hydrogenation. This finding demonstrates that the coordination environment has a major influence on the catalytic performance of single-atom catalysts.

Coordination environment also often has a large effect on nanocluster catalytic activity as well. Generally, supported nanoclusters adopt a variety of sizes and shapes that are difficult to

know *a priori*, particularly in the presence of adsorbates.[46] Consequently, a major challenge for modeling nanoclusters is finding model systems with realistic sizes, shapes, and surface compositions under reaction conditions. Many algorithms have been developed to model the diversity of nanocluster structures such as genetic algorithms,[47,48] basin hopping,[49] and grand canonical Monte Carlo.[50,51] However, modeling supported nanoclusters under realistic conditions is computationally demanding and requires much human effort. Nevertheless, there have been many advances in understanding the fluxionality of nanoclusters under reaction conditions via modeling. By fluxionality, we mean the dynamic nanocluster structural rearrangements triggered by adsorbates and reactions.[46] *Ab initio* molecular dynamics simulations have shown substantial isomerization of Pt_{13} clusters while dissociating methane at 400 K, far beyond what is observed thermally at 700 K.[52] Further modeling suggests that small Pt clusters can also break linear scaling relationships by way of their fluxionality compared with bulk metal or larger nanoparticles. Another instance of small cluster isomerization with beneficial catalytic effects is the dynamic restructuring of palladium-copper tetrahydride anions ($PdCuH_4^-$) for CO_2 reduction.[54] By a joint experimental-theoretical approach, these bimetallic hydride clusters were shown to convert CO_2 into formate and formic acid through a series of metastable cluster configurations. The lowest energy isomer had a 2.38 eV activation barrier for formate desorption, but a metastable isomer allowed for a more favorable overall reaction path, with two smaller barriers of 0.95 and 0.80 eV. These findings demonstrate the importance of studying multiple possible cluster structures as active sites, including metastable structures. On-going research is focusing on using machine learning to accelerate the structure search of catalysts,[55–57] which may benefit future studies of supported nanoclusters under reaction conditions and how their coordination environment influences catalytic performance.

1.2.3 Catalytic CO_2 Reduction

Due to environmental concerns, CO_2 reduction has been a broad and topical research area in heterogeneous catalysis. This subsection reviews a collection of recent research in the areas of thermocatalysis, plasma catalysis, and electrocatalysis for CO_2 reduction. Further focus on each catalytic method will be provided in Chapters 2 through 4.

1.2.3.1 Thermocatalytic CO_2 Reduction by Single Atoms and Nanoclusters

Generally, the thermocatalytic CO_2 reduction reaction mechanism depends heavily on the structural properties of catalysts. Additionally, the desorption behavior of CO is a key factor in determining the selectivity during CO_2 reduction. If the desorption of CO is favorable, reverse water gas shift reaction (RWGS) is the dominant reaction. Otherwise, further hydrogenation occurs to products such as methane or formic acid.[58–60] For many metal catalysts supported on metal oxides, single metal atoms tend to promote CO production via RWGS, whereas metal clusters promote CH_4 production via catalytic methanation. Here we will focus on the formation of CO and CH_4 products because of their versatility as feedstocks, but some systems often favor other products, including formic acid or methanol.

Multiple studies support the observation of a different reaction pathway between single atoms and nanoclusters for CO_2 reduction. For example, Ir nanoparticles were deposited on ceria to study how nanocluster size and coordination environment affect CO_2 reduction selectivity. The sizes of Ir clusters were adjusted to 2.2, 1.6, and 1.0 nm by varying Ir loadings from 20, 15, and 5 wt.%, respectively.[61] The Ir coordination environment, which can be tuned by the particle size, seemed to determine the selectivity in CO_2 hydrogenation. The Ir-O bond favors CO production, whereas the metallic Ir-Ir bond facilitates methanation. Ir/TiO_2 single atoms and clusters for CO_2 reduction were also studied through DFT modeling (**Fig. 1-6a**).[59] Compared with the step edges

of an Ir surface, the Ir_1 catalyst had a 2.45 eV higher activation barrier for CO dissociation. The work concludes that the Ir_1 catalyst prevents carbonyl dissociation and favors CO desorption. In contrast, Ir clusters were more capable of dissociating CO and further hydrogenating the intermediate to CH_4. More recent work similarly confirmed the RWGS reaction occurring on Pt_1/CeO_2, while methanation was more favored on Pt/CeO_2 nanoclusters.[62]

Shifts in catalyst selectivity to make either CO or CH_4 from CO_2 reduction by single atoms and nanoclusters have been reported. The CO_2 reduction selectivity of Ru nanoclusters supported on CeO_2, Al_2O_3, and TiO_2 were examined.[63] The work synthesized Ru nanoclusters with different sizes, but here we discuss the Ru nanoclusters of 2.6±0.3 nm as an example. Low-temperature H_2 reduction pretreatment of the nanoclusters at 230 °C was performed because metallic Ru can dissociate H_2 easily, making the catalyst a suitable material for methanation with high activity and selectivity. No change in the cluster size occurred from the reductive pretreatment. However, the reaction product distribution changed if an oxidative treatment was added at 230 °C before the H_2 reduction. The oxidative treatment switches the catalyst selectivity from methanation to RWGS, regardless of whether the support is Al_2O_3, TiO_2, or CeO_2. As shown in **Fig. 1-6b**, the oxidation-reduction treated samples are denoted as "OX-LTR" (oxidation–low temperature reduction) and "OX-HTR" (oxidation–high temperature reduction), both of which show higher CO selectivity than the "LTR" (low temperature reduction) sample. *In situ* and *ex situ* XAS revealed that oxidative treatment induced the redispersion of Ru nanoclusters into atomically dispersed RuO_x species, thus rationalizing the shift in catalytic function.

For the highlighted examples (Ir/CeO_2, Pt/CeO_2, Ru/TiO_2, etc.), there is a general selectivity tradeoff between RWGS and methanation based on the supported metal species. Typically, the RWGS is preferred when single atoms are the majority species, whereas the catalytic

reaction proceeds through the methanation pathway when nanoclusters are the dominant species. This selectivity difference aligns with the observation that single atoms typically bind CO weaker than nanoclusters, which allows CO to desorb from single atoms more readily than nanoclusters. Nanoclusters offer bridge sites that bind CO more strongly by way of two atoms, and this ensemble effect is not present with single atoms.[64] Additionally, the difference in ability of single atoms and nanoclusters to dissociate hydrogen may also contribute to the selectivity differences.[26,65,66] Nonetheless, exceptions to this selectivity trend do exist. Recently, a Co/γ-Mo_2N nanocluster catalyst, with an average of four Co atoms in each Co cluster, exhibited high CO selectivity of > 98%.[67] The Co precursor was impregnated in the pre-synthesized γ-Mo_2N, and the Co atoms assembled into nanoclusters after activation in a N_2-H_2 mixture at 863 K for two hours. This work found that the Co-N linkage is the primary chemical bond anchoring the Co nanoclusters to the support. Charge transfer from Co to Mo_2N inhibits the full dissociation of CO_2, thereby preventing the generation of the C or CH_x fragments that are necessary for methane formation. This work highlights the key role of the support material in regulating the reaction pathways, in addition to the chemistry of the supported metal structures.

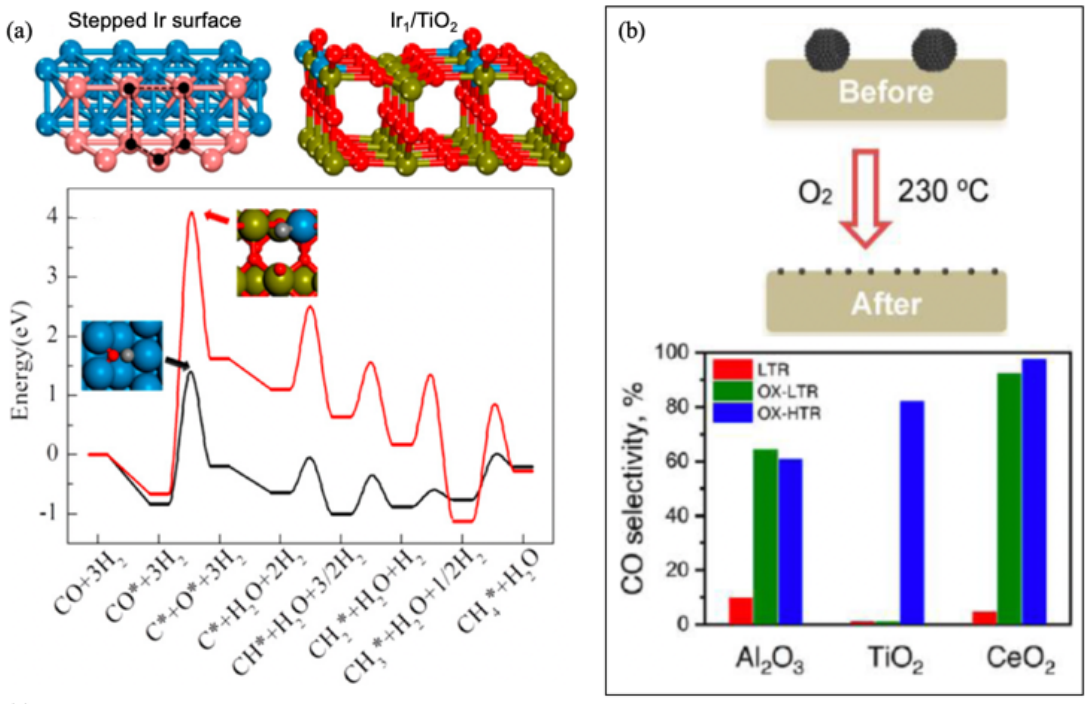

Fig. 1-6. CO_2 reduction activity and selectivity comparison of single-atom and nanocluster catalysts. (a) Comparison of CO conversion to CH_4 for stepped Ir surface (black line) and Ir_1 supported on rutile TiO_2(110) (red line). Structures of stepped Ir surface and Ir_1/TiO_2. Color legend: yellow = Ti; red = O; blue = Ir; pink = Ir step atoms. Ir_1/TiO_2 shows a larger activation barrier for CO dissociation than the stepped Ir surface and prefers CO desorption. Adapted from ref. 59. (b) Size-dependent CO selectivity on Ru/Al_2O_3, Ru/TiO_2, and Ru/CeO_2 for CO_2 reduction reaction. The top image illustrates Ru nanoparticle dispersion to single atoms after oxidative treatment at 230 °C. The bottom image shows CO selectivity for Ru species on Al_2O_3, TiO_2, and CeO_2 supports. LTR: low temperature reduction at 230 °C; OX-LTR: oxidation at 230 °C and low temperature reduction at 230 °C; and OX-HTR: oxidation at 230 °C and high temperature reduction at 530 °C. Adapted from ref. 63.

1.2.3.2 Plasma Enhanced Catalysis for CO_2 Reduction

Plasma is a phase of matter that consists of unbound electrons and positive ions in a net neutral mixture, and it can often contain other species of electronically excited states and radicals. Naturally occurring plasma is most commonly created at very high temperatures and pressures required for sustained ionization, like within the sun and other stars. However, plasma can also be created at atmospheric pressure and near room temperature by strong electric fields that cause a breakdown of the gas phase into a nonequilibrium plasma with high electron temperature (10^4 – 10^5 K) and low kinetic temperature (300 – 1000 K), referred to as low temperature plasma (LTP).

Plasma enhanced catalysis is a growing field of research that has reported a variety of synergistic effects for increased activity or selectivity compared to thermal catalysis, including operating beyond the thermochemical equilibrium limit.[18,19,68] LTP in direct contact with a catalyst or generated upstream from the catalyst promotes conversion of challenging reactions such as N_2 to ammonia[69] and CO_2 to fuels at lower thermal temperatures.[70] Plasma catalysis research offers several unique challenges and opportunities due to the two-way interactions that take place between the plasma and the catalyst surface, each able to impact the other. These many plasma-catalyst interactions are illustrated in **Fig. 1-7**. Still, there remain many unknown aspects of plasma-catalyst interactions that require further research.[71]

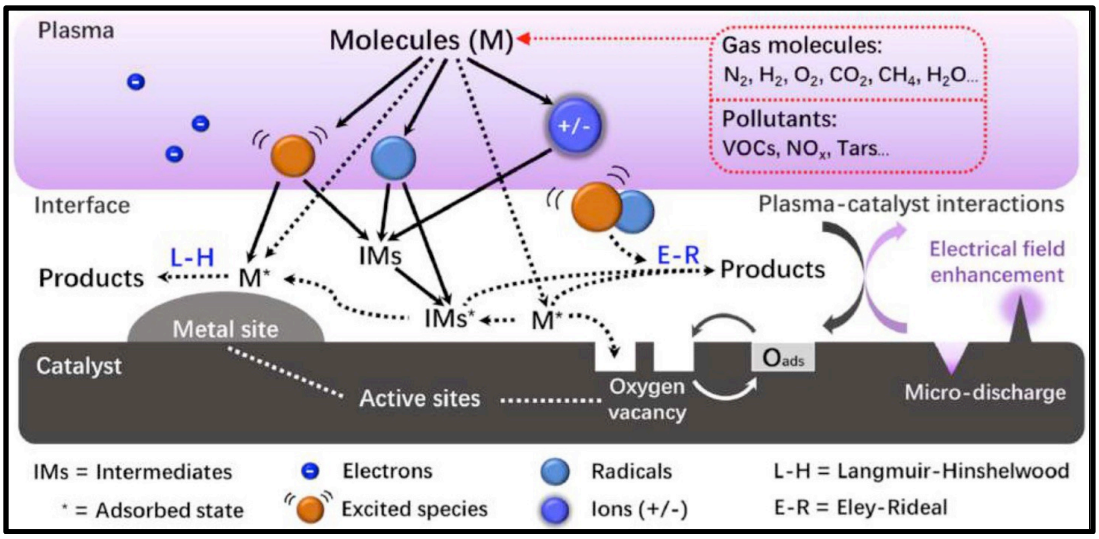

Fig. 1-7. Overview of the key mechanisms and species in the plasma and at the catalytic surface. The complex variety of interactions makes plasma catalysis an attractive area of research but a challenge for building accurate models. Adapted from ref. 19.

LTP has been researched as a CO_2 reduction catalyst in recent research. The synergistic effect of combined plasma and catalyst has been demonstrated through studying the CO_2 conversion rate and energy efficiency. Researchers compared the CO_2 conversion rate for plasma alone against a plasma + NiO/TiO_2 catalyst system and a plasma + TiO_2 system.[72] The inclusion of bare TiO_2 did not enhance the conversion effect, but adding NiO/TiO_2 had a two-fold increase in CO_2 conversion and energy efficiency (**Fig. 1-8a**).

Atomistic modeling using quantum mechanics can give insight into LTP-enhanced catalytic phenomena.[73–75] The plasma-solid interface has many phenomena that may affect catalytic performance (e.g., radical species, ions, excited vibrational species, electric field) that atomistic modeling can help understand. Because of the complexity of treating all possible effects,[19] however, atomistic modeling studies thus far have focused on probing one or two LTP-based phenomena at a time. Modeling each LTP/catalyst interaction in isolation helps to assess their relative impact and deconvolute the LTP effects on catalysis. For example, the role of plasma-induced vibrational excitations of N_2 to enhance ammonia synthesis has been studied by DFT and microkinetic modeling.[69] **Fig. 1-8b** shows how including the vibrational excitation effects for the NH_3 production reaction increased the overall modeled turnover frequency. Additionally, the optimal catalyst under LTP conditions was different than the optimal catalyst for thermocatalytic conditions, opening new materials spaces for exploration. Vibrationally excited states of H_2 and CH_4 were explicitly modeled using molecular dynamics,[76] finding that the presence of nonequilibrium vibrational states had a greater impact on catalytic activity for terrace surfaces compared to stepped surfaces. Modeling predicted that radical impingement of plasma-generated atomic N and O species onto Pt films gave increased production of NO compared to the conventional Langmuir-Hinshelwood reaction of adsorbed molecular $*N_2$ and $*O_2$.[77] The role of surface charging has also been examined by atomistic modeling,[78,79] but is less explored compared to the effect of vibrational excitations and radical formation.

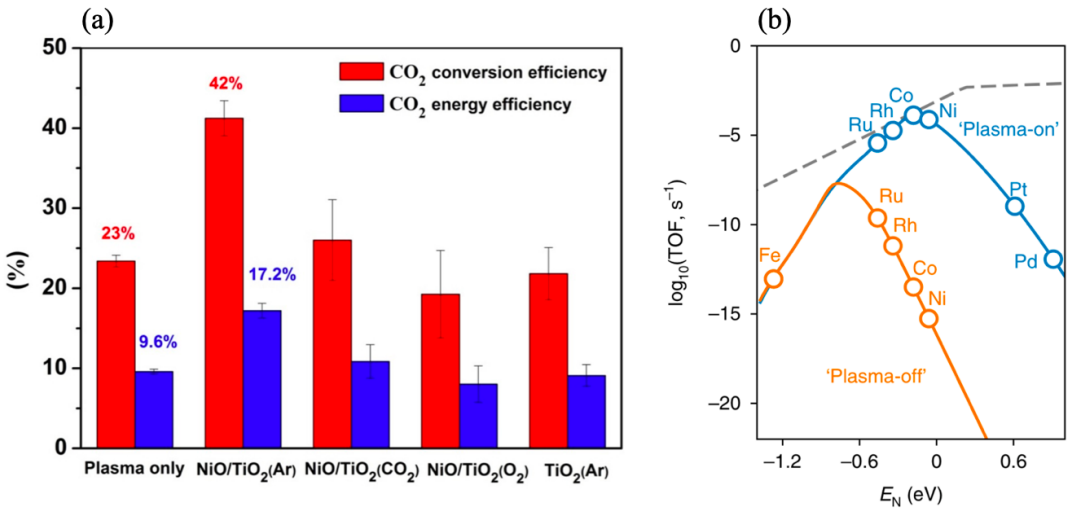

Fig. 1-8. Plasma enhancement effect on catalytic reactions. (a) CO_2 conversion efficiency and energy efficiency are both improved when combining plasma with a NiO/TiO_2 catalyst (42% conversion, 17.2% energy efficiency) compared to plasma alone (23% conversion, 9.6% energy efficiency). Adapted from ref. 72. (b) Microkinetic model for NH_3 production including plasma-generated vibrational excited states (plasma on) outperforms the base thermocatalytic model (plasma-off) and shifts the volcano peak to favor more earth-abundant metals Co and Ni over Ru and Rh. Adapted from ref. 69.

Plasma impinging onto a catalyst surface causes an accumulation of negative surface charge, which has implications for catalytic performance.[80–82] If the surface charging is sufficiently large, catalyst activity and selectivity can be modified from changing the adsorption strength of molecules (thus changing species coverages) and by increasing intrinsic kinetics by decreasing activation barriers of elementary reaction steps. The nature of the support and catalyst particle size can affect the importance of surface charging on heterogeneous catalysis. For example, DFT modeling was used to probe how plasma-induced surface charging changes the adsorption strength and activation of CO_2 on atomically dispersed metal ions (i.e., single atom catalysts) and nanoclusters on metal oxide supports. Specifically, Ti_1, Cu_1 and Ni_1 single atoms on γ-$Al_2O_3(110)$,[78] as well as Cu_5 and Ni_5 clusters supported on anatase $TiO_2(101)$,[79] were studied. Plasma-induced surface charging dramatically increased CO_2 adsorption strengths and decreased activation barriers for $*CO_2$ dissociation to *CO and *O for both single atoms and clusters in comparable magnitudes. Prior research has not yet explored the effects of surface charging across

a variety of catalyst materials or observed the dependence on the electronic structure of the metal and support, such as the number of *d* electrons of the metal or the support reducibility. This allows an opportunity for our research to contribute in this area by modeling different combinations of metal and support across the periodic table.

1.2.3.3 Electrocatalytic CO_2 reduction

Perhaps the most often explored method of CO_2 reduction in recent research has been electrocatalysis. Electrocatalysis has the benefit of providing an alternate source of hydrogen via H^+ in solution instead of H_2 gas which is costly to produce and has its own negative environmental impact. The electrocatalytic cell can be run by renewable sources of electricity, and therefore avoids another potential carbon emitting source that thermocatalysis depends on. Both homogeneous and heterogeneous catalytic methods have been developed, illustrated in **Fig. 1-9**. The catalyst is considered homogeneous when the reaction and the catalyst are both in the solvated phase, usually the case for small molecular catalysts (**Fig. 1-9a**). Those same molecular catalysts could instead be affixed to the electrode surface (**Fig. 1-9b**), or the electrode itself can act as the catalyst surface (**Fig. 1-9c**) to create a heterogeneous catalyst.

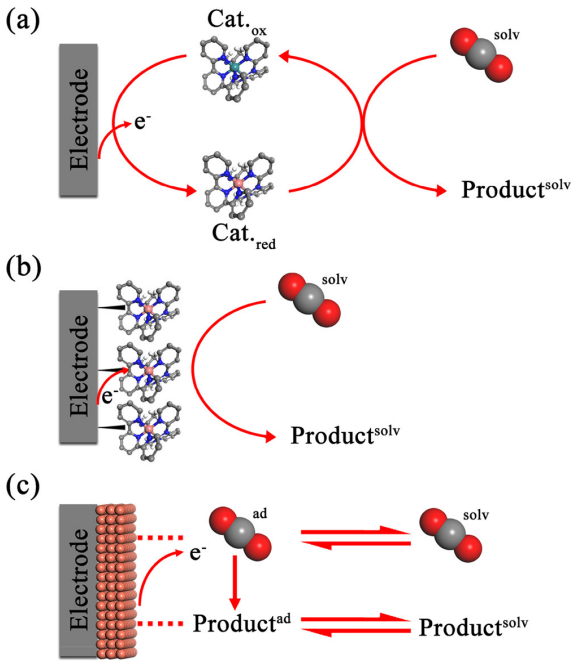

Fig. 1-9. Illustrated depiction of CO_2 electrocatalytic methods. (a) Homogeneous catalyst, where a solvated molecular catalyst is reduced by the electrode and then oxidized by the CO_2 reacting to form a product in the catalyst cycle. (b) Affixed catalyst, where the molecular catalyst site is joined with the electrode to reduce CO_2 at the surface. (c) Heterogeneous catalyst, where the electrode itself (either bulk metal or coated surface) acts as the catalyst surface by adsorbing and reducing CO_2. Image reproduced from ref. 20.

The strategy of affixing metal-organic molecular complexes onto the electrode surface offers several distinct advantages, and has been researched extensively in recent literature.[83,84] It maintains the highly specific and tunable coordination environment of the homogeneous organometallic complexes while allowing for easier product separation and scale-up available with heterogeneous catalysis.[85] The active site can be very specifically chosen and designed, and it uses a much smaller total amount of active metal compared to a solid metal electrode or metal coating.

Cobalt phthalocyanine (CoPc) is one such organometallic complex that has been investigated as a catalyst for CO_2 reduction. Originally, research into CoPc suggested that only CO_2 to CO was possible,[86,87] but more recent studies have demonstrated a cascading reaction to methanol via CoPc affixed to carbon nanotubes.[88] Researchers showed that the methanol generation achieves above 40% faradaic efficiency. Catalytic activity is enhanced by the presence of electron-donating amino substituents, indicating that intentional modification of the CoPc

ligands can benefit the reaction. Another study showed that the diameter of the carbon nanotube supporting CoPc can have a strong influence on catalyst activity.[89] Wider nanotubes achieved more CoPc dispersion and prevented detrimental stacking and aggregation. This dependence on CoPc dispersion was then modeled by comparing CoPc monomers and dimers in a computational study.[90] Only monomers showed a capability to produce methanol due to the easier reduction to $CoPc^-$, allowing for the more electron-demanding reduction to CH_3OH at less negative reduction potentials. The effect of aggregation was studied directly by creating a modified CoPc with additional ligands attached to the outer rings of phthalocyanine.[91] This study investigated cobalt(II) octaalkoxy-phthalocyanine (labeled CoPc-A) compared to CoPc for increased catalytic performance. **Fig. 1-10** depicts how the modified CoPc-A demonstrated higher catalytic activity than base CoPc when dispersed on a chemically converted graphene (CCG) substrate. The added groups on CoPc-A caused additional steric interference that kept them from aggregating as much as CoPc, which resulted in increased activity.

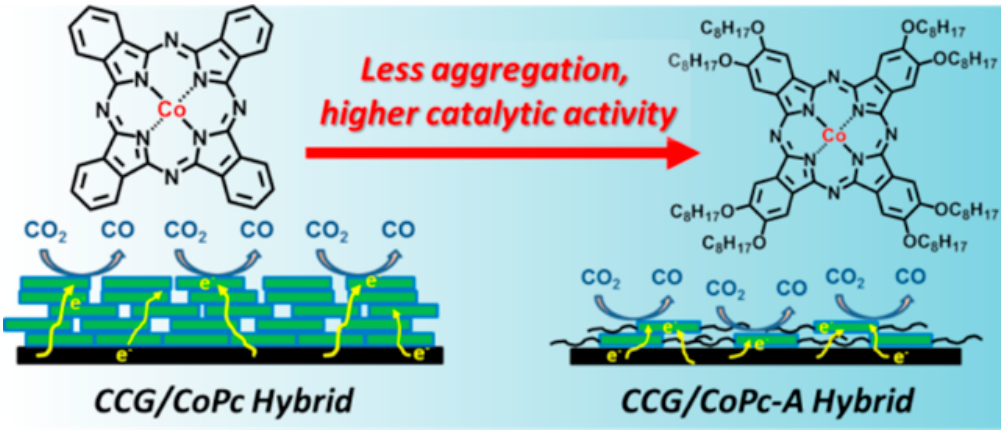

Fig. 1-10. Increased catalytic activity of CoPc-A due to less aggregation. The modified CoPc-A has additional long carbon chains attached to each outer ring which prevents the close packing of multiple CoPc molecules. Image reproduced from ref. 91.

The strategy of modifying CoPc with axial ligands also shows promise in achieving higher activity of CO_2 reduction. Research in this area has shown that CoPc modified with ligands attached at the Co center can change the electronic characteristics of the catalyst.[92] This hypothesis

was tested by synthesizing ligand-modified CoPc molecules, with eight different ligands of varying σ-electron donor strength. This variable offered a direct observation of the impact of ligand-derived electron donation on the catalytic activity of CoPc. The eight different ligands chosen are referred to as L1 through L8, where L1 = 1,3,5-triazine, L2 = pyrazine, L3 = pyridine, L4 = pyridazine, L5 = imidazole, L6 = 4-methylpyridine, L7 = 1-methyl imidazole, and L8 = 4-(dimethylamino)pyridine. The findings showed an increase in CO_2RR activity with increasing σ-donor strength of the axial ligand. Using DFT, it was found that axial coordination has the effect of increasing the energy of the dz^2 orbital of Co, and that the experimentally observed activity increase is correlated to an increased extent of charge transfer from the reduced CoPc-L complex to adsorbed CO_2. However, more exploration of the reaction steps beyond CO_2 to CO are necessary to make this ligand modified catalyst relevant for methanol production. This knowledge gap leaves an opportunity for further research that describes the effect of axial ligand coordination on the *CO intermediate, which is where our own work contributes.

1.3. Research Goals

Increasing atmospheric CO_2 continues to be one of our most pressing global challenges, and technological advances in catalytic CO_2 reduction methods offer a ripe field of research to address this problem. The goal of the research presented in this dissertation is to elucidate the trends of catalyst activity and selectivity for CO_2 reduction catalysts, especially as they apply to the dependence on catalyst structure at the atomic level. To this end, we explore single-atom catalyst systems relevant to thermal catalysis, plasma catalysis, and electrocatalysis via density functional theory modeling. Our objectives are summarized as follows:

1. Define structural models of single-atom catalysts that represent active catalyst sites relevant at reaction conditions.

2. Evaluate the adsorption strength of reactants, products, and intermediates for these catalyst models.
3. Relate these adsorption properties to likely reaction mechanisms by way of transition state calculations and microkinetic modeling.
4. Compare modeled results to experimental knowledge to rationalize the observed trends.

This dissertation is divided into five chapters at outlined below:

Chapter 1: Introduction and Background

This chapter explores the current state of research into catalytic CO_2 reduction to value-added chemicals. Focus is granted toward single atom and nanocluster catalysts. A general overview is provided for thermocatalysis, plasma catalysis, and electrocatalysis.

Chapter 2: Thermocatalytic Reverse Water Gas Shift Reaction via Rhodium Single-Atom Catalysts Compared to Nanoclusters

This chapter explores the mechanism for the thermocatalytic reverse water gas shift reaction (RWGSR, $CO_2 + H_2 \rightleftharpoons CO + H_2O$) catalyzed by rhodium single atoms supported on titania (Rh_1/TiO_2). By investigating the potential candidates for single atom active sites, three mechanisms are proposed and compared through density functional theory and microkinetic modeling. We also compare the single atom to different models of supported nanoclusters of varying size ($Rh_2 – Rh_8$). The main findings suggest that a reaction mechanism involving oxygen vacancies within the TiO_2 support offers a more reactive pathway for CO_2 reduction than a pristine TiO_2 surface. Additionally, single atoms are uniquely selective toward RWGSR over methanation due to weak binding of CO and limited availability for binding additional H_2 for further hydrogenation.

Chapter 3: Plasma-induced Surface Charge Effects on CO_2 Activation by Supported Single Atom Catalysts

This chapter elucidates the effect of plasma-induced surface charge on the CO_2 reduction reaction. Using DFT modeling, we assemble a net neutral system with excess negative charge on the surface and a positive countercharge in the vacuum above, modeling both the imparted surface charge from plasma as well as the strong electric field present. We model CO_2 adsorption strength and dissociation barriers for six different single metal atoms on both reducible and irreducible supports to elucidate trends. The findings show that accumulated surface charge on the single atom increases the CO_2 adsorption strength and decreases the CO_2 dissociation barrier for all studied single atom/support combinations. Our study demonstrates that surface charging should be considered in strong electric fields because it can have a large effect on molecule chemisorption and bond-breaking on catalytic surfaces.

Chapter 4: Electrocatalytic CO_2 Conversion via Molecular Catalyst Cobalt Phthalocyanine

This chapter provides an investigation into the capability of cobalt phthalocyanine (CoPc) to catalyze the CO_2 reduction reaction as a ligand-modified electrocatalyst. Previous literature demonstrates the capacity for CO production by CoPc, but recent research shows that a single-batch reaction to methanol is also possible. We model CoPc with eight different ligands of varying electron donor strength to determine the trend with CO_2 and CO adsorption. We include three different reduction states to compare results to different proposed mechanisms for CO_2 reduction. The trend with CO adsorption shows a reverse trend with respect to ligand electron donation strength compared to adsorption of CO_2. This finding shows that a careful choice of ligand must be made that optimizes for strong CO_2 adsorption and a moderate CO adsorption.

Chapter 5: Conclusion and Outlook

This chapter summarizes the key findings of my research and reviews how each research objective was addressed. Further discussion is given toward the future outlook for CO_2 reduction in research and industry, advances in modeling strategies, and data science approaches for accelerating catalyst discovery.

1.4 References

(1) Boden, T.; Andres, R.; Marland, G. Global, Regional, and National Fossil-Fuel CO2 Emissions (1751 - 2014) (V. 2017), 2017. https://doi.org/10.3334/cdiac/00001_v2017.

(2) *The Keeling Curve*. The Keeling Curve. http://scripps.ucsd.edu/programs/keelingcurve (accessed 2022-08-18).

(3) Hemminger, J.; Fleming, G.; Ratner, M. *Directing Matter and Energy: Five Challenges for Science and the Imagination*; DOESC (USDOE Office of Science (SC)), 2007. https://doi.org/10.2172/935427.

(4) Song, C. Global Challenges and Strategies for Control, Conversion and Utilization of CO_2 for Sustainable Development Involving Energy, Catalysis, Adsorption and Chemical Processing. *Catalysis Today* **2006**, *115* (1–4), 2–32. https://doi.org/10.1016/j.cattod.2006.02.029.

(5) Matsubu, J. C.; Yang, V. N.; Christopher, P. Isolated Metal Active Site Concentration and Stability Control Catalytic CO_2 Reduction Selectivity. *Journal of the American Chemical Society* **2015**, *137* (8), 3076–3084. https://doi.org/10.1021/ja5128133.

(6) Chen, X.; Su, X.; Su, H.-Y.; Liu, X.; Miao, S.; Zhao, Y.; Sun, K.; Huang, Y.; Zhang, T. Theoretical Insights and the Corresponding Construction of Supported Metal Catalysts for Highly Selective CO_2 to CO Conversion. *ACS Catalysis* **2017**, *7* (7), 4613–4620. https://doi.org/10.1021/acscatal.7b00903.

(7) Jeong, H.; Lee, G.; Kim, B.-S.; Bae, J.; Han, J. W.; Lee, H. Fully Dispersed Rh Ensemble Catalyst To Enhance Low-Temperature Activity. *J. Am. Chem. Soc.* **2018**, *140* (30), 9558–9565. https://doi.org/10.1021/jacs.8b04613.

(8) Wang, H.; Liu, J.-X.; Allard, L. F.; Lee, S.; Liu, J.; Li, H.; Wang, J.; Wang, J.; Oh, S. H.; Li, W.; Flytzani-Stephanopoulos, M.; Shen, M.; Goldsmith, B. R.; Yang, M. Surpassing the Single-Atom Catalytic Activity Limit through Paired Pt-O-Pt Ensemble Built from Isolated Pt 1 Atoms. *Nature Communications* **2019**, *10* (1), 3808. https://doi.org/10.1038/s41467-019-11856-9.

(9) Hvolbæk, B.; Janssens, T. V. W.; Clausen, B. S.; Falsig, H.; Christensen, C. H.; Nørskov, J. K. Catalytic Activity of Au Nanoparticles. *Nano Today* **2007**, *2* (4), 14–18. https://doi.org/10.1016/S1748-0132(07)70113-5.

(10) Liu, L.; Corma, A. Metal Catalysts for Heterogeneous Catalysis: From Single Atoms to Nanoclusters and Nanoparticles. *Chem. Rev.* **2018**, *118* (10), 4981–5079. https://doi.org/10.1021/acs.chemrev.7b00776.

(11) Fernández, E.; Liu, L.; Boronat, M.; Arenal, R.; Concepcion, P.; Corma, A. Low-Temperature Catalytic NO Reduction with CO by Subnanometric Pt Clusters. *ACS Catal.* **2019**, *9* (12), 11530–11541. https://doi.org/10.1021/acscatal.9b03207.

(12) Liu, L.; Meira, D. M.; Arenal, R.; Concepcion, P.; Puga, A. V.; Corma, A. Determination of the Evolution of Heterogeneous Single Metal Atoms and Nanoclusters under Reaction Conditions: Which Are the Working Catalytic Sites? *ACS Catal.* **2019**, *9* (12), 10626–10639. https://doi.org/10.1021/acscatal.9b04214.

(13) Tang, Y.; Asokan, C.; Xu, M.; Graham, G. W.; Pan, X.; Christopher, P.; Li, J.; Sautet, P. Rh Single Atoms on TiO 2 Dynamically Respond to Reaction Conditions by Adapting Their Site. *Nat Commun* **2019**, *10* (1), 4488. https://doi.org/10.1038/s41467-019-12461-6.

(14) Tosoni, S.; Pacchioni, G. Influence of Surface Hydroxylation on the Ru Atom Diffusion on the ZrO2(101) Surface: A DFT Study. *Surface Science* **2017**, *664*, 87–94. https://doi.org/10.1016/j.susc.2017.06.005.

(15) Wan, Q.; Wei, F.; Wang, Y.; Wang, F.; Zhou, L.; Lin, S.; Xie, D.; Guo, H. Single Atom Detachment from Cu Clusters, and Diffusion and Trapping on CeO 2 (111): Implications in Ostwald Ripening and Atomic Redispersion. *Nanoscale* **2018**, *10* (37), 17893–17901. https://doi.org/10.1039/C8NR06232C.
(16) De, S.; Dokania, A.; Ramirez, A.; Gascon, J. Advances in the Design of Heterogeneous Catalysts and Thermocatalytic Processes for CO2 Utilization. *ACS Catal.* **2020**, *10* (23), 14147–14185. https://doi.org/10.1021/acscatal.0c04273.
(17) Imteyaz Alam, M.; Cheula, R.; Moroni, G.; Nardi, L.; Maestri, M. Mechanistic and Multiscale Aspects of Thermo-Catalytic CO 2 Conversion to C 1 Products. *Catalysis Science & Technology* **2021**, *11* (20), 6601–6629. https://doi.org/10.1039/D1CY00922B.
(18) Mehta, P.; Barboun, P.; Go, D. B.; Hicks, J. C.; Schneider, W. F. Catalysis Enabled by Plasma Activation of Strong Chemical Bonds: A Review. *ACS Energy Lett.* **2019**, *4* (5), 1115–1133. https://doi.org/10.1021/acsenergylett.9b00263.
(19) Bogaerts, A.; Tu, X.; Whitehead, J. C.; Centi, G.; Lefferts, L.; Guaitella, O.; Azzolina-Jury, F.; Kim, H.-H.; Murphy, A. B.; Schneider, W. F.; Nozaki, T.; Hicks, J. C.; Rousseau, A.; Thevenet, F.; Khacef, A.; Carreon, M. The 2020 Plasma Catalysis Roadmap. *J. Phys. D: Appl. Phys.* **2020**, *53* (44), 443001. https://doi.org/10.1088/1361-6463/ab9048.
(20) Zhang, S.; Fan, Q.; Xia, R.; Meyer, T. J. CO2 Reduction: From Homogeneous to Heterogeneous Electrocatalysis. *Acc. Chem. Res.* **2020**, *53* (1), 255–264. https://doi.org/10.1021/acs.accounts.9b00496.
(21) Zhang, J.; Cai, W.; Xin Hu, F.; Yang, H.; Liu, B. Recent Advances in Single Atom Catalysts for the Electrochemical Carbon Dioxide Reduction Reaction. *Chemical Science* **2021**, *12* (20), 6800–6819. https://doi.org/10.1039/D1SC01375K.
(22) Su, Y.-Q.; Liu, J.-X.; Filot, I. A. W.; Hensen, E. J. M. Theoretical Study of Ripening Mechanisms of Pd Clusters on Ceria. *Chem. Mater.* **2017**, *29* (21), 9456–9462. https://doi.org/10.1021/acs.chemmater.7b03555.
(23) Ouyang, R.; Liu, J.-X.; Li, W.-X. Atomistic Theory of Ostwald Ripening and Disintegration of Supported Metal Particles under Reaction Conditions. *J. Am. Chem. Soc.* **2013**, *135* (5), 1760–1771. https://doi.org/10.1021/ja3087054.
(24) Goldsmith, B. R.; Sanderson, E. D.; Ouyang, R.; Li, W.-X. CO- and NO-Induced Disintegration and Redispersion of Three-Way Catalysts Rhodium, Palladium, and Platinum: An Ab Initio Thermodynamics Study. *J. Phys. Chem. C* **2014**, *118* (18), 9588–9597. https://doi.org/10.1021/jp502201f.
(25) Su, Y.-Q.; Wang, Y.; Liu, J.-X.; Filot, I. A. W.; Alexopoulos, K.; Zhang, L.; Muravev, V.; Zijlstra, B.; Vlachos, D. G.; Hensen, E. J. M. Theoretical Approach To Predict the Stability of Supported Single-Atom Catalysts. *ACS Catal.* **2019**, *9* (4), 3289–3297. https://doi.org/10.1021/acscatal.9b00252.
(26) Matsubu, J. C.; Yang, V. N.; Christopher, P. Isolated Metal Active Site Concentration and Stability Control Catalytic CO2 Reduction Selectivity. *J. Am. Chem. Soc.* **2015**, *137* (8), 3076–3084. https://doi.org/10.1021/ja5128133.
(27) Wang, Y.-G.; Mei, D.; Glezakou, V.-A.; Li, J.; Rousseau, R. Dynamic Formation of Single-Atom Catalytic Active Sites on Ceria-Supported Gold Nanoparticles. *Nature Communications* **2015**, *6* (1), 6511. https://doi.org/10.1038/ncomms7511.
(28) Agnelli, M.; Kolb, M.; Mirodatos, C. Co Hydrogenation on a Nickel Catalyst .: 1. Kinetics and Modeling of a Low-Temperature Sintering Process. *Journal of Catalysis* **1994**, *148* (1), 9–21. https://doi.org/10.1006/jcat.1994.1180.

(29) Goodman, E. D.; Johnston-Peck, A. C.; Dietze, E. M.; Wrasman, C. J.; Hoffman, A. S.; Abild-Pedersen, F.; Bare, S. R.; Plessow, P. N.; Cargnello, M. Catalyst Deactivation via Decomposition into Single Atoms and the Role of Metal Loading. *Nat Catal* **2019**, *2* (9), 748–755. https://doi.org/10.1038/s41929-019-0328-1.
(30) Liu, L.; Zakharov, D. N.; Arenal, R.; Concepcion, P.; Stach, E. A.; Corma, A. Evolution and Stabilization of Subnanometric Metal Species in Confined Space by in Situ TEM. *Nature Communications* **2018**, *9* (1), 574. https://doi.org/10.1038/s41467-018-03012-6.
(31) Xi, W.; Wang, K.; Shen, Y.; Ge, M.; Deng, Z.; Zhao, Y.; Cao, Q.; Ding, Y.; Hu, G.; Luo, J. Dynamic Co-Catalysis of Au Single Atoms and Nanoporous Au for Methane Pyrolysis. *Nat Commun* **2020**, *11* (1), 1919. https://doi.org/10.1038/s41467-020-15806-8.
(32) Moliner, M.; Gabay, J. E.; Kliewer, C. E.; Carr, R. T.; Guzman, J.; Casty, G. L.; Serna, P.; Corma, A. Reversible Transformation of Pt Nanoparticles into Single Atoms inside High-Silica Chabazite Zeolite. *J. Am. Chem. Soc.* **2016**, *138* (48), 15743–15750. https://doi.org/10.1021/jacs.6b10169.
(33) Gänzler, A. M.; Casapu, M.; Vernoux, P.; Loridant, S.; Cadete Santos Aires, F. J.; Epicier, T.; Betz, B.; Hoyer, R.; Grunwaldt, J.-D. Tuning the Structure of Platinum Particles on Ceria In Situ for Enhancing the Catalytic Performance of Exhaust Gas Catalysts. *Angew. Chem. Int. Ed.* **2017**, *56* (42), 13078–13082. https://doi.org/10.1002/anie.201707842.
(34) Goguet, A.; Hardacre, C.; Harvey, I.; Narasimharao, K.; Saih, Y.; Sa, J. Increased Dispersion of Supported Gold during Methanol Carbonylation Conditions. *J. Am. Chem. Soc.* **2009**, *131* (20), 6973–6975. https://doi.org/10.1021/ja9021705.
(35) Sá, J.; Goguet, A.; Taylor, S. F. R.; Tiruvalam, R.; Kiely, C. J.; Nachtegaal, M.; Hutchings, G. J.; Hardacre, C. Influence of Methyl Halide Treatment on Gold Nanoparticles Supported on Activated Carbon. *Angew. Chem.* **2011**, *123* (38), 9074–9078. https://doi.org/10.1002/ange.201102066.
(36) Sá, J.; Taylor, S. F. R.; Daly, H.; Goguet, A.; Tiruvalam, R.; He, Q.; Kiely, C. J.; Hutchings, G. J.; Hardacre, C. Redispersion of Gold Supported on Oxides. *ACS Catal.* **2012**, *2* (4), 552–560. https://doi.org/10.1021/cs300074g.
(37) Feng, S.; Song, X.; Liu, Y.; Lin, X.; Yan, L.; Liu, S.; Dong, W.; Yang, X.; Jiang, Z.; Ding, Y. In Situ Formation of Mononuclear Complexes by Reaction-Induced Atomic Dispersion of Supported Noble Metal Nanoparticles. *Nat Commun* **2019**, *10* (1), 5281. https://doi.org/10.1038/s41467-019-12965-1.
(38) Sidgwick, N. V. The Electronic Theory of Valency. *Journal of the Society of Chemical Industry* **1928**, *47* (8), 226–227. https://doi.org/10.1002/jctb.5000470815.
(39) Mitchell, P. R.; Parish, R. V. The Eighteen Electron Rule. *J. Chem. Educ.* **1969**, *46* (12), 811. https://doi.org/10.1021/ed046p811.
(40) Millet, M.-M.; Algara-Siller, G.; Wrabetz, S.; Mazheika, A.; Girgsdies, F.; Teschner, D.; Seitz, F.; Tarasov, A.; Levchenko, S. V.; Schlögl, R.; Frei, E. Ni Single Atom Catalysts for CO_2 Activation. *J. Am. Chem. Soc.* **2019**, *141* (6), 2451–2461. https://doi.org/10.1021/jacs.8b11729.
(41) Jones, J.; Xiong, H.; DeLaRiva, A. T.; Peterson, E. J.; Pham, H.; Challa, S. R.; Qi, G.; Oh, S.; Wiebenga, M. H.; Pereira Hernandez, X. I.; Wang, Y.; Datye, A. K. Thermally Stable Single-Atom Platinum-on-Ceria Catalysts via Atom Trapping. *Science* **2016**, *353* (6295), 150–154. https://doi.org/10.1126/science.aaf8800.
(42) Resasco, J.; DeRita, L.; Dai, S.; Chada, J. P.; Xu, M.; Yan, X.; Finzel, J.; Hanukovich, S.; Hoffman, A. S.; Graham, G. W.; Bare, S. R.; Pan, X.; Christopher, P. Uniformity Is Key in

Defining Structure–Function Relationships for Atomically Dispersed Metal Catalysts: The Case of Pt/CeO 2. *J. Am. Chem. Soc.* **2019**, *142* (1), 169–184. https://doi.org/10.1021/jacs.9b09156.
(43) Figueroba, A.; Kovács, G.; Bruix, A.; Neyman, K. M. Towards Stable Single-Atom Catalysts: Strong Binding of Atomically Dispersed Transition Metals on the Surface of Nanostructured Ceria. *Catal. Sci. Technol.* **2016**, *6* (18), 6806–6813. https://doi.org/10.1039/C6CY00294C.
(44) Ravel, B. Composing Complex EXAFS Problems with Severe Information Constraints. *J. Phys.: Conf. Ser.* **2009**, *190*, 012026. https://doi.org/10.1088/1742-6596/190/1/012026.
(45) Ren, Y.; Tang, Y.; Zhang, L.; Liu, X.; Li, L.; Miao, S.; Su, D. S.; Wang, A.; Li, J.; Zhang, T. Unraveling the Coordination Structure-Performance Relationship in Pt 1 /Fe 2 O 3 Single-Atom Catalyst. *Nat Commun* **2019**, *10* (1), 4500. https://doi.org/10.1038/s41467-019-12459-0.
(46) Zhai, H.; Alexandrova, A. N. Fluxionality of Catalytic Clusters: When It Matters and How to Address It. *ACS Catal.* **2017**, *7* (3), 1905–1911. https://doi.org/10.1021/acscatal.6b03243.
(47) Vilhelmsen, L. B.; Hammer, B. A Genetic Algorithm for First Principles Global Structure Optimization of Supported Nano Structures. *The Journal of Chemical Physics* **2014**, *141* (4), 044711. https://doi.org/10.1063/1.4886337.
(48) Jennings, P. C.; Lysgaard, S.; Hummelshøj, J. S.; Vegge, T.; Bligaard, T. Genetic Algorithms for Computational Materials Discovery Accelerated by Machine Learning. *npj Computational Materials* **2019**, *5* (1), 46. https://doi.org/10.1038/s41524-019-0181-4.
(49) Rondina, G. G.; Da Silva, J. L. F. Revised Basin-Hopping Monte Carlo Algorithm for Structure Optimization of Clusters and Nanoparticles. *J. Chem. Inf. Model.* **2013**, *53* (9), 2282–2298. https://doi.org/10.1021/ci400224z.
(50) Wexler, R. B.; Qiu, T.; Rappe, A. M. Automatic Prediction of Surface Phase Diagrams Using Ab Initio Grand Canonical Monte Carlo. *J. Phys. Chem. C* **2019**, *123* (4), 2321–2328. https://doi.org/10.1021/acs.jpcc.8b11093.
(51) Liu, J.-X.; Su, Y.; Filot, I. A. W.; Hensen, E. J. M. A Linear Scaling Relation for CO Oxidation on CeO2-Supported Pd. *J. Am. Chem. Soc.* **2018**, *140* (13), 4580–4587. https://doi.org/10.1021/jacs.7b13624.
(52) Guo, H.; Sautet, P.; Alexandrova, A. N. Reagent-Triggered Isomerization of Fluxional Cluster Catalyst via Dynamic Coupling. *J. Phys. Chem. Lett.* **2020**, *11* (8), 3089–3094. https://doi.org/10.1021/acs.jpclett.0c00548.
(53) Zandkarimi, B.; Alexandrova, A. N. Dynamics of Subnanometer Pt Clusters Can Break the Scaling Relationships in Catalysis. *J. Phys. Chem. Lett.* **2019**, *10* (3), 460–467. https://doi.org/10.1021/acs.jpclett.8b03680.
(54) Liu, G.; Poths, P.; Zhang, X.; Zhu, Z.; Marshall, M.; Blankenhorn, M.; Alexandrova, A. N.; Bowen, K. H. CO2 Hydrogenation to Formate and Formic Acid by Bimetallic Palladium–Copper Hydride Clusters. *J. Am. Chem. Soc.* **2020**. https://doi.org/10.1021/jacs.0c01855.
(55) Huang, S.-D.; Shang, C.; Liu, Z.-P. Ultrasmall Au Clusters Supported on Pristine and Defected CeO2: Structure and Stability. *J. Chem. Phys.* **2019**, *151* (17), 174702. https://doi.org/10.1063/1.5126187.
(56) Zhai, H.; Alexandrova, A. N. Ensemble-Average Representation of Pt Clusters in Conditions of Catalysis Accessed through GPU Accelerated Deep Neural Network Fitting Global Optimization. *Journal of Chemical Theory and Computation* **2016**, *12* (12), 6213–6226. https://doi.org/10.1021/acs.jctc.6b00994.

(57) Goldsmith, B. R.; Esterhuizen, J.; Liu, J.-X.; Bartel, C. J.; Sutton, C. Machine Learning for Heterogeneous Catalyst Design and Discovery. *AIChE J.* **2018**, *64* (7), 2311–2323. https://doi.org/10.1002/aic.16198.
(58) Graciani, J.; Mudiyanselage, K.; Xu, F.; Baber, A. E.; Evans, J.; Senanayake, S. D.; Stacchiola, D. J.; Liu, P.; Hrbek, J.; Sanz, J. F.; Rodriguez, J. A. Highly Active Copper-Ceria and Copper-Ceria-Titania Catalysts for Methanol Synthesis from CO2. *Science* **2014**, *345* (6196), 546–550. https://doi.org/10.1126/science.1253057.
(59) Chen, X.; Su, X.; Su, H.-Y.; Liu, X.; Miao, S.; Zhao, Y.; Sun, K.; Huang, Y.; Zhang, T. Theoretical Insights and the Corresponding Construction of Supported Metal Catalysts for Highly Selective CO_2 to CO Conversion. *ACS Catal.* **2017**, *7* (7), 4613–4620. https://doi.org/10.1021/acscatal.7b00903.
(60) Lin, W.; Stocker, K. M.; Schatz, G. C. Mechanisms of Hydrogen-Assisted CO_2 Reduction on Nickel. *J. Am. Chem. Soc.* **2017**, *139* (13), 4663–4666. https://doi.org/10.1021/jacs.7b01538.
(61) Li, S.; Xu, Y.; Chen, Y.; Li, W.; Lin, L.; Li, M.; Deng, Y.; Wang, X.; Ge, B.; Yang, C.; Yao, S.; Xie, J.; Li, Y.; Liu, X.; Ma, D. Tuning the Selectivity of Catalytic Carbon Dioxide Hydrogenation over Iridium/Cerium Oxide Catalysts with a Strong Metal–Support Interaction. *Angewandte Chemie International Edition* **2017**, *56* (36), 10761–10765. https://doi.org/10.1002/anie.201705002.
(62) Wang, Y.; Arandiyan, H.; Scott, J.; Aguey-Zinsou, K.-F.; Amal, R. Single Atom and Nanoclustered Pt Catalysts for Selective CO_2 Reduction. *ACS Appl. Energy Mater.* **2018**, *1* (12), 6781–6789. https://doi.org/10.1021/acsaem.8b00817.
(63) Aitbekova, A.; Wu, L.; Wrasman, C. J.; Boubnov, A.; Hoffman, A. S.; Goodman, E. D.; Bare, S. R.; Cargnello, M. Low-Temperature Restructuring of CeO_2 -Supported Ru Nanoparticles Determines Selectivity in CO_2 Catalytic Reduction. *J. Am. Chem. Soc.* **2018**, *140* (42), 13736–13745. https://doi.org/10.1021/jacs.8b07615.
(64) Back, S.; Lim, J.; Kim, N.-Y.; Kim, Y.-H.; Jung, Y. Single-Atom Catalysts for CO_2 Electroreduction with Significant Activity and Selectivity Improvements. *Chem. Sci.* **2017**, *8* (2), 1090–1096. https://doi.org/10.1039/C6SC03911A.
(65) Kwak, J. H.; Kovarik, L.; Szanyi, J. Heterogeneous Catalysis on Atomically Dispersed Supported Metals: CO2 Reduction on Multifunctional Pd Catalysts. *ACS Catal.* **2013**, *3* (9), 2094–2100. https://doi.org/10.1021/cs4001392.
(66) Matsubu, J. C.; Zhang, S.; DeRita, L.; Marinkovic, N. S.; Chen, J. G.; Graham, G. W.; Pan, X.; Christopher, P. Adsorbate-Mediated Strong Metal–Support Interactions in Oxide-Supported Rh Catalysts. *Nature Chemistry* **2017**, *9* (2), 120–127. https://doi.org/10.1038/nchem.2607.
(67) Yao, S.; Lin, L.; Liao, W.; Rui, N.; Li, N.; Liu, Z.; Cen, J.; Zhang, F.; Li, X.; Song, L.; Betancourt De Leon, L.; Su, D.; Senanayake, S. D.; Liu, P.; Ma, D.; Chen, J. G.; Rodriguez, J. A. Exploring Metal–Support Interactions To Immobilize Subnanometer Co Clusters on γ–Mo_2N: A Highly Selective and Stable Catalyst for CO_2 Activation. *ACS Catal.* **2019**, *9* (10), 9087–9097. https://doi.org/10.1021/acscatal.9b01945.
(68) Mehta, P.; Barboun, P. M.; Engelmann, Y.; Go, D. B.; Bogaerts, A.; Schneider, W. F.; Hicks, J. C. Plasma-Catalytic Ammonia Synthesis beyond the Equilibrium Limit. *ACS Catal.* **2020**, *10* (12), 6726–6734. https://doi.org/10.1021/acscatal.0c00684.

(69) Mehta, P.; Barboun, P.; Herrera, F. A.; Kim, J.; Rumbach, P.; Go, D. B.; Hicks, J. C.; Schneider, W. F. Overcoming Ammonia Synthesis Scaling Relations with Plasma-Enabled Catalysis. *Nat Catal* **2018**, *1* (4), 269–275. https://doi.org/10.1038/s41929-018-0045-1.
(70) Xu, S.; Chen, H.; Hardacre, C.; Fan, X. Non-Thermal Plasma Catalysis for CO2 Conversion and Catalyst Design for the Process. *J. Phys. D: Appl. Phys.* **2021**, *54* (23), 233001. https://doi.org/10.1088/1361-6463/abe9e1.
(71) Whitehead, J. C. Plasma–Catalysis: The Known Knowns, the Known Unknowns and the Unknown Unknowns. *J. Phys. D: Appl. Phys.* **2016**, *49* (24), 243001. https://doi.org/10.1088/0022-3727/49/24/243001.
(72) Chen, G.; Georgieva, V.; Godfroid, T.; Snyders, R.; Delplancke-Ogletree, M.-P. Plasma Assisted Catalytic Decomposition of CO2. *Applied Catalysis B: Environmental* **2016**, *190*, 115–124. https://doi.org/10.1016/j.apcatb.2016.03.009.
(73) Neyts, E. C. Atomistic Simulations of Plasma Catalytic Processes. *Front. Chem. Sci. Eng.* **2018**, *12* (1), 145–154. https://doi.org/10.1007/s11705-017-1674-7.
(74) Engelmann, Y.; van 't Veer, K.; Gorbanev, Y.; Neyts, E. C.; Schneider, W. F.; Bogaerts, A. Plasma Catalysis for Ammonia Synthesis: A Microkinetic Modeling Study on the Contributions of Eley–Rideal Reactions. *ACS Sustainable Chem. Eng.* **2021**, *9* (39), 13151–13163. https://doi.org/10.1021/acssuschemeng.1c02713.
(75) Bal, K. M.; Bogaerts, A.; Neyts, E. C. Ensemble-Based Molecular Simulation of Chemical Reactions under Vibrational Nonequilibrium. *J. Phys. Chem. Lett.* **2020**, *11* (2), 401–406. https://doi.org/10.1021/acs.jpclett.9b03356.
(76) Bal, K. M.; Neyts, E. C. Quantifying the Impact of Vibrational Nonequilibrium in Plasma Catalysis: Insights from a Molecular Dynamics Model of Dissociative Chemisorption. *J. Phys. D: Appl. Phys.* **2021**, *54* (39), 394004. https://doi.org/10.1088/1361-6463/ac113a.
(77) Ma, H.; Sharma, R. K.; Welzel, S.; van de Sanden, M. C. M.; Tsampas, M. N.; Schneider, W. F. Observation and Rationalization of Nitrogen Oxidation Enabled Only by Coupled Plasma and Catalyst. *Nat Commun* **2022**, *13* (1), 402. https://doi.org/10.1038/s41467-021-27912-2.
(78) Bal, K. M.; Huygh, S.; Bogaerts, A.; Neyts, E. C. Effect of Plasma-Induced Surface Charging on Catalytic Processes: Application to CO_2 Activation. *Plasma Sources Sci. Technol.* **2018**, *27* (2), 024001. https://doi.org/10.1088/1361-6595/aaa868.
(79) Jafarzadeh, A.; Bal, K. M.; Bogaerts, A.; Neyts, E. C. CO2 Activation on TiO2-Supported Cu5 and Ni5 Nanoclusters: Effect of Plasma-Induced Surface Charging. *J. Phys. Chem. C* **2019**, *123* (11), 6516–6525. https://doi.org/10.1021/acs.jpcc.8b11816.
(80) Neyts, E. C. Plasma-Surface Interactions in Plasma Catalysis. *Plasma Chem Plasma Process* **2016**, *36* (1), 185–212. https://doi.org/10.1007/s11090-015-9662-5.
(81) Neyts, E. C.; Ostrikov, K. (Ken); Sunkara, M. K.; Bogaerts, A. Plasma Catalysis: Synergistic Effects at the Nanoscale. *Chem. Rev.* **2015**, *115* (24), 13408–13446. https://doi.org/10.1021/acs.chemrev.5b00362.
(82) Neyts, E. C.; Bogaerts, A. Understanding Plasma Catalysis through Modelling and Simulation—a Review. *J. Phys. D: Appl. Phys.* **2014**, *47* (22), 224010. https://doi.org/10.1088/0022-3727/47/22/224010.
(83) Lin, S.; Diercks, C. S.; Zhang, Y.-B.; Kornienko, N.; Nichols, E. M.; Zhao, Y.; Paris, A. R.; Kim, D.; Yang, P.; Yaghi, O. M.; Chang, C. J. Covalent Organic Frameworks Comprising Cobalt Porphyrins for Catalytic CO2 Reduction in Water. *Science* **2015**, *349* (6253), 1208–1213. https://doi.org/10.1126/science.aac8343.

(84) Hod, I.; Sampson, M. D.; Deria, P.; Kubiak, C. P.; Farha, O. K.; Hupp, J. T. Fe-Porphyrin-Based Metal–Organic Framework Films as High-Surface Concentration, Heterogeneous Catalysts for Electrochemical Reduction of CO2. *ACS Catal.* **2015**, *5* (11), 6302–6309. https://doi.org/10.1021/acscatal.5b01767.
(85) Costentin, C.; Savéant, J.-M. Homogeneous Molecular Catalysis of Electrochemical Reactions: Catalyst Benchmarking and Optimization Strategies. *J. Am. Chem. Soc.* **2017**, *139* (24), 8245–8250. https://doi.org/10.1021/jacs.7b02879.
(86) Lieber, C. M.; Lewis, N. S. Catalytic Reduction of Carbon Dioxide at Carbon Electrodes Modified with Cobalt Phthalocyanine. *J. Am. Chem. Soc.* **1984**, *106* (17), 5033–5034. https://doi.org/10.1021/ja00329a082.
(87) Kapusta, S.; Hackerman, N. Carbon Dioxide Reduction at a Metal Phthalocyanine Catalyzed Carbon Electrode. *J. Electrochem. Soc.* **1984**, *131* (7), 1511. https://doi.org/10.1149/1.2115882.
(88) Wu, Y.; Jiang, Z.; Lu, X.; Liang, Y.; Wang, H. Domino Electroreduction of CO2 to Methanol on a Molecular Catalyst. *Nature* **2019**, *575* (7784), 639–642. https://doi.org/10.1038/s41586-019-1760-8.
(89) Chen, X.; Hu, X.-M.; Daasbjerg, K.; Ahlquist, M. S. G. Understanding the Enhanced Catalytic CO2 Reduction upon Adhering Cobalt Porphyrin to Carbon Nanotubes and the Inverse Loading Effect. *Organometallics* **2020**, *39* (9), 1634–1641. https://doi.org/10.1021/acs.organomet.9b00726.
(90) Chen, X.; Wei, D.; Ahlquist, M. S. G. Aggregation and Significant Difference in Reactivity Therein: Blocking the CO2-to-CH3OH Reaction. *Organometallics* **2021**, *40* (17), 3087–3093. https://doi.org/10.1021/acs.organomet.1c00431.
(91) Choi, J.; Wagner, P.; Gambhir, S.; Jalili, R.; MacFarlane, D. R.; Wallace, G. G.; Officer, D. L. Steric Modification of a Cobalt Phthalocyanine/Graphene Catalyst To Give Enhanced and Stable Electrochemical CO_2 Reduction to CO. *ACS Energy Lett.* **2019**, *4* (3), 666–672. https://doi.org/10.1021/acsenergylett.8b02355.
(92) Rivera Cruz, K. E.; Liu, Y.; Soucy, T. L.; Zimmerman, P. M.; McCrory, C. C. L. Increasing the CO2 Reduction Activity of Cobalt Phthalocyanine by Modulating the σ-Donor Strength of Axially Coordinating Ligands. *ACS Catal.* **2021**, *11* (21), 13203–13216. https://doi.org/10.1021/acscatal.1c02379.

Chapter 2

Thermocatalytic Reverse Water Gas Shift Reaction via Rhodium Single-Atom Catalysts Compared to Nanoclusters

This chapter was adapted from F. Doherty and B. R. Goldsmith, "Rhodium Single-Atom Catalysts on Titania for Reverse Water Gas Shift Reaction Explored by First Principles Mechanistic Analysis and Compared to Nanoclusters*." ChemCatChem*, 2021, **13**, 3155–3164.

2.1 Introduction

The size of supported nanoparticles affects catalytic performance for many reactions, such as CO oxidation,[1] methane activation,[2] and CO_2 reduction.[3,4] Taking this size-dependent catalytic phenomenon to the limit, researchers have been developing atomically dispersed (i.e., single atom) catalysts, which frequently show modified activity and selectivity relative to their larger nanocluster (< 2 nm) or nanoparticle counterparts.[5–8] Importantly, atomically dispersed catalysts can also achieve the maximum possible dispersion of metal on a support, making optimal use of rare and expensive metals.

In some cases, atomically dispersed catalysts are more active or selective than nanoclusters. For example, the direct conversion of methane to methanol was achieved with high selectivity by using atomically dispersed rhodium supported on titanium dioxide (Rh_1/TiO_2).[9] In other cases, nanoclusters display higher activity than atomically dispersed catalysts (e.g., Pt/CeO_2 for low-temperature CO oxidation).[10] Nevertheless, the activity and selectivity differences between

nanoclusters and their atomically dispersed counterparts are not well-understood for many reactions.[11]

One reaction where atomically dispersed catalysts and their corresponding nanoclusters have shown different activity and selectivity is the thermocatalytic reduction of CO_2 by H_2, which has become an intensively studied area of research because of environmental concerns.[12,13] Thermocatalytic CO_2 reduction can occur via the reverse water gas shift reaction (rWGSR, $CO_2 + H_2 \rightleftharpoons CO + H_2O$) or catalytic methanation ($CO_2 + 4H_2 \rightleftharpoons CH_4 + 2H_2O$) depending on the reaction conditions and catalyst. Methanol synthesis from the hydrogenation of CO_2 is also an important reaction for improving the chemical industry's environmental impact,[11] but is hindered by the competing rWGSR.

Notably, the activity and selectivity of CO_2 reduction to products such as methane and CO depends strongly on the metal catalyst size.[4,14,15] In particular, CO_2 reduction by Rh/TiO_2 displays a strong selectivity dependence between CO vs. CH_4 on the fraction of atomically dispersed Rh_1 relative to Rh nanoclusters. Correlations were observed between catalytic methanation turnover frequency (TOF) and the fraction of Rh nanoclusters, and between the TOF of the rWGSR and the fraction of Rh_1 species.[3] These Rh_1 species can be synthesized via techniques such as strong electrostatic adsorption[16–18] and atomic layer deposition,[19,20] or can spontaneously form via Rh nanocluster disintegration under reaction conditions.[21–27] The Rh_1 species are typically detected as gem-dicarbonyl $Rh_1(CO)_2$ complexes via diffuse reflectance Fourier transform infrared spectroscopy (DRIFTS)[3,28] and may anchor on the surface oxygen or in oxygen vacancies on metal oxide supports.[29–32] Stable Rh_1 species coexist with Rh particles on TiO_2 with ratios that depend on the loading percent of Rh, temperature, and gas composition.

The large difference in selectivity between Rh_1 species and Rh nanoclusters toward the rWGSR (**Fig. 2-1**) is not well-understood at the atomic level, in part due to a lack of knowledge of the precise active sites and elementary reaction steps. Several rWGSR mechanisms for Rh_1 on vacancy-free anatase $TiO_2(101)$ were explored based on electronic energies predicted using density functional theory (DFT) modeling.[33] The high selectivity of Rh_1 toward CO was proposed to arise from a lack of orbital overlap between the highest occupied molecular orbital of Rh_1 and the lowest unoccupied molecular orbital of H_2, which prevents H_2 adsorption on Rh_1 while CO is bound and halts the reaction before hydrogenation to CH_4.[33] However, the predicted rWGSR mechanism includes a large activation barrier of 1.9 eV for the second elementary hydrogenation step to form the CO and H_2O from the commonly proposed carboxyl (*COOH) intermediate.[34,35] Ir_1/FeO_x, Ru_1/Al_2O_3, and Pt_1/FeO_x have similar TOFs as Rh_1/TiO_2 for CO_2 reduction (i.e., TOF of 0.005–0.03 s^{-1} at 473 K),[3] with measured apparent activation energies around 0.52–0.82 eV between 270–350 K,[36,37] suggesting alternative reaction pathways or different Rh_1 catalytic sites may be responsible for the observed activity and selectivity differences compared with Rh nanoclusters. Further atomistic modeling of the rWGSR on Rh_1/TiO_2 and Rh nanoclusters would clarify the origin for the rWGSR activity and selectivity differences with particle size.

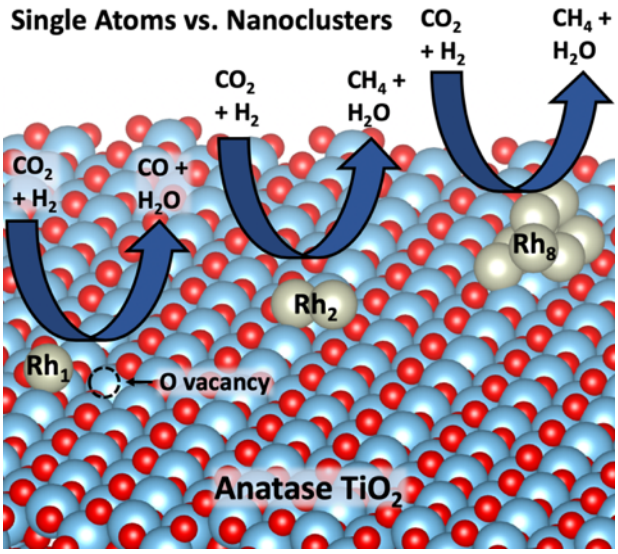

Fig. 2-1. Illustration of the Rh/TiO_2 catalyst for CO_2 reduction. The thermocatalytic reduction of CO_2 + H_2 by Rh/TiO_2 proceeds via two competing reaction mechanisms depending on whether single atoms or nanoclusters are used. Single atoms promote the reverse water gas shift reaction to create CO, while clusters tend toward the methanation reaction to create CH_4. The cluster size and local environment around the metal active site have an impact on the reaction mechanisms involved.

Here we report first-principles modeling studies of Rh_1 sites and small Rh_x nanoclusters (x = 2–8) on anatase TiO_2 to understand the activity of Rh_1 sites toward rWGSR and to explain the high selectivity of Rh_1 toward rWGSR compared to nanoclusters (**Fig. 2-1**). Plausible Rh_1 active sites on anatase TiO_2 for rWGSR are identified based on DFT-predicted formation energies, gem-dicarbonyl vibrational frequency analysis, and microkinetic modeling. Rh_1 near an oxygen vacancy at a three-fold coordinated site (Rh_1 near O_{3c}vac) is predicted to be the most active Rh_1 site because the nearby oxygen vacancy helps activate CO_2, yielding faster kinetics than proceeding through a *COOH intermediate. Rh_1 species on TiO_2 are found to be more selective toward rWGSR than Rh_x/TiO_2 nanoclusters because (i) CO adsorbs weaker to Rh and has a stronger C-O bond strength on all Rh_1 sites compared with nanoclusters, and (ii) Rh_1 active sites have a higher barrier for H_2 dissociation and adsorb hydrogen weaker than nanoclusters. The Rh_1 sites are predicted to be unique in their ability to have high selectivity toward CO even compared to Rh_2 dimers.

2.2 Computational Methods

DFT calculations. All DFT calculations were conducted using the Vienna Ab initio Simulation Package.[38–40] Electron-ion interactions were treated with the projector augmented-wave method.[41] Anatase TiO_2(101) was studied because the anatase phase is more stable than rutile for high-surface area particles smaller than ~14 nm.[42,43] The (101) surface was selected because it is the most abundant facet of the anatase surface.[44] A five-layer thick anatase TiO_2(101) slab (1×3 surface, 174 atoms total) with a 20 Å vacuum layer was built in the Atomic Simulation Environment (ASE).[45] Bulk experimental lattice constants of 3.78 Å (*a*, *b*) and 9.51 Å (*c*) were specified for the TiO_2(101) model.[46] The bottom two layers of the TiO_2(101) slab were fixed in the position of the bulk lattice, whereas the top three layers could relax during geometry optimization. The (134) surface, which exhibits (100)-like facets between steps, was chosen as a step-edge model. The (134) model was constructed as a 1×3 periodic surface slab that was three layers thick (192 atoms total). The top two layers of the (134) slab could relax during geometry optimization. Dipole corrections were included in the *z* direction for each model surface. A plane wave basis set with a cutoff energy of 340 eV was selected after benchmarking. The *k*-space was sampled using a 4×4×1 Monkhorst-Pack grid. Transition states were found using the Climbing Image Nudged Elastic Band method.[47]

The PBE+U functional with the D3 dispersion[48] correction was used for all calculations.[49,50] DFT using only PBE fails to describe the strong on-site Coulomb interaction of localized *d*-electrons in TiO_2, so a U value of 2.5 eV was chosen to reproduce the reaction energy of O vacancy formation in TiO_2,[50] which is important for the catalytic systems studied here.

Formation energies and binding energies were calculated using:

$$\Delta E_f = E_{ads/Rh/TiO_2} - (E_{TiO_2} + E_{bulk} + E_{mol(g)}) \qquad \text{(Eq. 2-1)}$$

$$\Delta E_b = E_{ads/Rh/TiO_2} - (E_{Rh/TiO_2} + E_{mol(g)}) \qquad \text{(Eq. 2-2)}$$

Here ΔE_f is the formation energy of a single-atom-adsorbate complex (e.g., $Rh_1(CO)_2/TiO_2$), $E_{ads/Rh/TiO_2}$ is the DFT-calculated electronic energy of the single-atom-adsorbate complex, E_{TiO_2} is the energy of the TiO_2 surface (including an O vacancy, Ti vacancy, or OH group if present), E_{bulk} is the per-atom energy of Rh in the bulk face-centered cubic crystal, $E_{mol(g)}$ is the energy of the adsorbate molecule(s) in the gas phase, ΔE_b is the binding energy of an adsorbate to Rh_x/TiO_2, and E_{Rh/TiO_2} is the energy of the Rh_x/TiO_2 system itself. The bulk Rh was constructed using the optimized lattice constant of 3.816 Å (*a*, *b*, *c*).

The strength of the C-O bond for adsorbed CO was calculated as:

$$E_{C-O} = (E_{Rh-CO} + E_{H_2(g)}) - (E_{Rh-C} + E_{H_2O(g)}) \qquad \text{(Eq. 2-3)}$$

where E_{C-O} is the C-O bond energy, E_{Rh-CO} is the binding energy of CO on the supported Rh species, E_{Rh-C} is the binding energy of atomic C on Rh, and $E_{H_2(g)}$ and $E_{H_2O(g)}$ are the gas-phase electronic energies of hydrogen and water. Using this formula, the energy difference between bound CO and dissociated C and O is found, resulting in the C-O bond strength. H_2 and H_2O are chosen as the gas phase reference states for removing O from CO, since the reaction occurs under reducing conditions with plentiful H_2(g).

Reported Gibbs free energies (ΔG) used in free energy diagrams and microkinetic modeling include ideal-gas corrections for molecular rotations, translations, and vibrations, as well as hindered rotation and vibration of the adsorbed species (as implemented in the ASE package). Vibrational frequencies for Gibbs free energy calculations and for comparison with DRIFTS were computed within the harmonic approximation. The gas phase CO vibrational frequency calculated using PBE was 2103 cm^{-1}, which is about 40 cm^{-1} lower than the experimentally measured value

of 2143 cm^{-1}.[51] For comparison with experimental DRIFTS measurements, a 40 cm^{-1} rigid shift was applied to all calculated vibrational frequencies for adsorbed CO to correct for this difference.

Nanocluster geometry search. A genetic algorithm (GA) was used to search the structure of supported Rh_x nanoclusters (x = 4–8 atoms) on anatase TiO_2(101). The GA is based on an implementation in ASE.[52,53] The positions and structures of Rh_1, Rh_2, and Rh_3 on TiO_2(101) were manually searched. The general workflow for the GA is represented in **Fig. 2-2** and described in further detail below.

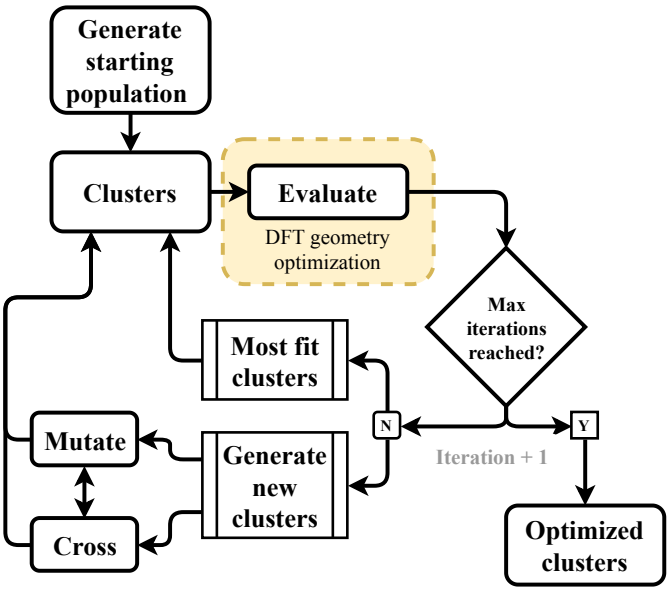

Fig. 2-2. Workflow summarizing the genetic algorithm for the global optimization of supported nanoclusters. Initially, a starting population of clusters is generated, which are then evaluated by DFT-based geometry optimization. The clusters are next evolved via mutate and crossover operations and the new clusters have their energies evaluated using DFT. This cycle is repeated until either the number of max iterations is reached, or no new low-energy structures are found.

For each GA search, the starting population contained 12 randomly generated Rh_x structures. Next, DFT calculations were performed to evaluate the total electronic energy of each Rh_x structure in the population. All the atoms in Rh_x nanoclusters were relaxed during GA calculations, but a one-layer TiO_2(101) support was fixed during the GA algorithm. Mutation and cross-over operations were applied to existing structures in the population to generate new

structures.[52] The calculated total electronic energy was used to evaluate the fitness of each nanocluster's structure. The fitness function of i^{th} candidate (F_i) is:

$$F_i = ½[1 - \tanh(2\rho_i - 1)] \qquad \text{(Eq. 2-4)}$$

$$\rho_i = (E_i - E_{min})/(E_{max} - E_{min}) \qquad \text{(Eq. 2-5)}$$

where E_i is the energy of the i^{th} candidate, and E_{max} and E_{min} denote the maximum and minimum energy of any structure in the population. Each structure has a probability of being selected for a crossover operation based on its fitness value divided by the sum fitness of the total generation. Each generation had a total of 12 different structures to analyze. New structures are generated by the crossover operation and used to fill out a new generation. There is also a 30% probability of mutation occurring, where one cluster will be randomly rotated or one atom in the cluster will be translated in space, and then this cluster is added to the population for fitness evaluation. The process continues until no new lowest energy structures are found within 1000 structures tested via DFT or after 80 generations, whichever comes first. Repeated runs of the GA with different initial populations reidentified the same ground-state structures of the Rh_x nanoclusters. Final structures were re-optimized on a full 6-layer TiO_2 slab (changes in each cluster structure were minimal upon re-optimization).

Microkinetic simulations. First-principles mean-field microkinetic simulations[54] of the rWGSR were conducted to predict TOFs, apparent activation barriers, and the degree of rate control (DRC)[55] for plausible Rh_1/TiO_2 sites and reaction mechanisms. All microkinetic simulations used the MKMCXX code.[56] The DFT-based microkinetic simulation approach that we use has been presented in detail elsewhere,[56,57] so here we summarize only the main points. The DFT-calculated forward and backward activation energies were used to calculate the rate constant of each elementary step. For surface reactions, the rate constant of step *i* was calculated using the

Arrhenius equation. Differential equations for all the reaction species were built using the predicted rate and equilibrium constants and the set of elementary steps. The rates of the elementary steps were computed based on the steady-state coverages. Steady-state surface coverages were determined by integrating the differential equations in time until changes in the surface coverages were less than 10^{-8}. In our simulations, the gas phase consisted of CO_2 and H_2 in a 1:4 molar ratio at a total pressure of 1 atm, within the range of typical experimental reaction conditions.[58]

Forward and backward reaction rate constants were computed using the DFT-calculated activation barriers. For surface reactions, forward and backward rate constants for each step were determined by the Arrhenius equation:

$$k = Ae^{\frac{\Delta G^{\ddagger}}{k_b T}} \qquad \text{(Eq. 2-6)}$$

where k is the reaction rate constant of step i in s^{-1}. Here k_b, T, and $\Delta G^{\ddagger}$ are the Boltzmann constant, temperature, and the activation free energy barrier, respectively. The pre-factor A is approximated as 10^{13} s^{-1} for all surface reactions, approximately equal to $\frac{k_b T}{h}$ for the temperature range 400-500 K, where h is Planck's constant. $\Delta G^{\ddagger}$ for surface reactions include the hindered rotational and vibrational entropy and enthalpy of each bound intermediate calculated at 400 K to enable comparison with measurements in literature.[3]

The rate of molecular adsorption is determined by the Hertz-Knudsen equation:

$$k_{ads} = \frac{pA'}{\sqrt{2\pi m k_b T}} S \qquad \text{(Eq. 2-7)}$$

where p is the partial pressure of adsorbate in the gas phase, A' is the surface area of the adsorption site, m is the mass of the adsorbate molecule and S is the sticking coefficient. A' is approximated as 1.0 $Å^2$ (10^{-20} m^2), and S is assumed to be 1.0.

The rate of desorption considers the added entropy from the adsorbate returning to the gas phase. There are assumed to be three rotational degrees of freedom and two translational degrees of freedom in the transition state. Thus, the rate of desorption is given by:

$$k_{des} = \frac{k_b T^3}{h^3} \frac{A'(2\pi k_b)}{\sigma \theta_{rot}} e^{-\frac{E_{des}}{k_b T}} \qquad \text{(Eq. 2-8)}$$

where σ is the symmetry number, θ_{rot} is the characteristic temperature for rotation, and E_{des} is the electronic desorption energy from DFT (without zero-point correction).

Differential equations for all the surface reaction intermediates were constructed using the rate constants and the set of elementary reaction steps. The elementary and overall reaction rates, reaction intermediate coverages, degrees of rate control, and apparent activation barriers were calculated by the MKMCXX program.

2.3 Results and Discussion

2.3.1 Atomically dispersed Rh_1 catalysts for rWGSR

Rh_1 binding locations on TiO_2. The feasible Rh_1 binding locations must first be known to understand the activity and selectivity of Rh_1/TiO_2 toward the rWGSR. Atomically dispersed Rh_1 is known to change its coordination environment on anatase and rutile TiO_2 depending on the reaction conditions.[32,59] A recent study identified plausible sites for Rh_1 binding on anatase TiO_2(101) under CO + H_2 reducing conditions using DFT and Fourier-transform infrared spectroscopy (FTIR), specifically $Rh_1(CO)_2$ bound to two, two-fold coordinated oxygen atoms (O_{2c}) with and without a nearby Ti-OH group.[32] Herein we build on this prior work and expand the set of structures considered as plausible Rh_1/TiO_2 sites, including anatase surfaces with oxygen vacancies and stepped sites.

We identify plausible binding locations for Rh_1 on anatase TiO_2 at zero Kelvin under vacuum based on DFT-computed formation energies and gem-dicarbonyl vibrational frequency

analysis. The systems considered were: Rh_1 on clean $TiO_2(101)$, Rh_1 on the $TiO_2(134)$ step edge, Rh_1 occupying O vacancies at the two-fold coordinated ($@O_{2c}vac$) and three-fold coordinated ($@O_{3c}vac$) sites, Rh_1 occupying a Ti vacancy at the five-fold coordinated site ($@Ti_{5c}vac$), and Rh_1 with O vacancies nearby and far away. Rh_1 with a nearby hydroxyl group on TiO_2 [$Rh_1OH/TiO_2(101)$] as proposed by Asokan *et al*.[32] is also considered.

The bare Rh_1 systems considered all have highly endothermic formation energies. In the presence of CO, the gem-dicarbonyl $Rh_1(CO)_2$ complexes (**Fig. 2-3**) are much more stable than bare Rh_1 species. The $Rh_1(CO)_2$ are readily detected via DRIFTS to probe the Rh_1 site environments and thus are considered in detail for stability and vibrational frequency analysis.[60–64]

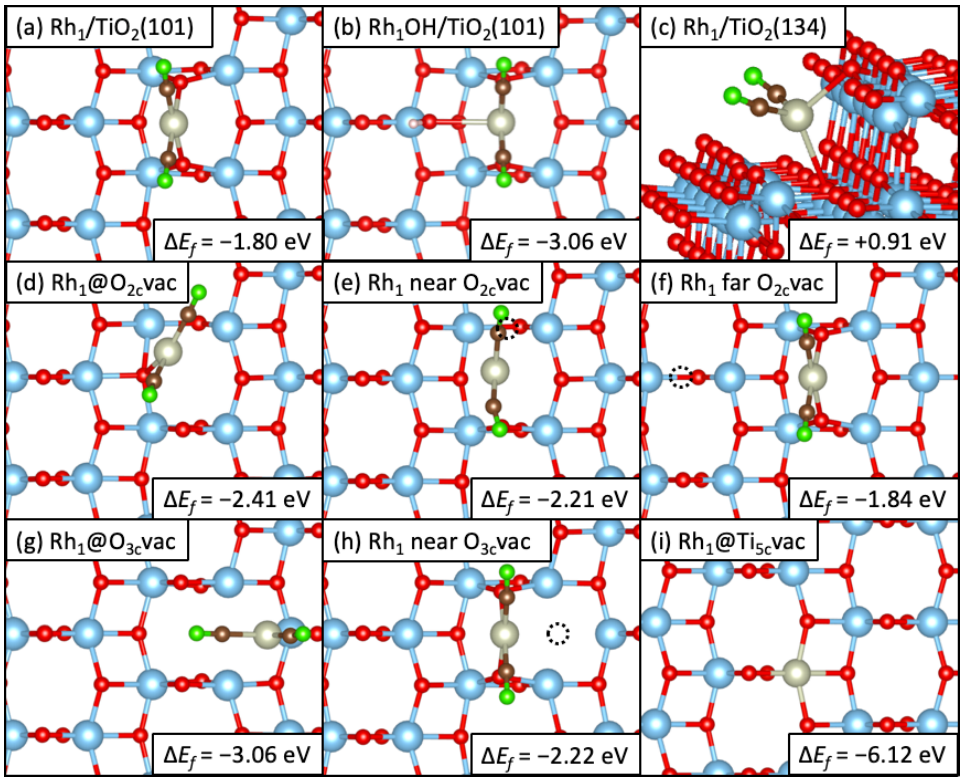

Fig. 2-3. Rh_1/TiO_2 system geometries. Top view of the gem-dicarbonyl $Rh_1(CO)_2$ binding locations on anatase TiO_2, along with their formation energy (ΔE_f) relative to a bare TiO_2 surface (defect-free, defective, or step, as relevant), Rh bulk lattice, and gaseous CO. The systems considered were: (a) Rh_1 on $TiO_2(101)$, (b) Rh_1 on $TiO_2(101)$ with a nearby hydroxyl group, (c) Rh_1 on the $TiO_2(134)$ step edge, (d) Rh_1 occupying an O vacancy at the two-fold

coordinated site (@O_{2c}vac) on TiO_2(101), (e) Rh_1 with an O_{2c}vac nearby on TiO_2(101), (f) Rh_1 with an O_{2c}vac far away on TiO_2(101), (g) Rh_1 occupying an O vacancy at the three-fold coordinated site (@O_{3c}vac) on TiO_2(101), (h) Rh_1 near a O_{3c}vac on TiO_2(101) and (i) Rh_1 in a Ti vacancy at the five-fold coordinated site (@Ti_{5c}vac) on TiO_2(101). Oxygen vacancies are denoted with dashed circles. Atom color legend: Blue = Ti, Red = O, Gray = Rh, Green = O in CO, Brown = C.

The $Rh_1(CO)_2$ formation energy on a defect-free TiO_2(101) surface, where Rh_1 is bound through two surface oxygens (**Fig. 2-3a**) is exothermic (–1.80 eV). This $Rh_1(CO)_2/TiO_2$ complex is the same structure as that suggested in recent work based on DRIFTS, temperature programmed desorption, and DFT.[32] Experimentally, the $Rh_1(CO)_2$ structure exhibits two peaks around 2097 and 2028 cm^{-1}, being the symmetric and asymmetric C-O bond stretches, respectively.[3,65] Vibrational stretches of 2080 cm^{-1} and 2027 cm^{-1} for $Rh_1(CO)_2$ on TiO_2(101) (**Fig. 2-4**) are predicted, similar to experiment and prior DFT vibrational frequency assignment.[32]

When considering a TiO_2 surface with nearby hydroxyl group (Rh_1OH), the Rh_1 binding location does not change from the clean surface (**Fig. 2-3b**). The formation energy is also very exothermic (–3.06 eV). The calculated vibrational frequencies of 2093 cm^{-1} and 2026 cm^{-1} match closely with experimental values (**Fig. 2-4**), differing only by 4 cm^{-1} and 1 cm^{-1}, respectively. These vibrational frequency predictions agree well with the prior study by Asokan *et al*.[32]

In contrast, the formation energy of the $Rh_1(CO)_2/TiO_2$(134) step edge is highly endothermic (0.91 eV, **Fig. 2-3c**). Besides having an endothermic formation energy, $Rh_1(CO)_2/TiO_2$(134) was also ruled out as an abundant surface species by incompatible vibrational frequencies compared with experiment (**Fig. 2-4**), namely 1973 and 1941 cm^{-1}.

Examining the effect of oxygen vacancies on the Rh_1/TiO_2 system is important because they may participate in activating CO_2 for the rWGSR.[64,66,67] An oxygen vacancy would allow for an alternative mechanism for CO_2 dissociation into *CO and *O to heal the vacancy, bypassing any *COOH intermediate. Subsurface oxygen vacancies were measured by scanning tunneling microscopy in anatase TiO_2 under reducing conditions similar to those used for CO_2 reduction.[68,69]

Supported Rh_1 has been shown via temperature programmed reduction to promote the formation of O vacancies within a P25 TiO_2 support, which is approximately 75% anatase and 25% rutile.[70] For (101) anatase, O vacancies were predicted by DFT to preferentially exist in the subsurface.[69,71] However, these O vacancies may diffuse throughout the lattice under reaction conditions.[71,72] Because of the mobility of O vacancies, both O_{2c}vac (**Figs. 2-3d–f**) and O_{3c}vac (**Figs. 2-3g,h**) surface vacancies are considered. The Rh_1 inside Ti vacancies (**Fig. 2-3i**) likely have low abundance in the strong reducing environment of rWGSR. Further, the formation energy is strongly negative for Rh_1 filling Ti vacancies, and they are not predicted to form Rh_1-dicarbonyl complexes because of their saturated coordination environment;[32,59] thus we do not consider Ti vacancies further as active Rh_1 sites.

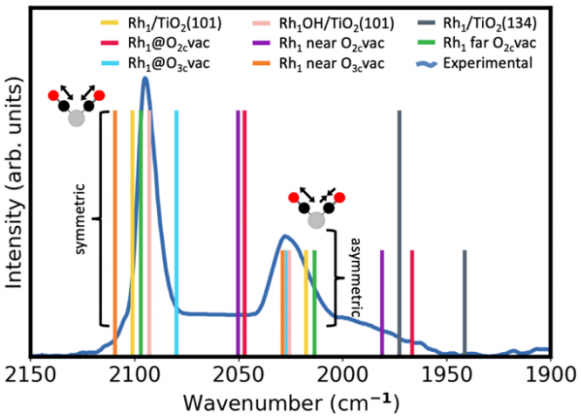

Fig. 2-4. Experimental DRIFTS spectroscopy and DFT-predicted CO stretching frequencies under the harmonic approximation for $Rh_1(CO)_2$ systems. The two peaks observed are for symmetric (high intensity peak) and asymmetric (low intensity peak) stretches of CO. Note, only the peak positions as computed by DFT are reported and the intensities are arbitrarily specified for clarity. The experimental DRIFTS spectra (300 K, 10% CO/90% Ar) is reproduced from Ref. 3. The experimental DRIFTS used P25, which is a mixture of 75% anatase and 25% rutile TiO_2.

The data in **Fig. 2-4** shows calculated IR stretching frequencies for each considered $Rh_1(CO)_2/TiO_2$ system compared with experimental DRIFTS from Matsubu *et al.*[3] Rh_1@O_{2c}vac or near an O_{2c}vac, and the Rh_1/TiO_2(134) step edge all have frequencies far from experimentally observed values, and thus may not be present in appreciable abundance. Remaining plausible

binding locations based on $Rh_1(CO)_2$ formation energies and vibrational frequency analysis are $Rh_1@O_{3c}$vac, Rh_1 near O_{3c}vac, Rh_1/TiO_2, and Rh_1OH/TiO_2. In particular, the Rh_1OH system agrees most closely with experiment, differing by less than 0.2% for both symmetric and asymmetric stretches. The $Rh_1/TiO_2(101)$ and $Rh_1OH/TiO_2(101)$ structures have been proposed previously as stable adsorption sites and potential active sites on anatase TiO_2,[32,33] but Rh_1 near O_{3c}vac and $Rh_1@O_{3c}$vac have not been studied in detail. In addition, with the exception of $Rh_1/TiO_2(101)$,[33] none of these species have had their rWGSR mechanism modeled via first-principles microkinetic modeling. We note that although CO-DRIFTS probes Rh_1 sites accessible by CO, which may be active sites for CO_2 reduction, it is possible that these sites are not fully representative of the distribution of sites present in $CO_2 + H_2$ reaction conditions.

Microkinetic modeling of rWGSR on plausible Rh_1/TiO_2 active sites. Based on having exothermic gem-dicarbonyl formation energies and qualitative agreement with prior experimental CO-DRIFTS peak assignments, the $Rh_1/TiO_2(101)$, $Rh_1OH/TiO_2(101)$, $Rh_1@O_{3c}$vac, and Rh_1 near O_{3c}vac are plausible active sites for rWGSR. However, we do not consider $Rh_1@O_{3c}$vac further because CO_2 is weakly bound by this site, and the barrier for CO_2 dissociation is computed to be large (1.30 eV) compared to Rh_1 near O_{3c}vac (0.21 eV). To clarify the activity differences among the remaining single-atom species, DFT-based microkinetic modeling of the rWGSR reaction mechanism is performed.

CO_2 hydrogenation to CO can proceed through a carboxyl intermediate (*COOH), which further reacts with *H to form water and CO. Alternatively, the $*CO_2$ can dissociate directly into *CO and *O by C-O bond cleavage, especially when *O is healing an oxygen vacancy on reducible supports such as CeO_2 and TiO_2.[58,73] In either case, *CO will desorb if not allowed to react further.

The selectivity will depend on the binding strength of CO and the availability of nearby *H, both of which vary between Rh_1 and Rh_x.

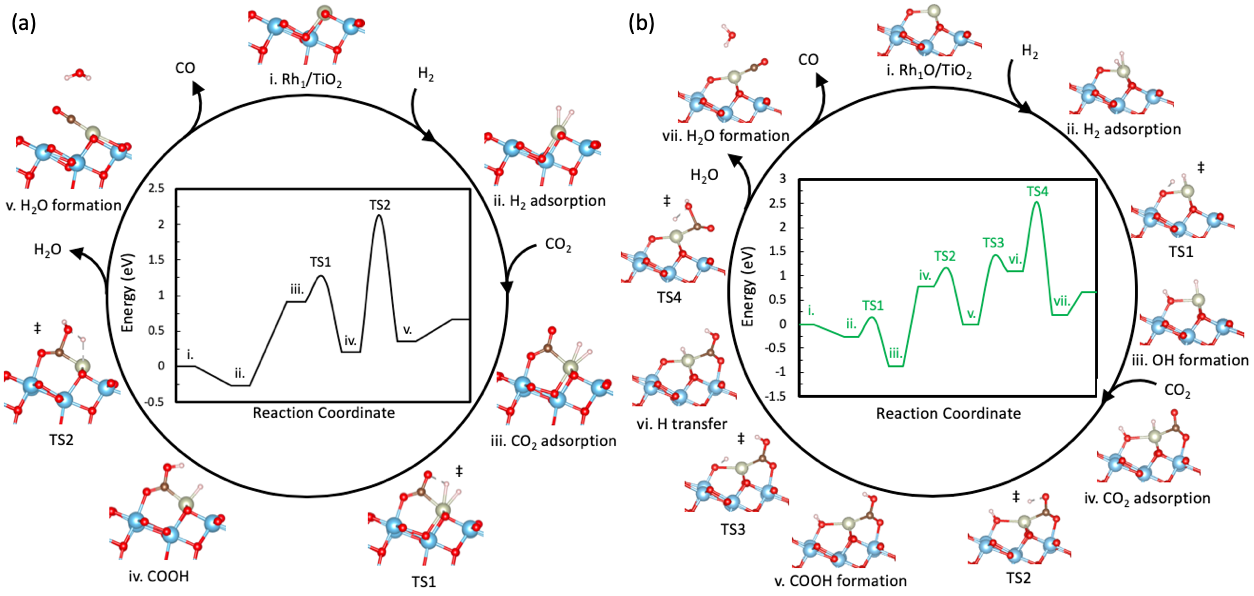

Fig. 2-5. DFT-predicted free-energy diagrams for reverse water gas shift reaction by (a) $Rh_1/TiO_2(101)$ and (b) $Rh_1OH/TiO_2(101)$. Free energies were computed at 400 K and 1 atm total pressure. Atom color legend: Blue = Ti, Red = O, Gray = Rh, Brown = C, White = H.

The free energy diagrams for the rWGSR mechanisms of $Rh_1/TiO_2(101)$ and $Rh_1OH/TiO_2(101)$ are shown in **Fig. 2-5**. The mechanism for $Rh_1/TiO_2(101)$ in **Fig. 2-5a** is the same as the proposed mechanism by Ma and colleagues,[33] with H_2 and CO_2 adsorbing onto Rh_1, followed by H transfer to the oxygen within $*CO_2$ to form *COOH. The second hydrogen transfers to *COOH and reacts to form *CO and water, which is rate controlling (i.e., TS2 in **Fig. 2-5a**, see **Table 2-1** for DRC analysis), where the water is weakly bound and desorbs from the surface. CO then desorbs to complete the cycle. An alternative mechanism was considered where bound *COOH dissociates to form *CO and *OH, followed by CO desorption and *OH hydrogenation to H_2O. This mechanism was predicted to have a lower reaction rate and led to a slightly higher apparent activation barrier.

The mechanism for Rh_1OH/TiO_2 in **Fig. 2-5b** is modeled to form a hydroxyl group next to Rh_1 during the reaction that participates in CO_2 hydrogenation. The starting configuration is similar to that of $Rh_1/TiO_2(101)$, but with an extra O atom adjacent to Rh_1. H_2 adsorbs on Rh_1 and dissociates onto the nearby O, forming the *OH group and Rh-H. CO_2 then adsorbs, and the H bound to Rh_1 transfers to form *COOH. The remaining H of the OH group undergoes a two-step transfer by moving to Rh and then to *COOH to form *CO and H_2O, which is rate controlling (TS4 in **Fig. 2-5b**, see **Table 2-1** for DRC analysis).

Both mechanisms share similarities, with a stable *COOH intermediate forming after one H transfer and a high barrier for the final H transfer to form H_2O. The activity of these two pathways is limited by the large free energy barrier to dissociate *COOH into CO and H_2O, with Rh_1OH further stabilizing the *COOH compared to the Rh_1 without a nearby hydroxyl group. The mechanism proposed here for Rh_1OH creates a system similar to that studied by Asokan *et al*,[32] but it does not observe the same Rh_1OH with bound CO during the reaction itself. Instead, the H from OH is used to hydrogenate *COOH and leaves behind the O atom adjacent to Rh_1. This OH group may exist in different configurations under reaction conditions and CO-DRIFTS conditions.

The free energy diagram for the rWGSR mechanism of Rh_1 near O_{3c}vac is shown in **Fig. 2-6**. The Rh_1 near O_{3c}vac mechanism begins similarly with H_2 adsorption, but then H_2 dissociates onto a nearby lattice oxygen (O_{3c}). When the remaining H reacts with the lattice OH, H_2O is formed and desorbs to leave an oxygen vacancy (O_{3c}vac), which is the step with the largest barrier (0.98 eV) and highest DRC (see **Table 2-1**). CO_2 then adsorbs with one of its oxygen atoms in the vacancy and dissociates to form CO, thereby healing the vacancy. CO desorbs to complete the cycle, as before. Elementary steps of each studied rWGSR mechanism on Rh_1/TiO_2, Rh_1OH/TiO_2, and Rh_1 near O_{3c}vac are provided in the SI.

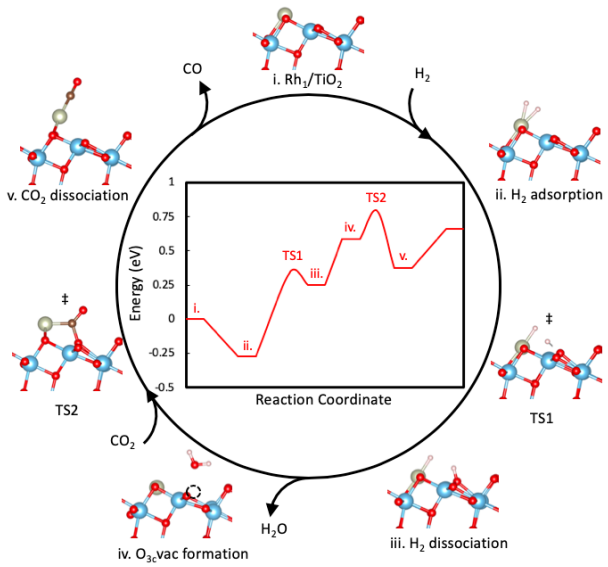

Fig. 2-6. DFT-predicted free-energy diagrams for reverse water gas shift reaction by Rh_1 near O_{3c}vac, which proceeds via CO_2 dissociation assisted by a surface oxygen vacancy. Free energies were computed at 400 K and 1 atm total pressure. Atom color legend: Blue = Ti, Red = O, Gray = Rh, Brown = C, White = H.

The elementary steps used in each constructed microkinetic model are presented below in **Table 2-1**. Forward and reverse barriers are given as input into the microkinetic simulations at 400 K, as well as the corresponding degree of rate control output. The * denotes a Rh_1 site, $O_{lattice}$ denote lattices oxygen in the TiO_2 support, and O_{vac} denotes an oxygen vacancy in the TiO_2 support. Blank cells for forward or reverse barrier refer to reactions that are considered to have no barrier in that direction. Cross references to specific steps in the reaction mechanism refer to **Figs. 2-5** and **2-6**.

Table 2-1. Elementary reaction steps for microkinetic models of $Rh_1/TiO_2(101)$, Rh_1OH/TiO_2 and Rh_1 near O_{3c}vac.

Elementary reaction steps for $Rh_1/TiO_2(101)$ via carboxyl (COOH) mechanism

Elementary Step	Forward barrier	Reverse barrier	Corresponds to Fig. 2-5a	Degree of Rate Control
$H_{2(g)} + * \rightleftharpoons H_2*$	--	0.73 eV	i. → ii.	0.00
$CO_{2(g)} + * \rightleftharpoons CO_2*$	--	0.83 eV	i. → ii. (alt)[a]	0.00
$CO_{2(g)} + H_2* \rightleftharpoons CO_2,H_2*$	--	0.57 eV	ii. → iii.	0.00
$CO_2* + H_{2(g)} \rightleftharpoons CO_2,H_2*$	--	0.47 eV	ii. → iii. (alt)	0.00
$CO_2,H_2* \rightleftharpoons COOH,H*$	0.34 eV	1.05 eV	iii. → TS1 → iv.	0.00

$COOH,H^* \rightleftharpoons CO^* + H_2O_{(g)}$	1.93 eV	1.12 eV	iv. → TS2 → v.	1.00
$CO^* \rightleftharpoons CO_{(g)} + *$	1.87 eV	--	v. → i.	0.00

[a] alt refers to the alternative order of adsorption for CO_2 and H_2. Both are provided in the model to allow for flexibility in the adsorption order.

Elementary reaction steps for Rh_1OH/TiO_2 via carboxyl (COOH) mechanism

Elementary Step	Forward barrier	Reverse barrier	Corresponds to Fig. 2-5b	Degree of Rate Control
$H_{2(g)} + * \rightleftharpoons H_2^*$	--	0.72 eV	i. → ii.	0.00
$H_2^* + O_{lattice} \rightleftharpoons H^* + HO_{lattice}$	0.38 eV	1.00 eV	ii. → TS1 → iii.	0.00
$CO_{2(g)} + H^* + HO_{lattice} \rightleftharpoons CO_2,H,OH^*$	--	0.11 eV	iii. → iv.	0.00
$CO_2,H,OH^* \rightleftharpoons COOH,OH^*$	0.36 eV	1.15 eV	iv. → TS2 → v.	0.00
$COOH,OH^* \rightleftharpoons COOH,H^* + O_{lattice}$	1.39 eV	0.30 eV	v. → TS3 → vi.	0.00
$COOH,H^* \rightleftharpoons CO^* + H_2O_{(g)}$	1.42 eV	1.68 eV	vi. → TS4 → vii.	1.00
$CO^* \rightleftharpoons CO_{(g)} + *$	2.05 eV	--	vii. → i.	0.00

Elementary reaction steps for Rh_1 near O_{3c}vac via CO_2 dissociation mechanism

Elementary Step	Forward barrier	Reverse barrier	Corresponds to Fig. 2-6	Degree of Rate Control
$H_{2(g)} + * \rightleftharpoons H_2^*$	--	0.73 eV	i. → ii.	0.00
$H_2^* + O_{lattice} \rightleftharpoons H^* + HO_{lattice}$	0.62 eV	0.09 eV	ii. → TS1 → iii.	0.00
$H^* + HO_{lattice} \rightleftharpoons H_2O_{(g)} + * + O_{3c}vac$	0.98 eV	--	iii. → iv.	1.00
$CO_{2(g)} + * \rightleftharpoons CO_2^*$	0.21 eV	--	iv. → TS2	0.00
$CO_2^* + O_{3c}vac \rightleftharpoons CO^* + O_{lattice}$	--	2.20 eV	TS2 → v.	0.00
$CO^* \rightleftharpoons CO_{(g)} + *$	1.87 eV	--	v. → i.	0.00

The microkinetic model results in **Fig. 2-7a** show the Rh_1 near O_{3c}vac system outperforming both the Rh_1 species on pristine TiO_2 and Rh_1 near a surface OH group with regards to predicted TOF. CO_2 reduction assisted via an oxygen vacancy has higher TOF by several orders of magnitude for the relevant temperature range of 400–600 K. Experimental observations show a TOF of $10^{-2.3}$ s^{-1} at 473 K, which is within an order of ~100 of the predicted TOF for Rh_1 near O_{3c}vac but 10^6–10^8 times too fast compared to $Rh_1/TiO_2(101)$ and $Rh_1OH/TiO_2(101)$. When comparing apparent activation barriers in **Fig. 2-7b**, the vacancy system again displays relatively close agreement with experiment. The apparent activation barriers show maxima around 500 K

due to a changing degree of rate control for *CO desorption. At higher temperature, *CO desorption becomes more favorable, and the apparent barrier begins to decrease.

Experimentally measured apparent activation barriers range from 1.24 eV at 393–423 K (0.5 wt% Rh, gas mixture 40% H_2, 10% CO_2, 50% He) and 1.07 eV at 473–573 K (0.5 wt% Rh, gas mixture 24% H_2, 6% CO_2, 70% He).[74,75] The $Rh_1/TiO_2(101)$ system has a predicted apparent barrier around 2.0–2.2 eV from 400–600 K, confirming that this previously proposed mechanism does not adequately represent the observed activity of the rWGSR on Rh_1/TiO_2. $Rh_1OH/TiO_2(101)$ likewise shares a high apparent activation barrier around 1.7–2.3 eV. In contrast, the Rh_1 near O_{3c}vac system barrier is 1.3–1.7 eV within the same temperature range, in much closer agreement with experiment.

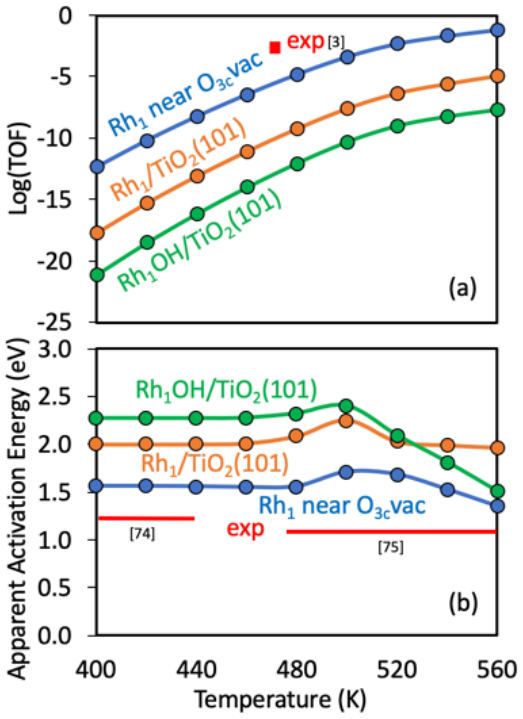

Fig. 2-7. Microkinetic modeling results for reverse water gas shift reaction. Predicted (a) TOF vs. temperature and (b) apparent activation energy vs. temperature for $Rh_1/TiO_2(101)$, Rh_1 near O_{3c}vac, and $Rh_1OH/TiO_2(101)$ based on mean-field microkinetic simulations. CO_2 and H_2 in a 1:4 molar ratio at a total pressure of 1 atm. Experimental data (exp) is shown inset from Ref. 3 for TOFs and Refs. 74,75 for apparent activation barriers over the denoted temperature range (solid red lines).

The Rh_1 through an O_{3c}vac-assisted mechanism was predicted to have the closest agreement with experimental TOF and measured apparent activation barriers. This mechanism depends heavily on the availability of O vacancies at the surface of TiO_2, which will depend on the temperature and reducing conditions. While it is known that subsurface O vacancies are more stable than surface vacancies in anatase TiO_2,[69,76] it has also been suggested that the vacancies are mobile under reaction conditions.[71] Hence, subsurface O vacancies may still play a role in the binding and dissociation of CO_2 by cascading diffusion of O into the lattice. The O_{3c}vac-assisted mechanism shares similarities to what has been investigated for Rh_1 on rutile TiO_2, with oxygen vacancies promoting the direct dissociation of CO_2 to CO.[59]

It is important to note that the experimental samples that we compare against typically include 25% rutile TiO_2, which would offer different Rh_1 binding configurations and active sites, as well as a different abundance of surface oxygen vacancies. Rutile and anatase also exhibit differing amounts of electron transfer between metal and support, which in itself can reverse the observed selectivity.[77] Researchers may seek to minimize these variable support effects when studying rWGSR by using well-defined single atom binding sites such as polyoxometalates (POMs) as a model system for catalytic studies.[78]

2.3.2 Effect of Nanocluster Size on rWGSR Selectivity

The catalytic activity and selectivity of nanoclusters depend on their surface composition, shape, and size.[79–81] Therefore, representative structures of nanoclusters must be known to predict its catalytic performance. Finding the stable and relevant structures of supported metal nanoclusters requires a search of the configuration space, which can be achieved via a GA structure search[52,82,83] or other methods such as stochastic surface walking,[84] basin hopping,[85,86] or replica-exchange molecular dynamics.[87] A GA is selected here for its superior performance in finding the

global minima of nanoclusters compared with methods such as simulated annealing.[88] We emphasize the structures identified here are model structures. The nanoclusters may change their size and shape under reaction conditions, which is not considered in our study. The structure of a given Rh nanocluster in equilibrium with some chemical potentials of reactants could in principle be addressed using techniques such as *ab initio* Grand Canonical Monte Carlo,[83,89] albeit this approach is computationally demanding for nanoclusters and multicomponent reaction conditions.

The predicted structures of the Rh_x single-atom and nanoclusters with one CO adsorbed are shown in **Fig. 2-8**. No major structural rearrangements occurred upon CO adsorption compared with the bare clusters. The optimal CO adsorption configurations were found by sampling 19 different adsorption configurations distributed radially around each cluster. The Rh_2 and Rh_3 clusters are flat against the TiO_2(101) surface with one layer of atoms, and the clusters of four atoms and above are two layers thick. In each case, the bottom layer of Rh atoms prefers to coordinate with oxygen in the TiO_2 lattice.

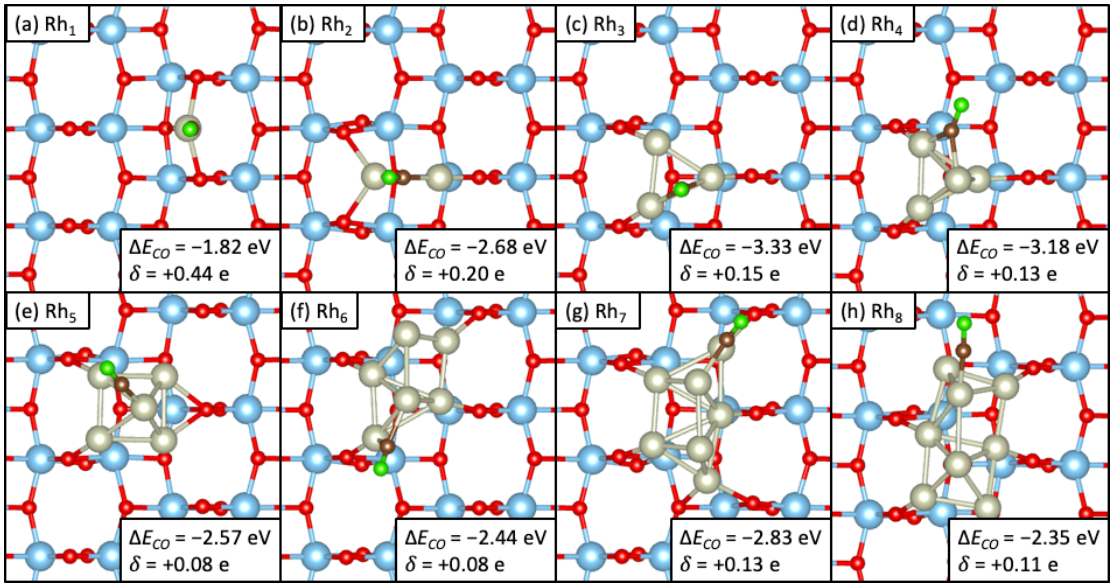

Fig. 2-8. Most stable configurations of Rh_x/TiO_2 (x = 1–8 atoms) with one CO adsorbed. The binding energy of CO (ΔE_{CO}) is given inset, as well as the average Bader charge (δ) of the Rh nanocluster atoms involved in the CO bond. Atom color legend: Blue = Ti, Red = O, Gray = Rh, Green = O in CO, Brown = C.

Bader charge analysis of the atoms in the Rh nanocluster reveals that the atoms in the bottom layer have slight positive charge (+0.01 to +0.55 e) and the top layer atoms have slight negative charge (–0.01 to –0.11 e). Generally, the average Bader charge of the cluster decreases as size increases toward that of bulk Rh (**Fig. 2-9**). CO binds most strongly to the cationic Rh-Rh bridge sites at the support interface, which aligns with prior knowledge that electron donors adsorb strongly to cationic sites at metal/support interfaces.[90,91] The cationic nature of metal atoms at the nanocluster/oxide interface is a well-known phenomenon for Rh/TiO_2[33,92] and other systems such as Pt/SiO_2,[93] Pt/Al_2O_3,[94] and Rh/faujasite.[95]

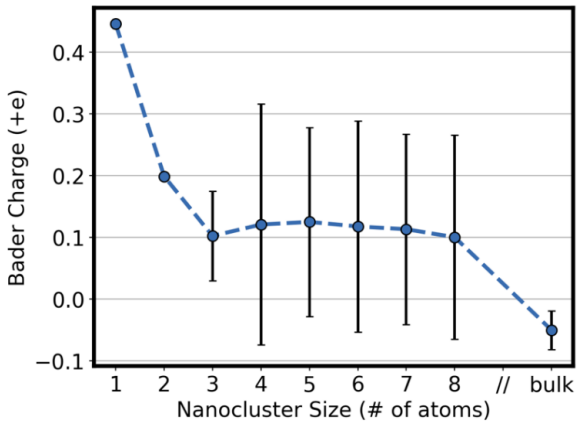

Fig. 2-9. Rh nanocluster characterization by Bader charge analysis. Bader charge is given as an average of all atoms in each cluster (blue dots). Black bars denote the range of atomic charge within each nanocluster.

Atomically dispersed Rh_1 are quite cationic compared to nanoclusters (**Fig. 2-9**). While positive charge is typically beneficial for binding electron donors such as CO, the metal-CO binding strength has been shown to vary on a case-by-case basis due to differences in coordination geometry and the extent of π-back-bonding occurring.[96] In our case, CO prefers to adsorb to Rh-Rh bridge sites on Rh nanoclusters, similarly to bulk Rh, which are not present for Rh_1. The presence of Rh-Rh bridge sites shows a stronger impact on CO binding than positive Bader charge alone. Weaker adsorption of CO on Rh_1 compared with nanoclusters should promote CO desorption before further hydrogenation to CH_4. The relatively weak adsorption of CO on Rh_1

compared with Rh nanoclusters is quite general based on DFT studies of CO adsorption[97] and CO temperature programmed desorption experiments on systems such as Pt/TiO_2,[16] Au/FeO,[98] and Rh/Al_2O_3.[99]

Our calculations predict that the binding energies of CO, CO_2, and H_2 are all relatively weak for Rh_1 compared with the larger Rh_x nanoclusters, **Fig. 2-10**. The adsorbate chemisorption strength increases until Rh_3, then becomes weaker as nanocluster size further increases toward bulk Rh(111). For all cluster sizes, CO is bound more strongly than H_2 and CO_2, owing to its ability to participate in π-back-bonding with the Rh metal.[100] Regardless, all adsorbates follow a similar trend with cluster size, where adsorbate binding is strongest for small undercoordinated clusters that can still offer two- or three-fold sites.

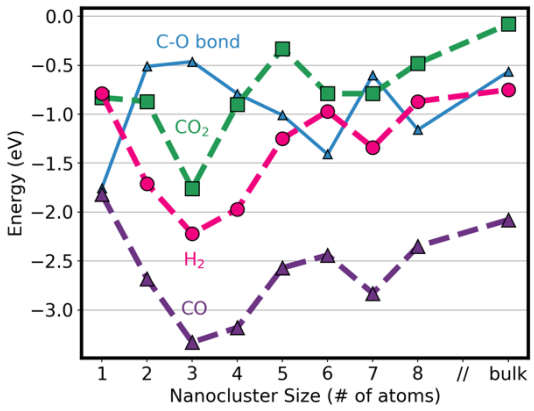

Fig. 2-10. Binding energies (dashed lines) for gaseous species of interest (CO, H_2, CO_2) on Rh_x/TiO_2 (x = 1–8 atoms). Also included is the strength of the C-O bond (solid line) for CO bound to each Rh_x cluster. Energies for the Rh(111) bulk system are provided as the upper limit for nanocluster size. More negative energy indicates a stronger bond.

We report a correlation between nanocluster size and the strength of the C-O bond for CO bound to each Rh nanocluster. **Fig. 2-10** shows that the C-O bond strength decreases from Rh_1 to larger Rh_x (x = 2–8) nanoclusters and Rh(111). The high C-O bond strength for CO adsorbed on Rh_1 compared to nanoclusters is quantitatively similar for all considered Rh_1 sites (within 10% for Rh_1/TiO_2, Rh_1OH/TiO_2 and Rh_1 near O_{3c}vac). The C-O bond strength has been shown previously

to be a descriptor of selectivity to CO for CO_2 reduction by Ir_1 species and nanoclusters.[97] For atomically dispersed catalysts such as Rh_1, in which C-O bond strength is larger than or similar to the CO binding energy, CO desorption is favored over further reduction. Because the C-O bond strength is weakened on Rh nanoclusters (including Rh_2 dimers) and Rh(111) compared to Rh_1 while having high CO adsorption strength, further reaction to products such as methane is favored over CO desorption.

Several examples in experimental studies show the importance of CO binding energy to selectivity.[97] For a Ru/TiO_2 catalyst, changing the support phase from rutile to anatase resulted in an increased amount of hydrogen migrating from metal to support, known as hydrogen spillover. This hydrogen spillover is accompanied by an electron transfer from metal to support, which weakened CO binding to Ru and caused a strong selectivity shift to rWGSR.[77] A related effect has also been observed for Rh/Al_2O_3 catalysts modified with Ni and K, where the Ni and K additives weaken the CO adsorption strength and hinder the rate of methanation.[101]

Another factor that may contribute to the increased CO_2-to-CO selectivity of Rh_1/TiO_2 is the lack of nearby metal sites to dissociate H_2.[3] To test this hypothesis, H_2 dissociation on Rh_2 dimers is predicted for comparison against Rh_1 on defect-free $TiO_2(101)$. H_2 bound to $Rh_1(CO)$ and $Rh_2(CO)$ are chosen as starting points because the methanation reaction depends on the further hydrogenation of bound CO. It is important to consider the CO already bound to Rh, since this would impact the ability to adsorb H_2 and is relevant to determining selectivity between rWGSR and methanation. The activation barrier for H_2 dissociation is calculated for the single atom and dimer systems.

The data in **Fig. 2-11** shows that the activation energy for H_2 dissociation on $Rh_1(CO)$ is higher than that of $Rh_2(CO)$ (0.90 vs 0.81 eV). Furthermore, H_2 does not adsorb nearly as strongly

to $Rh_1(CO)$ compared with $Rh_2(CO)$ (–0.23 vs –1.09 eV), which has been hypothesized to arise from a lack of orbital overlap between $Rh_1(CO)$ and H_2.[33] The binding of H_2 is predicted to be weak and similar for all considered Rh_1 sites (i.e., Rh_1/TiO_2, Rh_1OH/TiO_2 and Rh_1 near O_{3c}vac). Consequently, Rh_1 species cannot readily dissociate H_2, in contrast to Rh_2 dimers. This phenomenon is similar to how Pd-Pd sites strongly adsorb H_2 and accelerate dissociative H_2 adsorption on a Pd/Au alloy, unlike Pd-Au sites that bind H_2 more weakly.[102,103] These results, combined with the findings that CO adsorbs weakly and has strong C-O bond strength on Rh_1 on TiO_2, explain the increased rWGSR selectivity of Rh_1 compared with Rh nanoclusters. These observations may also provide insight for other atomically dispersed metal ions and nanoclusters supported on metal oxides (e.g., Ru/Al_2O_3,[36] Pt/CeO_2,[14] Ru/CeO_2[15]) that display a similar rWGSR vs. methanation selectivity tradeoff for thermocatalytic CO_2 reduction.

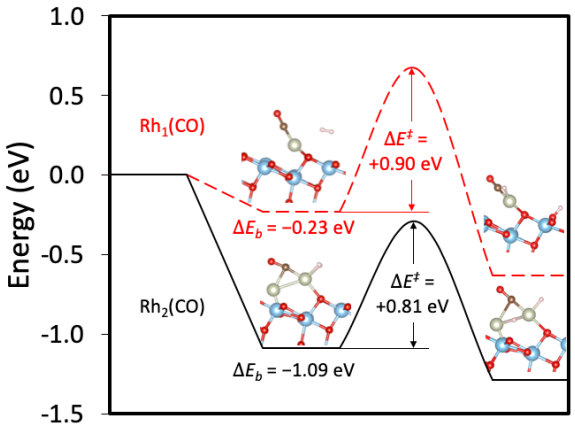

Fig. 2-11. Adsorption and dissociation of H_2 on $Rh_1(CO)$ and $Rh_2(CO)$ supported on $TiO_2(101)$. The reference state is $Rh_1(CO)/TiO_2(101)$ or $Rh_1(CO)/TiO_2(101)$. ΔE_b is the electronic binding energy of H_2 on $Rh_x(CO)$ and $\Delta E^{\ddagger}$ is the activation energy for hydrogen dissociation.

2.4 Conclusions

The selectivity of thermocatalytic CO_2 reduction to CH_4 or CO depends strongly on the size of Rh species on TiO_2 under reducing conditions. The high CO selectivity of atomically dispersed Rh_1 catalysts on anatase TiO_2 compared with their larger Rh nanocluster counterparts

has been experimentally demonstrated, but atomistic modeling of the origin of this selectivity difference has not yet been provided. Additionally, first-principles microkinetic modeling of Rh_1 active site(s) for CO_2 to CO reduction and the reaction pathway is lacking.

Here we computationally study plausible Rh_1/TiO_2 active sites and reaction mechanisms for CO_2 reduction to CO. We predict that Rh_1 on pristine $TiO_2(101)$ ($Rh_1/TiO_2(101)$), Rh_1 with a nearby hydroxyl group on TiO_2 ($Rh_1OH/TiO_2(101)$), and Rh_1 near an oxygen vacancy at a three-fold coordinated site (Rh_1 near O_{3c}vac) are likely stable Rh_1 species. The relative abundance of these species will depend on the reaction conditions.[59] Among the considered Rh_1 sites and reaction mechanisms, a Rh_1 site on $TiO_2(101)$ following CO_2 dissociation via an oxygen-vacancy assisted mechanism is predicted to be the most active toward CO production and had closest agreement compared with apparent activation barriers from literature.

Our findings reveal that CO adsorbs weakly and has strong C-O bond strength on Rh_1/TiO_2 compared with larger Rh_x (x = 2–8 atoms) nanoclusters, including Rh_2 dimers. Also, Rh_1 has a larger activation barrier than Rh_2 dimers and nanoclusters to dissociate H_2 to reduce CO to CH_4 and does not have nearby Rh-metal sites to adsorb H*. Taken together these findings rationalize the unique capability of Rh_1 species to selectively catalyze CO_2 reduction to CO compared with Rh nanoclusters.

2.5 References

(1) Qiao, B.; Wang, A.; Yang, X.; Allard, L. F.; Jiang, Z.; Cui, Y.; Liu, J.; Li, J.; Zhang, T. Single-Atom Catalysis of CO Oxidation Using Pt1/FeOx. *Nature Chem* **2011**, *3* (8), 634–641. https://doi.org/10.1038/nchem.1095.

(2) Kwon, Y.; Kim, T. Y.; Kwon, G.; Yi, J.; Lee, H. Selective Activation of Methane on Single-Atom Catalyst of Rhodium Dispersed on Zirconia for Direct Conversion. *Journal of the American Chemical Society* **2017**, *139* (48), 17694–17699. https://doi.org/10.1021/jacs.7b11010.

(3) Matsubu, J. C.; Yang, V. N.; Christopher, P. Isolated Metal Active Site Concentration and Stability Control Catalytic CO_2 Reduction Selectivity. *Journal of the American Chemical Society* **2015**, *137* (8), 3076–3084. https://doi.org/10.1021/ja5128133.

(4) Millet, M.-M.; Algara-Siller, G.; Wrabetz, S.; Mazheika, A.; Girgsdies, F.; Teschner, D.; Seitz, F.; Tarasov, A.; Levchenko, S. V.; Schlögl, R.; Frei, E. Ni Single Atom Catalysts for CO2 Activation. *J. Am. Chem. Soc.* **2019**, *141* (6), 2451–2461. https://doi.org/10.1021/jacs.8b11729.

(5) Yang, X. F.; Wang, A.; Qiao, B.; Li, J.; Liu, J.; Zhang, T. Single-Atom Catalysts: A New Frontier in Heterogeneous Catalysis. *Accounts of Chemical Research* **2013**, *46* (8), 1740–1748. https://doi.org/10.1021/ar300361m.

(6) Liu, J. Catalysis by Supported Single Metal Atoms. *ACS Catal.* **2017**, *7* (1), 34–59. https://doi.org/10.1021/acscatal.6b01534.

(7) Ammal, S. C.; Heyden, A. Water-Gas Shift Activity of Atomically Dispersed Cationic Platinum versus Metallic Platinum Clusters on Titania Supports. *ACS Catal.* **2017**, *7* (1), 301–309. https://doi.org/10.1021/acscatal.6b02764.

(8) Ammal, S. C.; Heyden, A. Understanding the Nature and Activity of Supported Platinum Catalysts for the Water–Gas Shift Reaction: From Metallic Nanoclusters to Alkali-Stabilized Single-Atom Cations. *ACS Catal.* **2019**, *9* (9), 7721–7740. https://doi.org/10.1021/acscatal.9b01560.

(9) Shan, J.; Li, M.; Allard, L. F.; Lee, S.; Flytzani-Stephanopoulos, M. Mild Oxidation of Methane to Methanol or Acetic Acid on Supported Isolated Rhodium Catalysts. *Nature* **2017**, *551* (7682), 605–608. https://doi.org/10.1038/nature24640.

(10) Wang, H.; Liu, J.-X.; Allard, L. F.; Lee, S.; Liu, J.; Li, H.; Wang, J.; Wang, J.; Oh, S. H.; Li, W.; Flytzani-Stephanopoulos, M.; Shen, M.; Goldsmith, B. R.; Yang, M. Surpassing the Single-Atom Catalytic Activity Limit through Paired Pt-O-Pt Ensemble Built from Isolated Pt1 Atoms. *Nat Commun* **2019**, *10* (1), 1–12. https://doi.org/10.1038/s41467-019-11856-9.

(11) Doherty, F.; Wang, H.; Yang, M.; R. Goldsmith, B. Nanocluster and Single-Atom Catalysts for Thermocatalytic Conversion of CO and CO_2. *Catalysis Science & Technology* **2020**. https://doi.org/10.1039/D0CY01316A.

(12) Ma, J.; Sun, N.; Zhang, X.; Zhao, N.; Xiao, F.; Wei, W.; Sun, Y. A Short Review of Catalysis for CO2 Conversion. *Catalysis Today* **2009**, *148* (3), 221–231. https://doi.org/10.1016/j.cattod.2009.08.015.

(13) Song, C. Global Challenges and Strategies for Control, Conversion and Utilization of CO_2 for Sustainable Development Involving Energy, Catalysis, Adsorption and Chemical Processing. *Catalysis Today* **2006**, *115* (1–4), 2–32. https://doi.org/10.1016/j.cattod.2006.02.029.

(14) Wang, Y.; Arandiyan, H.; Scott, J.; Aguey-Zinsou, K.-F.; Amal, R. Single Atom and Nanoclustered Pt Catalysts for Selective CO2 Reduction. *ACS Appl. Energy Mater.* **2018**, *1* (12), 6781–6789. https://doi.org/10.1021/acsaem.8b00817.
(15) Aitbekova, A.; Wu, L.; Wrasman, C. J.; Boubnov, A.; Hoffman, A. S.; Goodman, E. D.; Bare, S. R.; Cargnello, M. Low-Temperature Restructuring of CeO_2 -Supported Ru Nanoparticles Determines Selectivity in CO_2 Catalytic Reduction. *J. Am. Chem. Soc.* **2018**, *140* (42), 13736–13745. https://doi.org/10.1021/jacs.8b07615.
(16) DeRita, L.; Dai, S.; Lopez-Zepeda, K.; Pham, N.; Graham, G. W.; Pan, X.; Christopher, P. Catalyst Architecture for Stable Single Atom Dispersion Enables Site-Specific Spectroscopic and Reactivity Measurements of CO Adsorbed to Pt Atoms, Oxidized Pt Clusters, and Metallic Pt Clusters on TiO2. *J. Am. Chem. Soc.* **2017**, *139* (40), 14150–14165. https://doi.org/10.1021/jacs.7b07093.
(17) Resasco, J.; DeRita, L.; Dai, S.; Chada, J. P.; Xu, M.; Yan, X.; Finzel, J.; Hanukovich, S.; Hoffman, A. S.; Graham, G. W.; Bare, S. R.; Pan, X.; Christopher, P. Uniformity Is Key in Defining Structure–Function Relationships for Atomically Dispersed Metal Catalysts: The Case of Pt/CeO2. *J. Am. Chem. Soc.* **2020**, *142* (1), 169–184. https://doi.org/10.1021/jacs.9b09156.
(18) Hülsey, M. J.; Zhang, B.; Ma, Z.; Asakura, H.; Do, D. A.; Chen, W.; Tanaka, T.; Zhang, P.; Wu, Z.; Yan, N. In Situ Spectroscopy-Guided Engineering of Rhodium Single-Atom Catalysts for CO Oxidation. *Nat Commun* **2019**, *10* (1), 1330. https://doi.org/10.1038/s41467-019-09188-9.
(19) Wang, C.; Gu, X.-K.; Yan, H.; Lin, Y.; Li, J.; Liu, D.; Li, W.-X.; Lu, J. Water-Mediated Mars–Van Krevelen Mechanism for CO Oxidation on Ceria-Supported Single-Atom Pt1 Catalyst. *ACS Catal.* **2017**, *7* (1), 887–891. https://doi.org/10.1021/acscatal.6b02685.
(20) Yan, H.; Cheng, H.; Yi, H.; Lin, Y.; Yao, T.; Wang, C.; Li, J.; Wei, S.; Lu, J. Single-Atom Pd1/Graphene Catalyst Achieved by Atomic Layer Deposition: Remarkable Performance in Selective Hydrogenation of 1,3-Butadiene. *J. Am. Chem. Soc.* **2015**, *137* (33), 10484–10487. https://doi.org/10.1021/jacs.5b06485.
(21) Newton, M. A.; Belver-Coldeira, C.; Martínez-Arias, A.; Fernández-García, M. Dynamic in Situ Observation of Rapid Size and Shape Change of Supported Pd Nanoparticles during CO/NO Cycling. *Nat Mater* **2007**, *6* (7), 528–532. https://doi.org/10.1038/nmat1924.
(22) Dent, A. J.; Evans, J.; Fiddy, S. G.; Jyoti, B.; Newton, M. A.; Tromp, M. Rhodium Dispersion during NO/CO Conversions. *Angewandte Chemie International Edition* **2007**, *46* (28), 5356–5358. https://doi.org/10.1002/anie.200701419.
(23) Berkó, A.; Szökő, J.; Solymosi, F. Effect of CO on the Morphology of Pt Nanoparticles Supported on TiO2(110)-(1×n). *Surface Science* **2004**, *566–568*, 337–342. https://doi.org/10.1016/j.susc.2004.05.065.
(24) Solymosi, F.; Pasztor, M. An Infrared Study of the Influence of Carbon Monoxide Chemisorption on the Topology of Supported Rhodium. *J. Phys. Chem.* **1985**, *89* (22), 4789–4793. https://doi.org/10.1021/j100268a026.
(25) Mizushima, Takanori.; Tohji, Kazuyuki.; Udagawa, Yasuo.; Ueno, Akifumi. EXAFS Study of the Carbon Monoxide Adsorption-Induced Morphology Change in Ruthenium Clusters Supported on Alumina. *J. Phys. Chem.* **1990**, *94* (12), 4980–4985. https://doi.org/10.1021/j100375a041.
(26) Goldsmith, B. R.; Sanderson, E. D.; Ouyang, R.; Li, W. X. CO- and NO-Induced Disintegration and Redispersion of Three-Way Catalysts Rhodium, Palladium, and

Platinum: An Ab Initio Thermodynamics Study. *Journal of Physical Chemistry C* **2014**, *118* (18), 9588–9597. https://doi.org/10.1021/jp502201f.

(27) Ouyang, R.; Liu, J.-X.; Li, W.-X. Atomistic Theory of Ostwald Ripening and Disintegration of Supported Metal Particles under Reaction Conditions. *J. Am. Chem. Soc.* **2013**, *135* (5), 1760–1771. https://doi.org/10.1021/ja3087054.

(28) Berkó, A.; Solymosi, F. Adsorption-Induced Structural Changes of Rh Supported by TiO2(110)-(1×2): An STM Study. *Journal of Catalysis* **1999**, *183* (1), 91–101. https://doi.org/10.1006/jcat.1998.2368.

(29) Evans, J.; Hayden, B.; Mosselmans, F.; Murray, A. The Chemistry of Rhodium on TiO2(110) Deposited by MOCVD of [Rh(CO)2Cl]2 and MVD. *Surface Science* **1994**, *301* (1), 61–82. https://doi.org/10.1016/0039-6028(94)91288-2.

(30) Evans, J.; Hayden, B.; Mosselmans, F.; Murray, A. Adsorbate Induced Phase Changes of Rhodium on TiO2(110). *Surface Science Letters* **1992**, *279* (1), L159–L164. https://doi.org/10.1016/0167-2584(92)90193-9.

(31) Frank, M.; Kühnemuth, R.; Bäumer, M.; Freund, H.-J. Oxide-Supported Rh Particle Structure Probed with Carbon Monoxide. *Surface Science* **1999**, *427–428*, 288–293. https://doi.org/10.1016/S0039-6028(99)00281-2.

(32) Asokan, C.; Thang, H. V.; Pacchioni, G.; Christopher, P. Reductant Composition Influences the Coordination of Atomically Dispersed Rh on Anatase TiO2. *Catal. Sci. Technol.* **2020**, *10* (6), 1597–1601. https://doi.org/10.1039/D0CY00146E.

(33) Ma, S.; Song, W.; Liu, B.; Zheng, H.; Deng, J.; Zhong, W.; Liu, J.; Gong, X.-Q.; Zhao, Z. Elucidation of the High CO_2 Reduction Selectivity of Isolated Rh Supported on TiO_2: A DFT Study. *Catal. Sci. Technol.* **2016**, *6* (15), 6128–6136. https://doi.org/10.1039/C5CY02158H.

(34) Chernyshova, I. V.; Somasundaran, P.; Ponnurangam, S. On the Origin of the Elusive First Intermediate of CO2 Electroreduction. *PNAS* **2018**, *115* (40), E9261–E9270. https://doi.org/10.1073/pnas.1802256115.

(35) Luca, O. R.; Fenwick, A. Q. Organic Reactions for the Electrochemical and Photochemical Production of Chemical Fuels from CO2 – The Reduction Chemistry of Carboxylic Acids and Derivatives as Bent CO2 Surrogates. *Journal of Photochemistry and Photobiology B: Biology* **2015**, *152*, 26–42. https://doi.org/10.1016/j.jphotobiol.2015.04.015.

(36) Kwak, J. H.; Kovarik, L.; Szanyi, J. CO2 Reduction on Supported Ru/Al2O3 Catalysts: Cluster Size Dependence of Product Selectivity. *ACS Catal.* **2013**, *3* (11), 2449–2455. https://doi.org/10.1021/cs400381f.

(37) Lin, J.; Wang, A.; Qiao, B.; Liu, X.; Yang, X.; Wang, X.; Liang, J.; Li, J.; Liu, J.; Zhang, T. Remarkable Performance of Ir1/FeOx Single-Atom Catalyst in Water Gas Shift Reaction. *J. Am. Chem. Soc.* **2013**, *135*, 15314–15317. https://doi.org/dx.doi.org/10.1021/ja408574m.

(38) Kresse, G.; Hafner, J. Ab Initio Molecular Dynamics for Liquid Metals. *Physical Review B* **1993**, *47* (1), 558–561.

(39) Kresse, G.; Furthmüller, J. Efficiency of Ab-Initio Total Energy Calculations for Metals and Semiconductors Using a Plane-Wave Basis Set. *Computational Materials Science* **1996**, *6*, 15–50.

(40) Kresse, G.; Furthmüller, J. Efficient Iterative Schemes for Ab Initio Total-Energy Calculations Using a Plane-Wave Basis Set. *Physical Review B* **1996**, *54* (16), 11169–11186.

(41) Kresse, G.; Joubert, D. From Ultrasoft Pseudopotentials to the Projector Augmented-Wave Method. *Physical Review B* **1999**, *59* (3), 11–19.
(42) Ranade, M. R.; Navrotsky, A.; Zhang, H. Z.; Banfield, J. F.; Elder, S. H.; Zaban, A.; Borse, P. H.; Kulkarni, S. K.; Doran, G. S.; Whitfield, H. J. Energetics of Nanocrystalline TiO2. *PNAS* **2002**, *99* (suppl 2), 6476–6481. https://doi.org/10.1073/pnas.251534898.
(43) Vittadini, A.; Casarin, M.; Selloni, A. Chemistry of and on TiO2-Anatase Surfaces by DFT Calculations: A Partial Review. *Theor Chem Account* **2007**, *117* (5), 663–671. https://doi.org/10.1007/s00214-006-0191-4.
(44) Hengerer, R.; Bolliger, B.; Erbudak, M.; Grätzel, M. Structure and Stability of the Anatase TiO2 (101) and (001) Surfaces. *Surface Science* **2000**, *460* (1), 162–169. https://doi.org/10.1016/S0039-6028(00)00527-6.
(45) Larsen, A. H.; Jens, J.; Blomqvist, J. The Atomic Simulation Environment — a Python Library for Working with Atoms. *Journal of Physics: Condensed Matter* **2017**, *29*, 273002–273031.
(46) Iyengar, L.; Rao, K. V. K.; Naidu, S. V. N. Thermal Expansion of Rutile and Anatase. *Journal of the American Ceramic Society* **1969**, *53* (3), 124.
(47) Henkelman, G.; Uberuaga, B. P.; Jónsson, H. A Climbing Image Nudged Elastic Band Method for Finding Saddle Points and Minimum Energy Paths. *The Journal of Chemical Physics* **2000**, *113* (22), 9901–9904. https://doi.org/10.1063/1.1329672.
(48) Grimme, S.; Antony, J.; Ehrlich, S.; Krieg, H. A Consistent and Accurate Ab Initio Parametrization of Density Functional Dispersion Correction (DFT-D) for the 94 Elements H-Pu. *Journal of Chemical Physics* **2010**, *132* (15). https://doi.org/10.1063/1.3382344.
(49) Morgan, B. J.; Watson, G. W. A DFT+U Description of Oxygen Vacancies at the TiO_2 Rutile (110) Surface. *Surface Science* **2007**, *601* (21), 5034–5041. https://doi.org/10.1016/j.susc.2007.08.025.
(50) Hu, Z.; Metiu, H. Choice of U for DFT+U Calculations for Titanium Oxides. *Journal of Physical Chemistry C* **2011**, *115* (13), 5841–5845. https://doi.org/10.1021/jp111350u.
(51) Mina-Camilde, N.; Manzanares I., C.; Caballero, J. F. Molecular Constants of Carbon Monoxide at v = 0, 1, 2, and 3: A Vibrational Spectroscopy Experiment in Physical Chemistry. *J. Chem. Educ.* **1996**, *73* (8), 804. https://doi.org/10.1021/ed073p804.
(52) Vilhelmsen, L. B.; Hammer, B. A Genetic Algorithm for First Principles Global Structure Optimization of Supported Nano Structures. *The Journal of Chemical Physics* **2014**, *141* (4), 044711. https://doi.org/10.1063/1.4886337.
(53) Bahn, S. R.; Jacobsen, K. W. An Object-Oriented Scripting Interface to a Legacy Electronic Structure Code. *Computing in Science & Engineering* **2002**, *4* (3), 56–66.
(54) Bruix, A.; Margraf, J. T.; Andersen, M.; Reuter, K. First-Principles-Based Multiscale Modelling of Heterogeneous Catalysis. *Nat Catal* **2019**, *2* (8), 659–670. https://doi.org/10.1038/s41929-019-0298-3.
(55) Campbell, C. T. The Degree of Rate Control: A Powerful Tool for Catalysis Research. *ACS Catal.* **2017**, *7* (4), 2770–2779. https://doi.org/10.1021/acscatal.7b00115.
(56) Filot, I. A. W.; Broos, R. J. P.; van Rijn, J. P. M.; van Heugten, G. J. H. A.; van Santen, R. A.; Hensen, E. J. M. First-Principles-Based Microkinetics Simulations of Synthesis Gas Conversion on a Stepped Rhodium Surface. *ACS Catal.* **2015**, *5* (9), 5453–5467. https://doi.org/10.1021/acscatal.5b01391.

(57) Liu, J.-X.; Richards, D.; Singh, N.; Goldsmith, B. R. Activity and Selectivity Trends in Electrocatalytic Nitrate Reduction on Transition Metals. *ACS Catal.* **2019**, *9* (8), 7052–7064. https://doi.org/10.1021/acscatal.9b02179.
(58) Porosoff, M. D.; Yan, B.; Chen, J. G. Catalytic Reduction of CO 2 by H 2 for Synthesis of CO, Methanol and Hydrocarbons: Challenges and Opportunities. *Energy Environ. Sci.* **2016**, *9* (1), 62–73. https://doi.org/10.1039/C5EE02657A.
(59) Tang, Y.; Asokan, C.; Xu, M.; Graham, G. W.; Pan, X.; Christopher, P.; Li, J.; Sautet, P. Rh Single Atoms on TiO2 Dynamically Respond to Reaction Conditions by Adapting Their Site. *Nat Commun* **2019**, *10* (1), 1–10. https://doi.org/10.1038/s41467-019-12461-6.
(60) Yates, J. T.; Duncan, T. M.; Vaughan, R. W. Infrared Spectroscopic Study of Activated Surface Processes: CO Chemisorption on Supported Rh. *J. Chem. Phys.* **1979**, *71* (10), 9.
(61) Yates, J. T.; Duncan, T. M.; Worley, S. D.; Vaughan, R. W. Infrared Spectra of Chemisorbed CO on Rh. *The Journal of Chemical Physics* **1979**, *70* (3), 1219–1224. https://doi.org/10.1063/1.437603.
(62) Miessner, H.; Burkhardt, I.; Gutschick, D.; Zecchina, A.; Morterra, C.; Spoto, G. The Formation of a Well Defined Rhodium Dicarbonyl in Highly Dealuminated Rhodium-Exchanged Zeolite Y by Interaction with CO. *J. Chem. Soc., Faraday Trans. 1* **1989**, *85* (8), 2113–2126. https://doi.org/10.1039/F19898502113.
(63) Trautmann, S.; Baerns, M. Infrared Spectroscopic Studies of CO Adsorption on Rhodium Supported by SiO2, Al2O3, and TiO2. *Journal of Catalysis* **1994**, *150* (2), 335–344. https://doi.org/10.1006/jcat.1994.1352.
(64) Rasko, J.; Solymosi, F. Infrared Spectroscopic Study of the Photoinduced Activation of CO2 on TiO2 and Rh/TiO2 Catalysts. *J. Phys. Chem.* **1994**, *98* (29), 7147–7152. https://doi.org/10.1021/j100080a009.
(65) Frank, M.; Kühnemuth, R.; Bäumer, M.; Freund, H.-J. Vibrational Spectroscopy of CO Adsorbed on Supported Ultra-Small Transition Metal Particles and Single Metal Atoms. *Surface Science* **2000**, *454–456*, 968–973. https://doi.org/10.1016/S0039-6028(00)00241-7.
(66) Ji, Y.; Luo, Y. New Mechanism for Photocatalytic Reduction of CO2 on the Anatase TiO2(101) Surface: The Essential Role of Oxygen Vacancy. *J. Am. Chem. Soc.* **2016**, *138* (49), 15896–15902. https://doi.org/10.1021/jacs.6b05695.
(67) Novák, É.; Fodor, K.; Szailer, T.; Oszkó, A.; Erdöhelyi, A. CO2 Hydrogenation on Rh/TiO2 Previously Reduced at Different Temperatures. *Topics in Catalysis* **2002**, *20* (1), 107–117. https://doi.org/10.1023/A:1016359601399.
(68) Pan, X.; Yang, M.-Q.; Fu, X.; Zhang, N.; Xu, Y.-J. Defective TiO2 with Oxygen Vacancies: Synthesis, Properties and Photocatalytic Applications. *Nanoscale* **2013**, *5* (9), 3601–3614. https://doi.org/10.1039/C3NR00476G.
(69) He, Y.; Dulub, O.; Cheng, H.; Selloni, A.; Diebold, U. Evidence for the Predominance of Subsurface Defects on Reduced Anatase TiO2. *Phys. Rev. Lett.* **2009**, *102* (10), 106105. https://doi.org/10.1103/PhysRevLett.102.106105.
(70) Guan, H.; Lin, J.; Qiao, B.; Miao, S.; Wang, A.-Q.; Wang, X.; Zhang, T. Enhanced Performance of Rh1/TiO2 Catalyst without Methanation in Water-Gas Shift Reaction. *AIChE Journal* **2017**, *63* (6), 2081–2088. https://doi.org/10.1002/aic.15585.
(71) Scheiber, P.; Fidler, M.; Dulub, O.; Schmid, M.; Diebold, U.; Hou, W.; Aschauer, U.; Selloni, A. (Sub)Surface Mobility of Oxygen Vacancies at the TiO2 Anatase (101) Surface. *Phys. Rev. Lett.* **2012**, *109* (13), 136103. https://doi.org/10.1103/PhysRevLett.109.136103.

(72) Setvín, M.; Aschauer, U.; Scheiber, P.; Li, Y.-F.; Hou, W.; Schmid, M.; Selloni, A.; Diebold, U. Reaction of O2 with Subsurface Oxygen Vacancies on TiO2 Anatase (101). *Science* **2013**, *341* (6149), 988–991. https://doi.org/10.1126/science.1239879.
(73) Kattel, S.; Yan, B.; Chen, J. G.; Liu, P. CO2 Hydrogenation on Pt, Pt/SiO2 and Pt/TiO2: Importance of Synergy between Pt and Oxide Support. *Journal of Catalysis* **2016**, *343*, 115–126. https://doi.org/10.1016/j.jcat.2015.12.019.
(74) Karelovic, A.; Ruiz, P. Mechanistic Study of Low Temperature CO2 Methanation over Rh/TiO2 Catalysts. *Journal of Catalysis* **2013**, *301*, 141–153. https://doi.org/10.1016/j.jcat.2013.02.009.
(75) Zhang, Z. L.; Kladi, A.; Verykios, X. E. Effects of Carrier Doping on Kinetic Parameters of CO2 Hydrogenation on Supported Rhodium Catalysts. *Journal of Catalysis* **1994**, *148* (2), 737–747. https://doi.org/10.1006/jcat.1994.1260.
(76) Cheng, H.; Selloni, A. Surface and Subsurface Oxygen Vacancies in Anatase TiO2 and Differences with Rutile. *Phys. Rev. B* **2009**, *79* (9), 092101. https://doi.org/10.1103/PhysRevB.79.092101.
(77) Li, X.; Lin, J.; Li, L.; Huang, Y.; Pan, X.; Collins, S. E.; Ren, Y.; Su, Y.; Kang, L.; Liu, X.; Zhou, Y.; Wang, H.; Wang, A.; Qiao, B.; Wang, X.; Zhang, T. Controlling CO2 Hydrogenation Selectivity by Metal-Supported Electron Transfer. *Angewandte Chemie International Edition* **2020**, *59* (45), 19983–19989. https://doi.org/10.1002/anie.202003847.
(78) Hülsey, M. J.; Sun, G.; Sautet, P.; Yan, N. Observing Single-Atom Catalytic Sites During Reactions with Electrospray Ionization Mass Spectrometry. *Angewandte Chemie International Edition* **2021**, *60* (9), 4764–4773. https://doi.org/10.1002/anie.202011632.
(79) Zhai, H.; Alexandrova, A. N. Fluxionality of Catalytic Clusters: When It Matters and How to Address It. *ACS Catal.* **2017**, *7* (3), 1905–1911. https://doi.org/10.1021/acscatal.6b03243.
(80) Sanchez, A.; Abbet, S.; Heiz, U.; Schneider, W.-D.; Häkkinen, H.; Barnett, R. N.; Landman, U. When Gold Is Not Noble: Nanoscale Gold Catalysts. *J. Phys. Chem. A* **1999**, *103* (48), 9573–9578. https://doi.org/10.1021/jp9935992.
(81) Bell, A. T. The Impact of Nanoscience on Heterogeneous Catalysis. *Science* **2003**, *299* (5613), 1688–1691. https://doi.org/10.1126/science.1083671.
(82) Jennings, P. C.; Lysgaard, S.; Hummelshøj, J. S.; Vegge, T.; Bligaard, T. Genetic Algorithms for Computational Materials Discovery Accelerated by Machine Learning. *npj Computational Materials* **2019**, *5* (1), 46. https://doi.org/10.1038/s41524-019-0181-4.
(83) Liu, J.-X.; Su, Y.; Filot, I. A. W.; Hensen, E. J. M. A Linear Scaling Relation for CO Oxidation on CeO2-Supported Pd. *J. Am. Chem. Soc.* **2018**, *140* (13), 4580–4587. https://doi.org/10.1021/jacs.7b13624.
(84) Shang, C.; Liu, Z.-P. Stochastic Surface Walking Method for Structure Prediction and Pathway Searching. *J. Chem. Theory Comput.* **2013**, *9* (3), 1838–1845. https://doi.org/10.1021/ct301010b.
(85) Wales, D. J.; Doye, J. P. K. Global Optimization by Basin-Hopping and the Lowest Energy Structures of Lennard-Jones Clusters Containing up to 110 Atoms. *J. Phys. Chem. A* **1997**, *101* (28), 5111–5116. https://doi.org/10.1021/jp970984n.
(86) Rondina, G. G.; Da Silva, J. L. F. Revised Basin-Hopping Monte Carlo Algorithm for Structure Optimization of Clusters and Nanoparticles. *J. Chem. Inf. Model.* **2013**, *53* (9), 2282–2298. https://doi.org/10.1021/ci400224z.

(87) Sugita, Y.; Okamoto, Y. Replica-Exchange Molecular Dynamics Method for Protein Folding. *Chemical Physics Letters* **1999**, *314* (1), 141–151. https://doi.org/10.1016/S0009-2614(99)01123-9.
(88) Deaven, D. M.; Ho, K. M. Molecular Geometry Optimization with a Genetic Algorithm. *Phys. Rev. Lett.* **1995**, *75* (2), 288–291. https://doi.org/10.1103/PhysRevLett.75.288.
(89) Wexler, R. B.; Qiu, T.; Rappe, A. M. Automatic Prediction of Surface Phase Diagrams Using Ab Initio Grand Canonical Monte Carlo. *J. Phys. Chem. C* **2019**, *123* (4), 2321–2328. https://doi.org/10.1021/acs.jpcc.8b11093.
(90) Wallace, W. T.; Whetten, R. L. Carbon Monoxide Adsorption on Selected Gold Clusters: Highly Size-Dependent Activity and Saturation Compositions. *J. Phys. Chem. B* **2000**, *104* (47), 10964–10968. https://doi.org/10.1021/jp002889b.
(91) Kattel, S.; Liu, P.; Chen, J. G. Tuning Selectivity of CO $_2$ Hydrogenation Reactions at the Metal/Oxide Interface. *J. Am. Chem. Soc.* **2017**, *139* (29), 9739–9754. https://doi.org/10.1021/jacs.7b05362.
(92) Yang, C.-T.; Wood, B. C.; Bhethanabotla, V. R.; Joseph, B. CO2 Adsorption on Anatase TiO2 (101) Surfaces in the Presence of Subnanometer Ag/Pt Clusters: Implications for CO2 Photoreduction. *J. Phys. Chem. C* **2014**, *118* (45), 26236–26248. https://doi.org/10.1021/jp509219n.
(93) Ewing, C. S.; Hartmann, M. J.; Martin, K. R.; Musto, A. M.; Padinjarekutt, S. J.; Weiss, E. M.; Veser, G.; McCarthy, J. J.; Johnson, J. K.; Lambrecht, D. S. Structural and Electronic Properties of Pt13 Nanoclusters on Amorphous Silica Supports. *J. Phys. Chem. C* **2015**, *119* (5), 2503–2512. https://doi.org/10.1021/jp5105104.
(94) Beniya, A.; Higashi, S.; Ohba, N.; Jinnouchi, R.; Hirata, H.; Watanabe, Y. CO Oxidation Activity of Non-Reducible Oxide-Supported Mass-Selected Few-Atom Pt Single-Clusters. *Nature Communications* **2020**, *11* (1), 1–10. https://doi.org/10.1038/s41467-020-15850-4.
(95) Vayssilov, G. N.; Gates, B. C.; Rösch, N. Oxidation of Supported Rhodium Clusters by Support Hydroxy Groups. *Angewandte Chemie International Edition* **2003**, *42* (12), 1391–1394. https://doi.org/10.1002/anie.200390357.
(96) Jakub, Z.; Hulva, J.; Meier, M.; Bliem, R.; Kraushofer, F.; Setvin, M.; Schmid, M.; Diebold, U.; Franchini, C.; Parkinson, G. S. Local Structure and Coordination Define Adsorption in a Model Ir1/Fe3O4 Single-Atom Catalyst. *Angewandte Chemie* **2019**, *131* (39), 14099–14106. https://doi.org/10.1002/ange.201907536.
(97) Chen, X.; Su, X.; Su, H.-Y.; Liu, X.; Miao, S.; Zhao, Y.; Sun, K.; Huang, Y.; Zhang, T. Theoretical Insights and the Corresponding Construction of Supported Metal Catalysts for Highly Selective CO2 to CO Conversion. *ACS Catal.* **2017**, *7* (7), 4613–4620. https://doi.org/10.1021/acscatal.7b00903.
(98) Shaikhutdinov, Sh. K.; Meyer, R.; Naschitzki, M.; Bäumer, M.; Freund, H.-J. Size and Support Effects for CO Adsorption on Gold Model Catalysts. *Catalysis Letters* **2003**, *86* (4), 211–219. https://doi.org/10.1023/A:1022616102162.
(99) Belton, D. N.; Schmieg, S. J. Effect of Rh Particle Size on CO Desorption from Rh/Alumina Model Catalysts. *Surface Science* **1988**, *202* (1), 238–254. https://doi.org/10.1016/0039-6028(88)90071-4.
(100) Blyholder, G. Molecular Orbital View of Chemisorbed Carbon Monoxide. *J. Phys. Chem.* **1964**, *68* (10), 2772–2777. https://doi.org/10.1021/j100792a006.

(101) Heyl, D.; Rodemerck, U.; Bentrup, U. Mechanistic Study of Low-Temperature CO2 Hydrogenation over Modified Rh/Al2O3 Catalysts. *ACS Catal.* **2016**, *6* (9), 6275–6284. https://doi.org/10.1021/acscatal.6b01295.
(102) Yu, W.-Y.; Mullen, G. M.; Mullins, C. B. Hydrogen Adsorption and Absorption with Pd–Au Bimetallic Surfaces. *J. Phys. Chem. C* **2013**, *117* (38), 19535–19543. https://doi.org/10.1021/jp406736b.
(103) Lucci, F. R.; Darby, M. T.; Mattera, M. F. G.; Ivimey, C. J.; Therrien, A. J.; Michaelides, A.; Stamatakis, M.; Sykes, E. C. H. Controlling Hydrogen Activation, Spillover, and Desorption with Pd–Au Single-Atom Alloys. *J. Phys. Chem. Lett.* **2016**, *7* (3), 480–485. https://doi.org/10.1021/acs.jpclett.5b02400.

Chapter 3

Modeling Plasma-Induced Surface Charge Effects on CO_2 Activation by Supported Single-Atom Catalysts

3.1 Introduction

Low-temperature plasma (LTP) enhanced catalysis is a growing field of research that has reported a variety of synergistic effects for increased activity or selectivity compared to thermal catalysis, including operating beyond the thermochemical equilibrium limit.[1–3] LTP in direct contact with a catalyst or generated upstream from the catalyst promotes conversion of challenging reactions such as N_2 to ammonia[4] and CO_2 to fuels at lower thermal temperatures.[5] However, mechanistic knowledge of LTP-enhanced catalysis at the atomic level is lacking in many cases. Greater understanding of the LTP effect on the catalyst structure and properties as well as the role of LTP-generated species in the reaction mechanism is needed to guide catalyst design.

Atomistic modeling using quantum mechanics can give insight into LTP-enhanced catalytic phenomena.[6–8] The plasma-solid interface has many phenomena that may affect catalytic performance (e.g., radical species, ions, excited vibrational species, electric field) that atomistic modeling can help understand. Because of the complexity of treating all possible effects,[1] however, atomistic modeling studies thus far have focused on probing one or two LTP-based phenomena at a time. Modeling each LTP/catalyst interaction in isolation helps to assess their relative impact and deconvolute the LTP effects on catalysis. For example, the role of plasma-induced vibrational

excitations of N_2 to enhance ammonia synthesis has been studied by density functional theory (DFT) and microkinetic modeling.[4] Vibrational excitations were suggested to greatly enhance N_2 dissociation rates and NH_3 production. Additionally, the optimal catalyst for ammonia production under LTP conditions was different than the optimal catalyst for thermocatalytic conditions, opening new materials spaces for exploration. Vibrationally excited states of H_2 and CH_4 were explicitly modeled using molecular dynamics,[9] finding that the presence of nonequilibrium vibrational states had a greater impact on catalytic activity for terrace surfaces compared to stepped surfaces. Modeling predicted that radical impingement of plasma-generated atomic N and O species onto Pt films gave increased production of NO compared to the conventional Langmuir-Hinshelwood reaction of adsorbed molecular $*N_2$ and $*O_2$.[10] The role of surface charging has also been examined by atomistic modeling,[11,12] but is less explored compared to the effect of vibrational excitations and radical formation.

Plasma impinging onto a catalyst surface causes an accumulation of negative surface charge, which has implications for catalytic performance.[13–15] If the surface charging is sufficiently large, catalyst activity and selectivity can be modified from changing the adsorption strength of molecules (thus changing species coverages) and by increasing intrinsic kinetics by decreasing activation barriers of elementary reaction steps. The nature of the support and catalyst particle size can affect the importance of surface charging on heterogeneous catalysis. For example, DFT modeling was used to probe how plasma-induced surface charging changes the adsorption strength and activation of CO_2 on atomically dispersed metal ions (i.e., single atom catalysts) and nanoclusters on metal oxide supports. Specifically, Ti_1, Cu_1 and Ni_1 single atoms on γ-$Al_2O_3(110)$,[11] as well as Cu_5 and Ni_5 clusters supported on anatase $TiO_2(101)$,[12] were studied. Plasma-induced surface charging dramatically increased CO_2 adsorption strengths and decreased

activation barriers for *CO_2 dissociation to *CO and *O for both single atoms (SAs) and clusters in comparable magnitudes. It is important to know if these findings are general across many single atom catalysts and supports, or if they depend on the single atom/support combination.

In this chapter we computationally study a variety of single atom catalyst systems and compare charged (low temperature plasma catalysis) and uncharged (thermal catalysis) systems to elucidate trends across the periodic table with respect to surface charging and catalytic reduction of CO_2. We study SA catalysts because they typically show high selectivity toward the reverse water-gas shift reaction, $CO_2 + H_2 \rightleftharpoons CO + H_2O$, relative to nanoparticles.[16,17] We predict how the surface charging of irreducible and reducible supports from LTP can modulate the adsorption strength and activation of CO_2 and intermediates during CO_2 reduction by single atom catalysts. We study six different SAs and three different support materials to span a range of electronic properties for our catalyst and broaden the applicability of our resulting predictions. The six SA catalysts selected are Co_1, Ni_1, Cu_1, Rh_1, Pd_1, and Ag_1 because they are common catalysts and systematically vary in *d*-electronic configuration across the 3*d* and 4*d* transition metal series. The three supports studied, i.e., $CeO_2(100)$, $TiO_2(101)$, and γ-$Al_2O_3(110)$, are selected because they have different levels of reducibility and are broadly used catalyst supports. This collection of systems allows us to build a trend in CO_2 adsorption and dissociation for charged and uncharged catalysts. We also examine the extent of electron delocalization and charge distribution depending on the reducibility of different supports. We observe the effect of the extra electron charge on the energy of the CO_2 dissociation transition states relative to the intermediates by comparing the dissociation barriers for each system. Insights from these studies could be used to guide selection of single metal atom and support type for LTP-enhanced CO_2 reduction.

3.2 Computational Methods

Density functional theory (DFT) calculations were conducted using the CP2K software.[18] Catalyst models consisted of atomically dispersed single metal atoms (M_1) from Groups IX, X, and XI (i.e., Co_1, Ni_1, Cu_1, Rh_1, Pd_1, Ag_1) on three different metal oxide supports that differ in reducibility, namely, $CeO_2(100)$, anatase $TiO_2(101)$, and γ-$Al_2O_3(110)$ (from most to least reducible). These chosen facets offer stable binding locations for single atoms often cited in literature.[19–21] Supports are periodic in the *xy*-plane and were arranged as supercells approximately 10×10×15 Å. The bottom two layers of each support were fixed in the position of the bulk lattice, while the remaining layers could relax during geometry optimization. The DZVP basis sets were used for all atoms, which were optimized from molecular interactions,[22] combined with a plane wave basis set with 1200 Ry cutoff. The PBE+U functional with D3 dispersion[23] (i.e., PBE+U+D3) was used for all calculations. For CeO_2, an effective value of $U - J = 5.0$ eV for the Ce 4*f* electrons,[24,25] and for TiO_2 an effective $U - J = 2.5$ eV was used for the Ti 3*d* electrons.[26] No U correction was used for Al_2O_3 because this support does not have strongly correlated electrons. The Martyna-Tuckerman Poisson solver was used,[27] which allowed for defining periodicity in the *xy* plane while avoiding a periodic *z* boundary. This formalism avoided the unphysical self-interaction of vertically stacked slabs and counterions, which would provide unrealistic results for charged simulations.[28] Transition states for neutral systems were found using the Climbing Image Nudged Elastic Band method,[29] and for charged systems we used single point calculations starting from the same transition state geometries found for neutral systems.

Surface charge interactions were implemented similar to that of Bal *et al.*,[11] where an extra electron charge was given to the slab surface and was countered by a proton in the vacuum layer for net charge neutrality. The H^+ counterion was given a null basis set to force the extra electron

to associate with the surface rather than the H^+ itself. The net charge on H^+ was confirmed to be +1.0 e in each system by Hirshfeld charge analysis. The negative charge was allowed to distribute among the remaining atoms of the slab, and charge localization on the single metal atom was calculated using Hirshfeld charge. The electric field strength was tuned by changing the height of the proton above the surface. For uncharged systems, the vacuum layer above the support surface was ~25 Å (total cell height of 40 Å). For charged systems, the proton was placed as a counterion 25 Å above the surface, and the total vacuum space is 85 Å (total cell height of 100 Å). This modeling protocol results in a mean electric field strength of 1.58 V/Å, and an equivalent surface charge density of –0.14 C/m^2. This field strength is similar to the peak electric field observed experimentally within nanodischarges of porous catalyst materials.[30,31]

3.3 Results and Discussion

Although there have been no experimental studies exploring the effect of plasma-induced surface charging on catalyst performance, outside of the plasma catalysis field there is research into tunable surface chemistry by controlling the surface charge of the catalyst through applied voltage and electric field.[32,33] This research may have some analog to our plasma catalysis systems and may help isolate the relative effect that surface charge has outside of other plasma effects. For example, one study showed significant increases in binding energy (up to 0.62 eV) for isopropyl alcohol on amorphous alumina when inducing a positive 0.162 *e* charge per active site.[34] With negative charge instead of positive, the impact on adsorption may depend on the adsorbate characteristics and polarity but still have a strengthening effect on adsorption. There are also parallels with electrocatalytic studies that model charge on surfaces. Some studies explicitly add electrons to the system similar to our own methodology,[35,36] while others make use of grand canonical density functional theory (GC-DFT) that include a potential in the quantum mechanical

calculations which effectively induces a surface charge.[37,38] These studies differ in the use of a solvent, either as a dielectric background or with explicit solvent molecules that interact with the electronic field. The charge is also a result of an equilibrium reached with the grand canonical potential provided, while LTP is an inherently non-equilibrium state.

To our knowledge, single atom catalysis and plasma catalysis have not been studied together experimentally. This study therefore focuses primarily on the difference between systems with and without LTP-induced surface charge, rather than the activity inherent to single atoms compared to clusters or larger particles. When examining the rate enhancement by plasma catalysis for CO_2 reduction, it is important to know what role surface charging plays in that enhancement. Herein, we initially discuss our models of the atomically dispersed SA catalysts on metal oxide supports. Next, we analyze the electronic structure and charge of these SA/support systems under surface charging conditions and link these electronic properties to their CO_2 binding energy and CO_2 activation capabilities. We then discuss implications of these results on the field of LTP-enhanced catalysis.

The geometries of likely binding sites of the single atoms on the metal oxide supports are modeled using DFT. The model geometries of each M_1/support pair are shown in **Fig. 3-1**, including a schematic of the charged systems with the H^+ counterion in the vacuum above the surface (**Fig. 3-1g**). The binding locations are chosen based on a review of stable SA binding locations proposed under non-plasma conditions.[16,19,39,40] We did not investigate if the plasma-induced surface charge would change the ranking of stable sites because the focus of this work is to directly compare how the charge itself can affect the characteristics of CO_2 binding energy and reaction barriers, and therefore we aim to minimize the effects of confounding variables of different SA geometries. Single atom binding locations are held constant for each of the six

different metals to isolate the effects of different geometries within each support material. We model $M_1/CeO_2(100)$ in the hollow site between four surface O atoms, approximating a square planar geometry preferred by most metal atoms on ceria step sites (**Fig. 3-1a and 3-1d**).[19] $M_1/TiO_2(101)$ is modeled as bridged between a pair of two-coordinated O atoms, with varying levels of interaction with a three-coordinated O atom beneath depending on the metal identity (**Fig. 3-1b and 3-1e**). For $M_1/Al_2O_3(110)$, the M_1 replaced a surface three-coordinated Al atom (**Fig. 3-1c and 3-1f**), because this motif was predicted to be a preferred geometry for stable single atoms in recent studies of the γ-$Al_2O_3(110)$ system.[39,40]

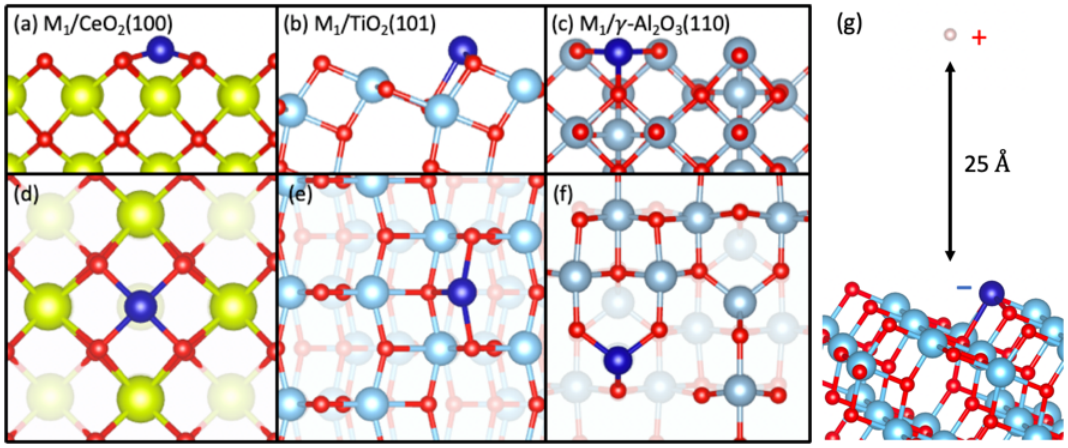

Fig. 3-1. Model systems of atomically dispersed single atom catalysts (M_1) on different supports. Side view: **(a)** $M_1/CeO_2(100)$, **(b)** $M_1/TiO_2(101)$, **(c)** M_1/γ-$Al_2O_3(110)$. Top view: **(d)** $M_1/CeO_2(100)$, **(e)** $M_1/TiO_2(101)$, **(f)** M_1/γ-$Al_2O_3(110)$. The single atom location is represented by a dark blue sphere, with the same locations chosen for all six single atoms (Co_1, Ni_1, Cu_1, Rh_1, Pd_1, Ag_1). Subsurface support atoms are shaded in the top view for clarity. (g) Schematic of the charged model system with H^+ counterion in the vacuum above the surface and a negative charge imparted to the surface (distance not to scale). Atom color legend: O = red; Ce = yellow; Ti = light blue; Al = gray blue; Single atom = dark blue; H^+ = white.

We next examine the predicted binding energy of CO_2 on each SA/support to determine the dependence of adsorption strength on charge. CO_2 adsorption is stronger on charged systems (**Fig. 3-2a**) compared to uncharged, neutral, systems (**Fig. 3-2b**). A binding energy trend emerges for the different metal species that is shared between neutral and charged systems. The binding energy is strongest for single atoms in Group IX (Co_1 and Rh_1), then decreases going across the

periodic table, that is, $Co_1 > Ni_1 > Cu_1$, and $Rh_1 > Pd_1 > Ag_1$. This binding energy trend is present for both 3*d* and 4*d* transition metals. Our predictions follow observed trends seen for CO_2 adsorption on metal surfaces, with noble metals Cu and Ag generally having weaker chemisorption strength of CO_2 compared to less noble metals like Rh.[41,42] The weak binding on Cu and Ag is present for all three supports studied. It is important to note the previous work by Bal et al. that modeled single atom Ni_1 and Cu_1 on γ-Al_2O_3(110) with and without charge.[11] Their results match well with our own trends, demonstrating a two or three-fold increase in adsorption strength of CO_2 when charge is added, as well as CO_2 adsorbing more strongly to Ni_1 than Cu_1 in both charged and neutral cases. The value of our predicted CO_2 adsorption is greater than that reported previously (2.1 eV on charged Ni_1/γ-Al_2O_3, and 1.8 eV on charged Cu_1/γ-Al_2O_3),[11] but the single atom placement in each study differs.

The trend across the three supports shows comparable binding energy between M_1/TiO_2 and M_1/Al_2O_3, whereas M_1/CeO_2 systems have much weaker CO_2 adsorption. This trend can be rationalized by the geometry of the single atom coordination environments on each support. The metal atom on ceria is more fully coordinated, surrounded by four lattice oxygens. In contrast, the SA on TiO_2 and Al_2O_3 are only coordinated with three lattice oxygens and can more readily chemisorb CO_2 with a stronger bond.

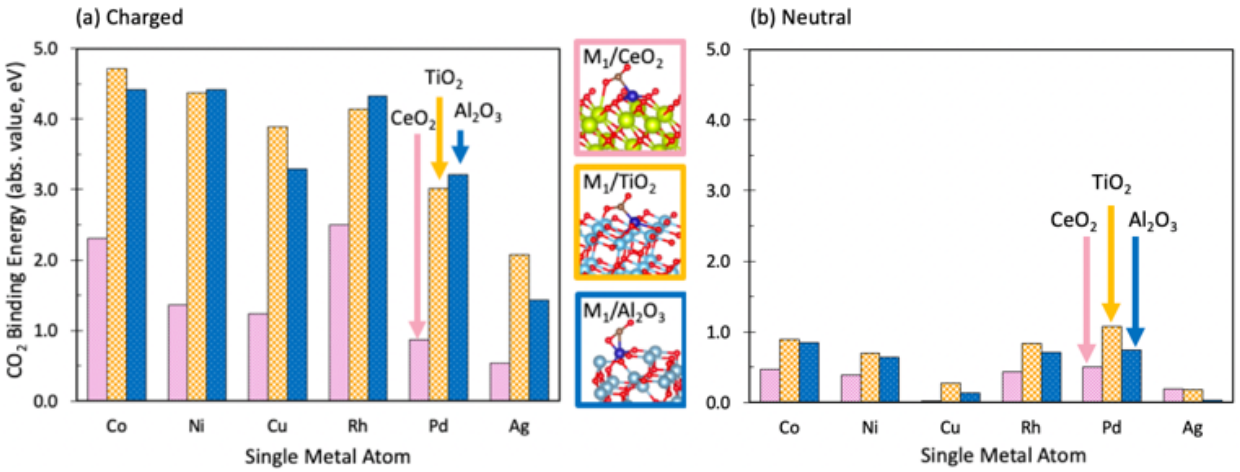

Fig. 3-2. Influence of surface charge on CO_2 binding energy on M_1/support systems. Binding energy of CO_2 on **(a)** charged and **(b)** neutral systems. Single atom = Co_1, Ni_1, Cu_1, Rh_1, Pd_1, or Ag_1; Support = $CeO_2(100)$, $TiO_2(101)$, or $Al_2O_3(110)$. Representative geometries of $*CO_2$ bound to Co_1/support are included in the center.

To better explain the reported dependence of CO_2 adsorption strength on the accumulated charge in **Fig. 3-2**, we conducted partial density of states (PDOS) and Hirshfeld charge analysis for each catalyst system. The PDOS analysis shows the energy and filling of each orbital with and without the extra charge, giving insight into why the binding energy differs so strongly based on surface charge. The Hirshfeld charge analysis assigns the calculated electron density to each atom center based on its free atom density at the corresponding distance from the atomic nucleus.[43] This analysis estimates the excess charge associated with each atom compared to its neutral state, which elucidates how much extra charge is taken on by the SA when the system is given an extra electron. Here we have performed a Hirshfeld charge analysis on each single atom system with CO_2 adsorbed.

The Hirshfeld charge on the SA catalyst depends on both the electronic structure of the single atom-adsorbate complex and the support material, shown in **Fig. 3-3a** (neutral) and **3-3b** (charged). As expected, the charge on the single atom becomes more negative when an excess electron is added, shown by the difference in Hirshfeld charge with and without the excess electron (**Fig. 3-3c**). For neutral systems, each single atom carries a negative charge naturally, ranging from

−0.4 to −1.0 *e*. With an extra electron, each adopts a further negative charge, ranging from −0.6 to −1.3 *e* in total. The Cu_1 and Ag_1 take on the least amount of charge, averaging −0.19 and −0.18 *e* respectively compared to the neutral state. This lack of additional electron localization aligns with the noble nature of bulk Cu and Ag and their fully occupied *d*-valence shells. The other SAs from Group IX and X take on more negative charge, averaging close to −0.3 *e* in net difference. There does not seem to be a clear qualitative trend based on the support type, with some SAs having little dependence on support (e.g., Ni_1) whereas others vary more strongly (e.g., Pd_1 and Ag_1). The quantitative values of these predictions are dependent on the single atom binding location and support structure, but the qualitative aspects of this analysis should be quite general.

To better understand the effect of the extra charge on CO_2 binding, we look at the PDOS of the carbon *s* and *p* orbitals in $*CO_2$ in **Fig. 3-3d**, comparing with and without charge. Energies are centered with the Fermi level set to zero. Generally, the charged systems (solid lines) all experience a downshift in energy from the neutral systems (dotted lines), due to the excess charge resulting in a higher degree of filling for higher energy orbitals. This charging has the effect of lowering the relative energy of the bonding states between the adsorbed $*CO_2$ and the single metal atom and should result in stronger adsorption of CO_2 to the SA. To support the qualitative description of the shift in orbital energy due to excess charge, we include arrows showing the change in average energy level across the depicted range from –3 eV to 5 eV. The base of the arrow is located at the average energy level for the neutral system, and the head points to the average energy level for the charged system. Average values were calculated by estimating the area under each curve with equal width rectangles (0.05 eV wide), and weighting the energy by the peak height, shown in **Eq. 3-1** below:

$$Average = \frac{\sum_{E_i=-3.0}^{E_i=5.0}(E_i * h_i)}{\sum_{E_i=-3.0}^{E_i=5.0}(h_i)} \qquad \text{(Eq. 3-1)}$$

where E_i is the energy at interval i, and h_i is the height at that energy. All arrows show the downshift in energy mentioned previously. For M_1/CeO_2, the magnitude of the shift is generally smaller than for M_1/TiO_2 and M_1/Al_2O_3. The largest shifts occur for Rh_1/TiO_2 (2.24 eV to 0.52 eV) and Ag_1/TiO_2 (3.30 eV to 0.74 eV). The magnitude of the shift in energy does not correlate directly with the amount of excess charge taken up by the single atom (**Fig. 3-2**), as Rh_1/TiO_2 shows a large degree of excess charge (–0.53 eV) while Ag_1/TiO_2 has very little (–0.10 eV).

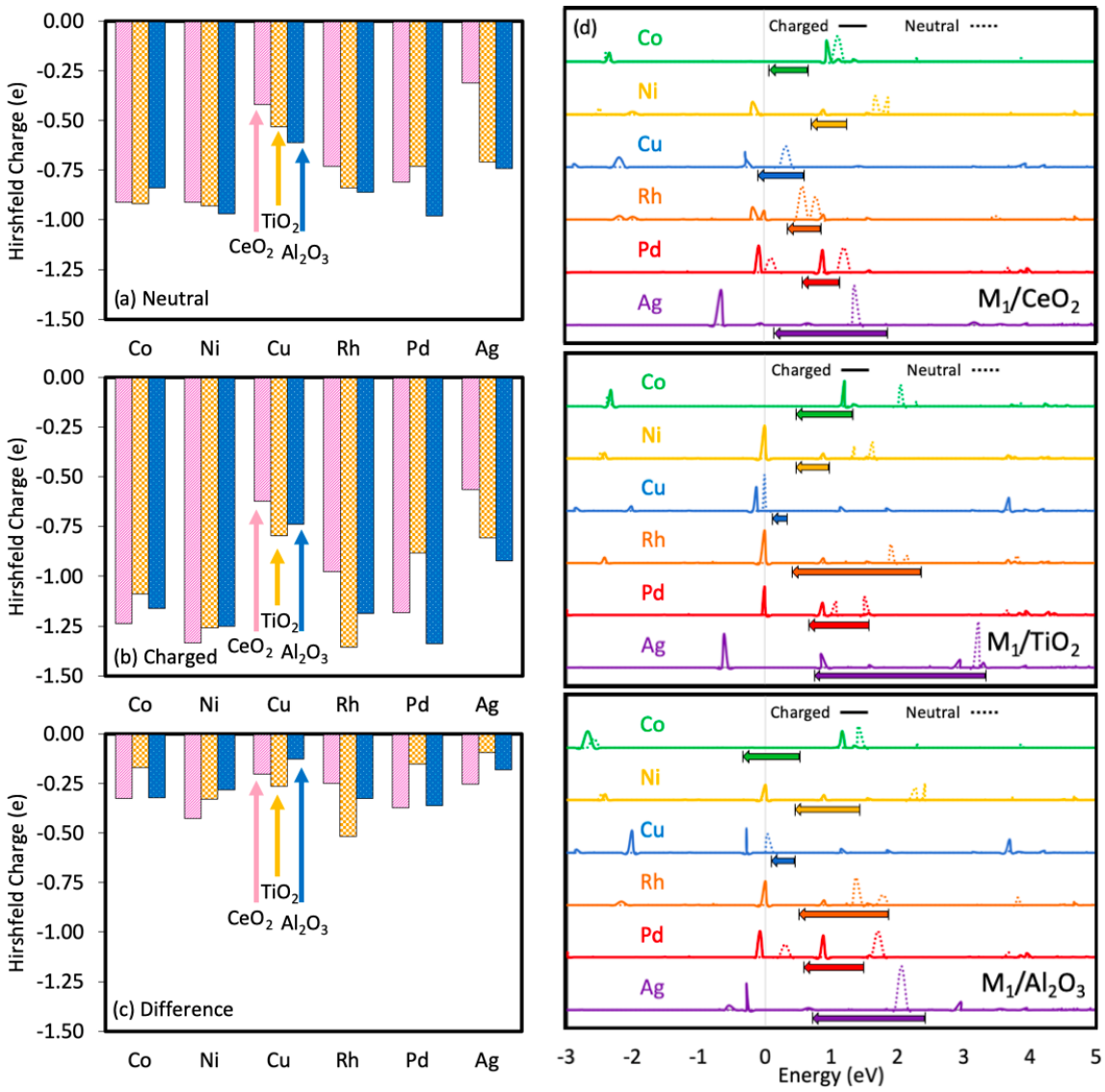

Fig. 3-3. Charge analysis and projected density of states for CO_2 adsorbed on the single atom catalyst systems. Hirshfeld charge analysis of excess charge on the single metal atom with *CO_2 bound to the single atom for **(a)** neutral and **(b)** charged systems. **(c)** The difference in Hirshfeld charge between neutral and charged systems. **(d)** *d*-projected density of states (PDOS) of *s* and *p* orbitals for the bound C atom within *CO_2, centered on the Fermi level (Fermi level energy set to zero). M_1/CeO_2 (top), M_1/TiO_2 (middle), and M_1/Al_2O_3 (bottom) are depicted separately. Dotted lines show the neutral systems, and solid lines show the charged systems. The arrow denotes the change in average energy level from neutral to charged systems calculated in the depicted range from –3 eV to 5 eV.

We next examine the effect of surface charging on the CO_2 activation barrier to dissociate to *CO and *O. The data in **Fig. 3-4** shows the CO_2 dissociation barriers for each single metal atom and support pairing for both neutral and charged systems. Most noticeably, the charged systems (**Fig. 3-4b**) all have lower CO_2 dissociation barriers than their uncharged counterparts (**Fig. 3-4a**). The difference in dissociation barriers is shown directly in **Fig. 3-4c**. In each case, the

extra electron decreases the energy of the transition states along the CO_2 splitting pathway. This effect has a greater impact on partial C-O bonds present in the transition states relative to the stable intermediates on either side, which causes the dissociation barrier itself to be lowered. Further, the barriers follow a familiar trend from left to right between Group IX, X, and XI, with the Group IX metals having the lowest barriers and the noble metals of Group XI having the highest barriers (e.g., average 49% increase from neutral Co_1 to Cu_1). This trend is present in both neutral and charged systems, although it is slightly less pronounced in the charged systems (e.g., average 38% increase from charged Co_1 to Cu_1). The CO_2 dissociation barrier trend with metal identity has an inverse correlation with the CO_2 binding energy and the Hirshfeld charge, which both followed a downward trend in absolute value from $Co_1 > Ni_1 > Cu_1$, and $Rh_1 > Pd_1 > Ag_1$ (**Fig. 3-2** and **3-3**). This finding supports the hypothesis that a more intense localized charge would cause a stronger binding energy and lower dissociation barrier. SA catalysts supported on Al_2O_3 tend to have the highest barriers, while CeO_2 and TiO_2 perform similarly to each other and swap between having the lowest or second lowest barrier depending on the metal. The added surface charge does have a larger effect on the barriers of Group XI metals Cu and Ag, seen in the difference in barriers for the neutral and charged systems (**Fig. 3-4c**).

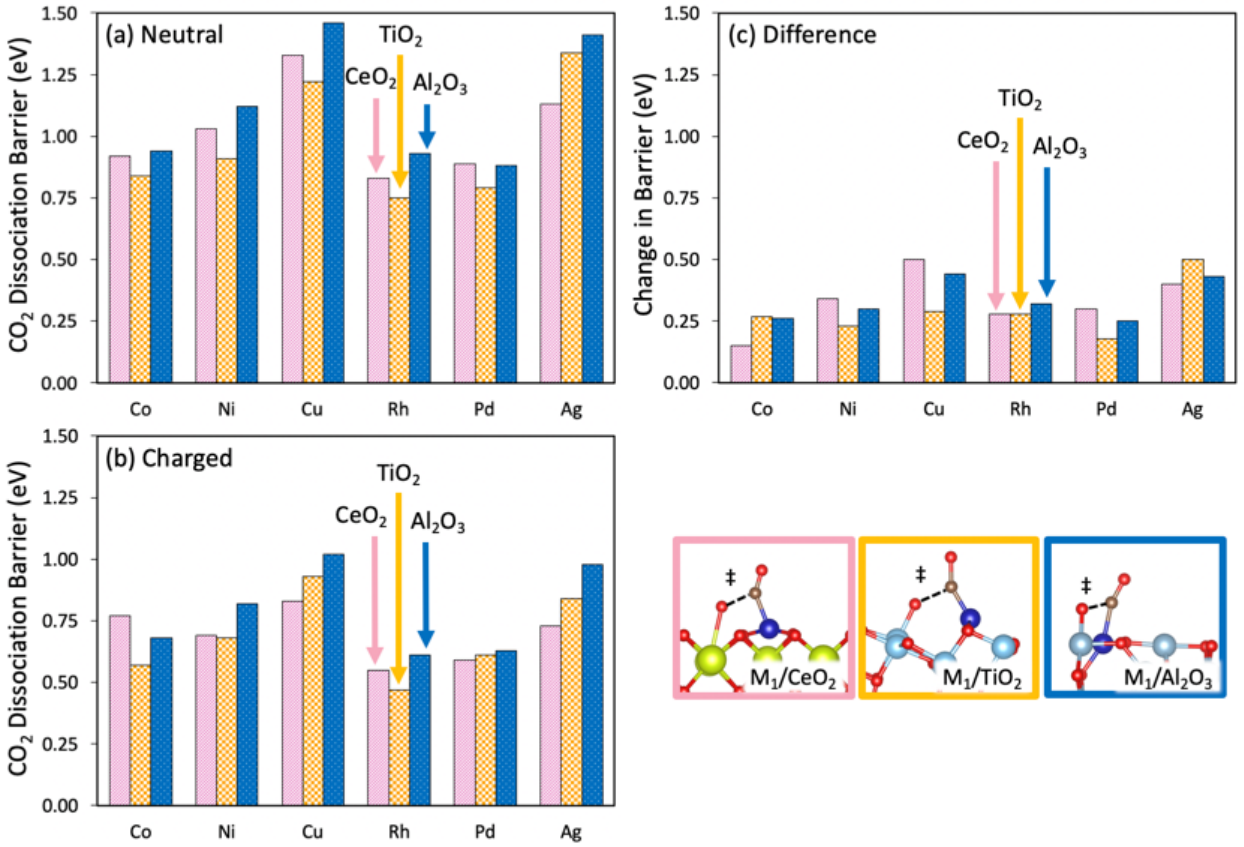

Fig. 3-4. Dissociation barrier for *CO_2 to *CO + *O for different M_1/support systems. (a) Neutral and **(b)** charged dissociation barriers shown are electronic energies. **(c)** The difference between the neutral and the charged CO_2 dissociation. Representative geometries of a CO_2 molecule dissociating on each SA/support are shown on the bottom right.

In the case of CO_2 activation, a strong CO_2 binding energy is usually beneficial for overall reaction rate, giving a chance for the *CO_2 to react on the catalyst surface before desorbing unreacted.[44] There have been connections between CO_2 adsorption strength and CO_2 dissociation barriers through linear scaling relations.[45] The ability to link CO_2 adsorption energy to CO_2 activation and catalyst geometry and electronic structure is invaluable to guide catalyst understanding and design. Here we show a correlation between adsorption energy, dissociation barrier, and excess charge on each single atom/support in **Fig. 3-5**. The correlation indicates how the effect of charge carries across each metal and support system. **Fig. 3-5a** shows the trend between charge and adsorption energy, where more negative charge accumulation correlates with stronger CO_2 adsorption energy. The trend across metals is steepest and most strongly correlated

(R^2 = 0.53) for both the M_1/TiO_2 and M_1/Al_2O_3 systems. Ceria supported metals have a smaller slope and are less correlated (R^2 = 0.38). The CO_2 dissociation barrier also follows a linear trend with Hirshfeld charge (**Fig. 3-5b**), where a more negative charge correlates with a lower barrier. M_1/Al_2O_3 carries the strongest trend (R^2 = 0.73), while M_1/CeO_2 has the weakest (R^2 = 0.45). Since both CO_2 adsorption energy and CO_2 dissociation barrier both correlate with the Hirshfeld charge, they also have a mild correlation with each other, shown in **Fig. 3-5c**. Systems with stronger CO_2 adsorption also feature a lower CO_2 dissociation barrier. The excess charge has the effect of lowering the energy of adsorbed CO_2, but it also has the same effect on the transition state along the dissociation pathway, which lowers the barrier for those systems that have strong CO_2 adsorption. All data used to generate this figure is presented in **Table 3-1**. From this analysis we confirm that the excess charge strongly affects the adsorption energy and dissociation barrier of supported SA catalysts, and that the amount of charge correlates qualitatively with each of those properties. The strength of the correlation seems to depend on the support properties, with the most reducible CeO_2 having the weakest correlation between adsorption energy, dissociation energy, and charge, and the least reducible Al_2O_3 support having the strongest correlation. However, many of these properties will depend on the single atom binding location and support facet, thus more studies are needed to draw more generalizable conclusions for these correlations.

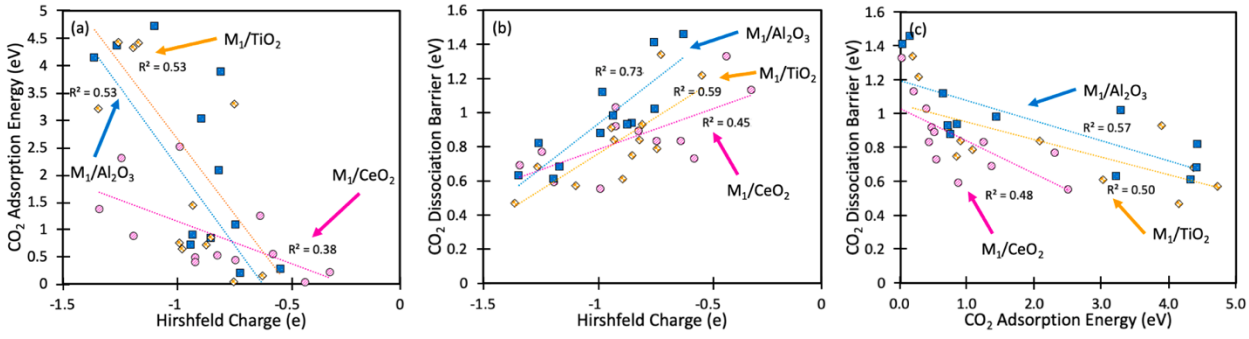

Fig. 3-5. Correlation between Hirshfeld charge, CO_2 adsorption energy, and CO_2 dissociation barrier. Data includes both charged and neutral systems. **(a)** CO_2 adsorption energy vs. Hirshfeld charge. More negative charge correlates with stronger adsorption. **(b)** CO_2 dissociation barrier vs. Hirshfeld charge. More negative charge correlates with lower barrier. **(c)** CO_2 dissociation barrier vs. CO_2 adsorption energy. Stronger adsorption correlates with lower

barrier. Trends are shown with dotted lines, and R^2 values are included next to each trendline. Key: M_1/CeO_2 = pink circles, M_1/TiO_2 = orange diamonds, M_1/Al_2O_3 = blue squares.

Table 3-1. CO_2 adsorption energies, CO_2 dissociation barriers, and Hirshfeld charges of M_1/CeO_2, M_1/TiO_2, and M_1/Al_2O_3. Energies are given as electronic energies at 0K from CP2K.

SA/Support	Charge State	CO_2 Adsorption Energy (eV)	CO_2 Dissociation Barrier(eV)	Hirshfeld Charge (e)
Co_1/CeO_2	Neutral	0.472	0.921	-0.912
Ni_1/CeO_2	Neutral	0.393	1.030	-0.914
Cu_1/CeO_2	Neutral	0.021	1.337	-0.421
Rh_1/CeO_2	Neutral	0.427	0.833	-0.737
Pd_1/CeO_2	Neutral	0.508	0.898	-0.814
Ag_1/CeO_2	Neutral	0.203	1.139	-0.317
Co_1/TiO_2	Neutral	0.898	0.842	-0.929
Ni_1/TiO_2	Neutral	0.703	0.915	-0.935
Cu_1/TiO_2	Neutral	0.271	1.221	-0.534
Rh_1/TiO_2	Neutral	0.834	0.750	-0.848
Pd_1/TiO_2	Neutral	1.074	0.795	-0.733
Ag_1/TiO_2	Neutral	0.186	1.348	-0.717
Co_1/Al_2O_3	Neutral	0.849	0.943	-0.849
Ni_1/Al_2O_3	Neutral	0.642	1.129	-0.974
Cu_1/Al_2O_3	Neutral	0.140	1.467	-0.612
Rh_1/Al_2O_3	Neutral	0.710	0.932	-0.865
Pd_1/Al_2O_3	Neutral	0.747	0.887	-0.981
Ag_1/Al_2O_3	Neutral	0.031	1.414	-0.740
Co_1/CeO_2	Charged	2.304	0.772	-1.236
Ni_1/CeO_2	Charged	1.363	0.694	-1.336
Cu_1/CeO_2	Charged	1.240	0.834	-0.621
Rh_1/CeO_2	Charged	2.548	0.558	-0.978
Pd_1/CeO_2	Charged	0.871	0.599	-1.184
Ag_1/CeO_2	Charged	0.539	0.735	-0.563
Co_1/TiO_2	Charged	4.716	0.571	-1.090
Ni_1/TiO_2	Charged	4.366	0.682	-1.258
Cu_1/TiO_2	Charged	3.886	0.930	-0.795
Rh_1/TiO_2	Charged	4.145	0.477	-1.358
Pd_1/TiO_2	Charged	3.017	0.610	-0.881
Ag_1/TiO_2	Charged	2.073	0.842	-0.805
Co_1/Al_2O_3	Charged	4.416	0.683	-1.161
Ni_1/Al_2O_3	Charged	4.421	0.825	-1.252
Cu_1/Al_2O_3	Charged	3.286	1.027	-0.737
Rh_1/Al_2O_3	Charged	4.322	0.612	-1.186
Pd_1/Al_2O_3	Charged	3.217	0.634	-1.340
Ag_1/Al_2O_3	Charged	1.431	0.987	-0.922

3.4 Conclusions

We performed density functional theory (DFT) modeling to elucidate how plasma-induced surface charging of atomically dispersed single atoms on metal oxides affects CO_2 adsorption trends and is linked to CO_2 dissociation barriers. We further connect these trends to the partial density of states and the reducibility of the support. We find that accumulated surface charge on the SA increases the CO_2 adsorption strength and decreases the CO_2 dissociation barrier for all studied SA/support combinations, consistent with prior computational studies for other single atom, nanocluster, and support combinations. The findings presented herein give better understanding of how catalyst surface charging could enable manipulation of surface coverages and intrinsic kinetics. Better understanding and control of the electron density at catalyst surfaces will enable manipulation of surface chemistry for optimal rate and selectivity to desired products.

3.5 References

(1) Bogaerts, A.; Tu, X.; Whitehead, J. C.; Centi, G.; Lefferts, L.; Guaitella, O.; Azzolina-Jury, F.; Kim, H.-H.; Murphy, A. B.; Schneider, W. F.; Nozaki, T.; Hicks, J. C.; Rousseau, A.; Thevenet, F.; Khacef, A.; Carreon, M. The 2020 Plasma Catalysis Roadmap. *J. Phys. Appl. Phys.* **2020**, *53* (44), 443001. https://doi.org/10.1088/1361-6463/ab9048.

(2) Mehta, P.; Barboun, P.; Go, D. B.; Hicks, J. C.; Schneider, W. F. Catalysis Enabled by Plasma Activation of Strong Chemical Bonds: A Review. *ACS Energy Lett.* **2019**, *4* (5), 1115–1133. https://doi.org/10.1021/acsenergylett.9b00263.

(3) Mehta, P.; Barboun, P. M.; Engelmann, Y.; Go, D. B.; Bogaerts, A.; Schneider, W. F.; Hicks, J. C. Plasma-Catalytic Ammonia Synthesis beyond the Equilibrium Limit. *ACS Catal.* **2020**, *10* (12), 6726–6734. https://doi.org/10.1021/acscatal.0c00684.

(4) Mehta, P.; Barboun, P.; Herrera, F. A.; Kim, J.; Rumbach, P.; Go, D. B.; Hicks, J. C.; Schneider, W. F. Overcoming Ammonia Synthesis Scaling Relations with Plasma-Enabled Catalysis. *Nat. Catal.* **2018**, *1* (4), 269–275. https://doi.org/10.1038/s41929-018-0045-1.

(5) Xu, S.; Chen, H.; Hardacre, C.; Fan, X. Non-Thermal Plasma Catalysis for CO2 Conversion and Catalyst Design for the Process. *J. Phys. Appl. Phys.* **2021**, *54* (23), 233001. https://doi.org/10.1088/1361-6463/abe9e1.

(6) Neyts, E. C. Atomistic Simulations of Plasma Catalytic Processes. *Front. Chem. Sci. Eng.* **2018**, *12* (1), 145–154. https://doi.org/10.1007/s11705-017-1674-7.

(7) Engelmann, Y.; van 't Veer, K.; Gorbanev, Y.; Neyts, E. C.; Schneider, W. F.; Bogaerts, A. Plasma Catalysis for Ammonia Synthesis: A Microkinetic Modeling Study on the Contributions of Eley–Rideal Reactions. *ACS Sustain. Chem. Eng.* **2021**, *9* (39), 13151–13163. https://doi.org/10.1021/acssuschemeng.1c02713.

(8) Bal, K. M.; Bogaerts, A.; Neyts, E. C. Ensemble-Based Molecular Simulation of Chemical Reactions under Vibrational Nonequilibrium. *J. Phys. Chem. Lett.* **2020**, *11* (2), 401–406. https://doi.org/10.1021/acs.jpclett.9b03356.

(9) Bal, K. M.; Neyts, E. C. Quantifying the Impact of Vibrational Nonequilibrium in Plasma Catalysis: Insights from a Molecular Dynamics Model of Dissociative Chemisorption. *J. Phys. Appl. Phys.* **2021**, *54* (39), 394004. https://doi.org/10.1088/1361-6463/ac113a.

(10) Ma, H.; Sharma, R. K.; Welzel, S.; van de Sanden, M. C. M.; Tsampas, M. N.; Schneider, W. F. Observation and Rationalization of Nitrogen Oxidation Enabled Only by Coupled Plasma and Catalyst. *Nat. Commun.* **2022**, *13* (1), 402. https://doi.org/10.1038/s41467-021-27912-2.

(11) Bal, K. M.; Huygh, S.; Bogaerts, A.; Neyts, E. C. Effect of Plasma-Induced Surface Charging on Catalytic Processes: Application to CO_2 Activation. *Plasma Sources Sci. Technol.* **2018**, *27* (2), 024001. https://doi.org/10.1088/1361-6595/aaa868.

(12) Jafarzadeh, A.; Bal, K. M.; Bogaerts, A.; Neyts, E. C. CO2 Activation on TiO2-Supported Cu5 and Ni5 Nanoclusters: Effect of Plasma-Induced Surface Charging. *J. Phys. Chem. C* **2019**, *123* (11), 6516–6525. https://doi.org/10.1021/acs.jpcc.8b11816.

(13) Neyts, E. C. Plasma-Surface Interactions in Plasma Catalysis. *Plasma Chem. Plasma Process.* **2016**, *36* (1), 185–212. https://doi.org/10.1007/s11090-015-9662-5.

(14) Neyts, E. C.; Ostrikov, K. (Ken); Sunkara, M. K.; Bogaerts, A. Plasma Catalysis: Synergistic Effects at the Nanoscale. *Chem. Rev.* **2015**, *115* (24), 13408–13446. https://doi.org/10.1021/acs.chemrev.5b00362.

(15) Neyts, E. C.; Bogaerts, A. Understanding Plasma Catalysis through Modelling and Simulation—a Review. *J. Phys. Appl. Phys.* **2014**, *47* (22), 224010. https://doi.org/10.1088/0022-3727/47/22/224010.
(16) Doherty, F.; Goldsmith, B. R. Rhodium Single-Atom Catalysts on Titania for Reverse Water Gas Shift Reaction Explored by First Principles Mechanistic Analysis and Compared to Nanoclusters. *ChemCatChem* **2021**, *13* (n/a). https://doi.org/10.1002/cctc.202100292.
(17) Doherty, F.; Wang, H.; Yang, M.; Goldsmith, B. R. Nanocluster and Single-Atom Catalysts for Thermocatalytic Conversion of CO and CO2. *Catal. Sci. Technol.* **2020**, *10* (17), 5772–5791. https://doi.org/10.1039/D0CY01316A.
(18) Hutter, J.; Iannuzzi, M.; Schiffmann, F.; VandeVondele, J. Cp2k: Atomistic Simulations of Condensed Matter Systems. *WIREs Comput. Mol. Sci.* **2014**, *4* (1), 15–25. https://doi.org/10.1002/wcms.1159.
(19) Figueroba, A.; Kovács, G.; Bruix, A.; Neyman, K. M. Towards Stable Single-Atom Catalysts: Strong Binding of Atomically Dispersed Transition Metals on the Surface of Nanostructured Ceria. *Catal. Sci. Technol.* **2016**, *6* (18), 6806–6813. https://doi.org/10.1039/C6CY00294C.
(20) Hengerer, R.; Bolliger, B.; Erbudak, M.; Grätzel, M. Structure and Stability of the Anatase TiO2 (101) and (001) Surfaces. *Surf. Sci.* **2000**, *460* (1), 162–169. https://doi.org/10.1016/S0039-6028(00)00527-6.
(21) Fernández Sanz, J.; Rabaâ, H.; Poveda, F. M.; Márquez, A. M.; Calzado, C. J. Theoretical Models for γ-Al2O3 (110) Surface Hydroxylation: An Ab Initio Embedded Cluster Study. *Int. J. Quantum Chem.* **1998**, *70* (2), 359–365. https://doi.org/10.1002/(SICI)1097-461X(1998)70:2<359::AID-QUA12>3.0.CO;2-7.
(22) VandeVondele, J.; Hutter, J. Gaussian Basis Sets for Accurate Calculations on Molecular Systems in Gas and Condensed Phases. *J. Chem. Phys.* **2007**, *127* (11), 114105. https://doi.org/10.1063/1.2770708.
(23) Smith, D. G. A.; Burns, L. A.; Patkowski, K.; Sherrill, C. D. Revised Damping Parameters for the D3 Dispersion Correction to Density Functional Theory. *J. Phys. Chem. Lett.* **2016**, *7* (12), 2197–2203. https://doi.org/10.1021/acs.jpclett.6b00780.
(24) Lin, F.; Wang, Q.; Huang, X.; Jin, J. Investigation of Chlorine-Poisoning Mechanism of MnO /TiO2 and MnO -CeO2/TiO2 Catalysts during o-DCBz Catalytic Decomposition: Experiment and First-Principles Calculation. *J. Environ. Manage.* **2021**, *298*, 113454. https://doi.org/10.1016/j.jenvman.2021.113454.
(25) Jiang, Y.; Adams, J. B.; van Schilfgaarde, M. Density-Functional Calculation of CeO2 Surfaces and Prediction of Effects of Oxygen Partial Pressure and Temperature on Stabilities. *J. Chem. Phys.* **2005**, *123* (6), 064701. https://doi.org/10.1063/1.1949189.
(26) Hu, Z.; Metiu, H. Choice of U for DFT+U Calculations for Titanium Oxides. *J. Phys. Chem. C* **2011**, *115* (13), 5841–5845. https://doi.org/10.1021/jp111350u.
(27) Martyna, G. J.; Tuckerman, M. E. A Reciprocal Space Based Method for Treating Long Range Interactions in Ab Initio and Force-Field-Based Calculations in Clusters. *J. Chem. Phys.* **1999**, *110* (6), 2810. https://doi.org/10.1063/1.477923.
(28) Bal, K. M.; Neyts, E. C. Modelling Molecular Adsorption on Charged or Polarized Surfaces: A Critical Flaw in Common Approaches. *Phys. Chem. Chem. Phys.* **2018**, *20* (13), 8456–8459. https://doi.org/10.1039/C7CP08209F.

(29) Henkelman, G.; Uberuaga, B. P.; Jónsson, H. A Climbing Image Nudged Elastic Band Method for Finding Saddle Points and Minimum Energy Paths. *J. Chem. Phys.* **2000**, *113* (22), 9901–9904. https://doi.org/10.1063/1.1329672.
(30) Hensel, K.; Martišovitš, V.; Machala, Z.; Janda, M.; Leštinský, M.; Tardiveau, P.; Mizuno, A. Electrical and Optical Properties of AC Microdischarges in Porous Ceramics. *Plasma Process. Polym.* **2007**, *4* (7–8), 682–693. https://doi.org/10.1002/ppap.200700022.
(31) Hensel, K. Microdischarges in Ceramic Foams and Honeycombs. *Eur. Phys. J. D* **2009**, *54* (2), 141–148. https://doi.org/10.1140/epjd/e2009-00073-1.
(32) Che, F.; Gray, J. T.; Ha, S.; Kruse, N.; Scott, S. L.; McEwen, J.-S. Elucidating the Roles of Electric Fields in Catalysis: A Perspective. *ACS Catal.* **2018**, *8* (6), 5153–5174. https://doi.org/10.1021/acscatal.7b02899.
(33) Léonard, N. G.; Dhaoui, R.; Chantarojsiri, T.; Yang, J. Y. Electric Fields in Catalysis: From Enzymes to Molecular Catalysts. *ACS Catal.* **2021**, *11* (17), 10923–10932. https://doi.org/10.1021/acscatal.1c02084.
(34) Onn, T. M.; Gathmann, S. R.; Wang, Y.; Patel, R.; Guo, S.; Chen, H.; Soeherman, J. K.; Christopher, P.; Rojas, G.; Mkhoyan, K. A.; Neurock, M.; Abdelrahman, O. A.; Frisbie, C. D.; Dauenhauer, P. J. Alumina Graphene Catalytic Condenser for Programmable Solid Acids. *JACS Au* **2022**, *2* (5), 1123–1133. https://doi.org/10.1021/jacsau.2c00114.
(35) Varley, J. B.; Hansen, H. A.; Ammitzbøll, N. L.; Grabow, L. C.; Peterson, A. A.; Rossmeisl, J.; Nørskov, J. K. Ni–Fe–S Cubanes in CO2 Reduction Electrocatalysis: A DFT Study. *ACS Catal.* **2013**, *3* (11), 2640–2643. https://doi.org/10.1021/cs4005419.
(36) Duan, Z.; Henkelman, G. Surface Charge and Electrostatic Spin Crossover Effects in CoN4 Electrocatalysts. *ACS Catal.* **2020**, *10* (20), 12148–12155. https://doi.org/10.1021/acscatal.0c02458.
(37) Abidi, N.; Lim, K. R. G.; Seh, Z. W.; Steinmann, S. N. Atomistic Modeling of Electrocatalysis: Are We There Yet? *WIREs Comput. Mol. Sci.* **2021**, *11* (3), e1499. https://doi.org/10.1002/wcms.1499.
(38) Alsunni, Y. A.; Alherz, A. W.; Musgrave, C. B. Electrocatalytic Reduction of CO2 to CO over Ag(110) and Cu(211) Modeled by Grand-Canonical Density Functional Theory. *J. Phys. Chem. C* **2021**, *125* (43), 23773–23783. https://doi.org/10.1021/acs.jpcc.1c07484.
(39) Gao, H. Theoretical Analysis of CO+NO Reaction Mechanism on the Single Pd Atom Embedded in γ-Al2O3 (110) Surface. *Appl. Catal. Gen.* **2017**, *529*, 156–166. https://doi.org/10.1016/j.apcata.2016.11.007.
(40) Li, H.; Shi, L.; Jin, C.; Ye, R.; Zhang, R. Co and Ni Incorporated γ-Al2O3 (110) Surface: A Density Functional Theory Study. *Catalysts* **2022**, *12* (2), 111. https://doi.org/10.3390/catal12020111.
(41) Hammer, B.; Norskov, J. K. Why Gold Is the Noblest of All the Metals. *Nature* **1995**, *376* (6537), 238–240. https://doi.org/10.1038/376238a0.
(42) Kepp, K. P. Chemical Causes of Metal Nobleness. *ChemPhysChem* **2020**, *21* (5), 360–369. https://doi.org/10.1002/cphc.202000013.
(43) Hirshfeld, F. L. Bonded-Atom Fragments for Describing Molecular Charge Densities. *Theor. Chim. Acta* **1977**, *44* (2), 129–138. https://doi.org/10.1007/BF00549096.
(44) Li, Y.; Hwa Chan, S.; Sun, Q. Heterogeneous Catalytic Conversion of CO 2 : A Comprehensive Theoretical Review. *Nanoscale* **2015**, *7* (19), 8663–8683. https://doi.org/10.1039/C5NR00092K.

(45) Rendón-Calle, A.; Builes, S.; Calle-Vallejo, F. A Brief Review of the Computational Modeling of CO2 Electroreduction on Cu Electrodes. *Curr. Opin. Electrochem.* **2018**, *9*, 158–165. https://doi.org/10.1016/j.coelec.2018.03.012.

Chapter 4

Electrocatalytic CO_2 Conversion via Molecular Catalyst Cobalt Phthalocyanine

4.1 Introduction

The electrochemical reduction of CO_2 into value added chemicals has been a significant area of interest for researchers for the past several decades.[1] When CO_2 is converted to energy-rich fuels such as methanol, this reaction can act as a way to store energy from sources of renewable energy that only generate intermittently, such as solar or wind power. Alternatively, CO_2 can be used to form chemical feedstocks for other reactions or further processing. CO_2 conversion by electrocatalysis is especially promising because it can be driven by carbon neutral energy sources, thus making the overall process net CO_2 negative and offering a strategy to lower atmospheric levels of CO_2 if captured from ambient air.

Electrochemical reduction of CO_2 to other value-added products requires advances in catalyst research to improve activity and selectivity. As the resulting product of the highly exothermic combustion reaction, CO_2 is very stable and any conversion away from CO_2 requires climbing a large thermodynamic hill. CO_2 can be converted to a large variety of products including formic acid (HCOOH), carbon monoxide (CO), methane (CH_4), methanol (CH_3OH), and ethylene (C_2H_4), depicted in **Fig. 4-1**. To decrease electricity costs and avoid unwanted product yield and costly separation processes after the reaction, a selective catalyst is highly desirable. In all these cases, the competing hydrogen evolution reaction (HER) must also be avoided, as it occurs at

potentials close to that of the CO_2 reduction reaction (CO_2RR) (e.g., CO_2 (g) + $6H^+ + 6e^- \rightarrow$ CH_3OH (l) + H_2O (l); E^0 = 0.016 V vs. RHE).[2] Given the numerous possible products and the thermodynamic penalty of converting CO_2 to higher energy products, it is a leading challenge in the area of CO_2 electrocatalysis to develop catalysts with high activity and selectivity toward specific products. Other major challenges to enable CO_2RR at industrial scales include the design and development of gas diffusion electrodes and membranes tailored for the CO_2RR (e.g., for use in membrane-electrode assemblies), but these topics are beyond the scope of this chapter and we point the reader to pertinent references.[3,4]

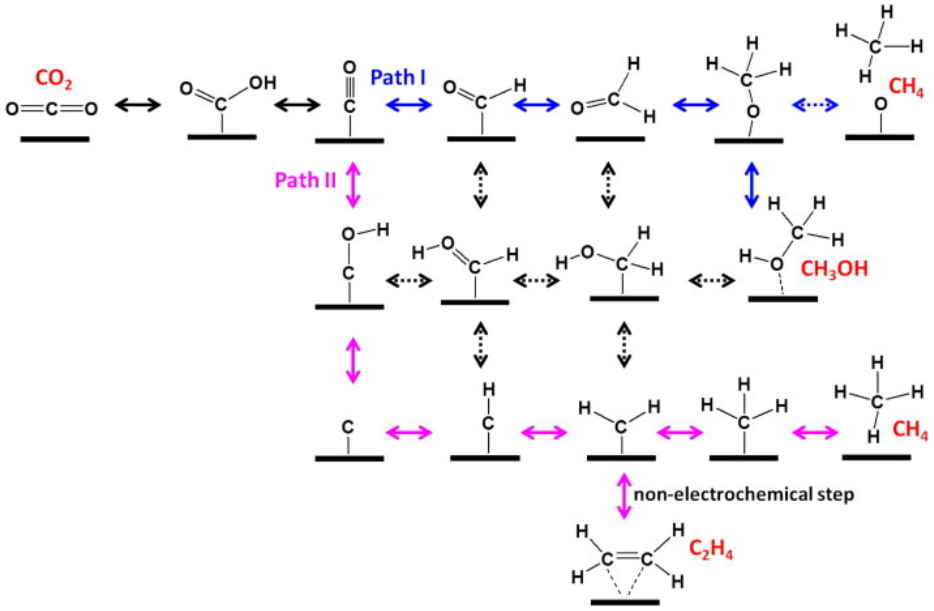

Fig. 4-1. Branching mechanism of CO_2 reduction to CH_4, CH_3OH, or C_2H_4. Other reactions are also possible, as well as desorption of CO at the start of the branching path. Adapted from ref. 5.

Electrocatalysts can take on a variety of forms, including both homogeneous and heterogeneous catalysts. Homogeneous catalysts exist in the same phase as the reactants and products, usually the gas or aqueous phase. Soluble organometallic complexes are often good candidates for homogeneous catalysis, such as the manganese polypyridyl complex $[Mn^I(bpy(COOH)_2)(CO)_3Br]$,[6] or the molecular cobalt(II) catalyst $[Co^{II}(qpy)(H_2O)]^{2+}$,[7] both capable of catalyzing CO_2 to CO. In homogeneous electrocatalysis, the catalyst molecule engages

in an electron transfer with the inert electrode, then transfers an electron with the reactant species, performing the redox chemistry (**Fig. 4-2a**). Heterogeneous catalysts make up a separate phase from the reactants and products, usually a solid catalyst in a liquid or gas reactant phase. In heterogeneous electrocatalysis, the electrode itself can act as the catalyst surface (**Fig. 4-2c**), or organometallic complexes can be affixed to the electrode to act as the active site (**Fig. 4-2b**).[8] Electron transfer for the redox reaction takes place directly between the electrode (and any affixed complexes) and the adsorbed reactants. A depiction of a typical electrocatalyst cell for CO_2 reduction is included in **Fig. 4-2d**.

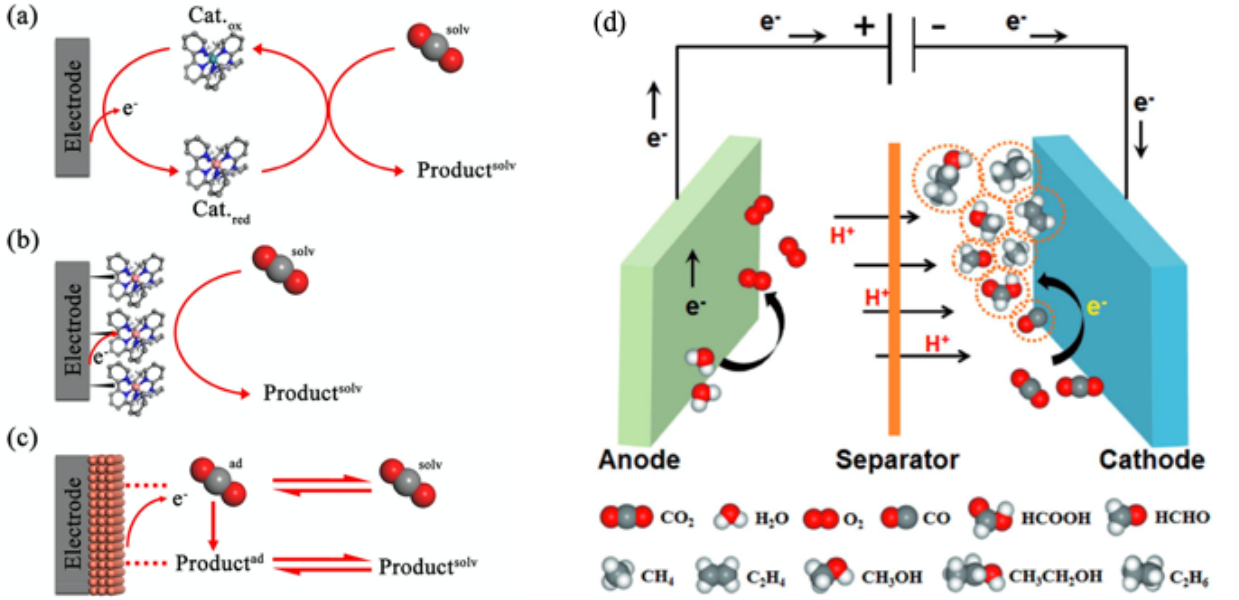

Fig. 4-2. Schemes for CO_2 reduction by different catalytic mechanisms: (a) homogeneous, (b) immobilized, and (c) heterogeneous. Adapted from ref. 8. (d) A typical electrochemical cell includes two half reactions that occur at the cathode and anode, separated by a membrane and immersed in aqueous electrolyte. Electricity is delivered to drive the reaction forward. Adapted from ref. 1.

The strategy of affixing metal-organic molecular complexes onto the electrode surface (**Fig. 4-2b**) offers several distinct advantages compared to aqueous homogeneous catalysts or solid metal heterogeneous catalysts.[9,10] This strategy maintains the highly specific and tunable coordination environment of the homogeneous organometallic complexes while allowing for

easier product separation and scale-up available with heterogeneous catalysis.[11] The active site can be very specifically chosen and designed, and it uses a much smaller total amount of active metal compared to a solid metal electrode or metal coating. Most transition metal complexes used for CO_2RR are only capable of producing CO,[12,13] but recent studies of cobalt complexes, including cobalt phthalocyanine (CoPc) have demonstrated direct reduction of CO_2 to methanol.[14–16] The mechanisms for CO_2 to CH_3OH on CoPc are still a topic of debate for the research community, but this promising reaction offers a way to efficiently convert CO_2 to a liquid fuel and feedstock in a single reaction. In this chapter, we present a review of current research on CoPc used for the CO_2RR and our own calculation and analysis of ligand-modified CoPc catalysts and their interactions with CO_2 and its reduction intermediates.

4.2 Background

Cobalt phthalocyanine (CoPc) is a metal-organic molecule with chemical formula $C_{32}H_{16}CoN_8$ that is useful in a variety of applications, from photovoltaics,[17] to light-emitting diodes,[18] to catalysis.[19] It is one of a class of phthalocyanine-based catalysts that has shown promise in the area of electrochemistry. Phthalocyanine-based catalysts have been investigated for a range of catalytic applications, such as oxidation of sulfur compounds,[20] toluene,[21] cyclohexane,[22] and reduction of CO_2.[23] A range of transition metals can be used as the central atom within the phthalocyanine (Pc). One study chose to directly determine the impact of the choice of central metal atom on the CO_2 reduction reaction.[24] In their experimental study, they chose five metals (Fe, Co, Ni, Cu, Zn) from the first row of transition metals and synthesized metal-Pc catalysts from each. Cobalt was the clear standout, with CoPc achieving the highest faradaic efficiency for CO_2 to CO (95%), followed by NiPc (72%), FePc (28%), CuPc (8.5%), and ZnPc (0.8%). CoPc also showed stability over time, maintaining a faradaic efficiency between 92-95% over 12 hours of CO_2 electrolysis.

CoPc was first recognized as a catalyst for CO_2RR to CO in 1984 by Kapusta et al.[25] and Lieber et al.[26] At this initial stage of investigation, CO was the only appreciable product observed. As research into CoPc continued, different methods of modifying the CoPc catalyst were explored that improved the efficiency and selectivity of the reaction. In one example, researchers coated a graphite electrode with a poly(4-vinylpyridine) (P4VP) membrane containing CoPc.[27] The observed production of CO was six times greater than the H_2 produced by the competing HER. The favorable selectivity was attributed to the coordination effects between the CoPc and P4VP polymers, where protonated P4VP would assist in the reduction reaction occurring on nearby CoPc.

The CoPc complex can also be modified by attaching additional functional groups or carbon complexes to the outer rings of CoPc. A 2019 study investigated cobalt(II) octaalkoxy-phthalocyanine (labeled CoPc-A) compared to CoPc and demonstrated increased catalytic performance.[28] **Fig. 4-3a** shows the structure for CoPc, and **Fig. 4-3b** shows CoPc-A. The added groups on CoPc-A caused additional steric interference that kept them from aggregating as much as CoPc (**Fig. 4-3c**), which resulted in increased catalytic performance. Both the current density (**Fig. 4-3d**) and the CO production rate (**Fig. 4-3e**) had improvement for CoPc-A over CoPc. The reduced aggregation allowed for more efficient reduction of CoPc at lower overpotentials (lower driving force), which in turn allowed for efficient reduction of CO_2.

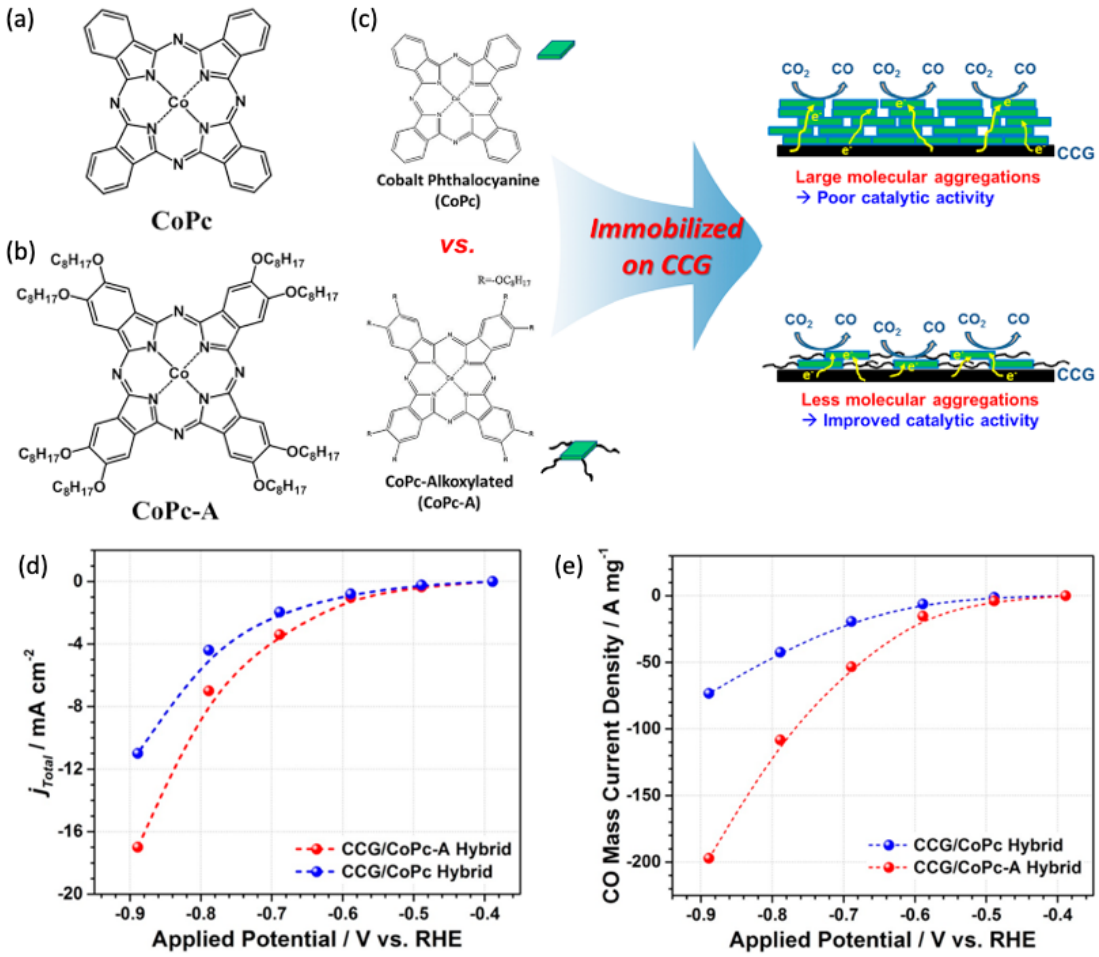

Fig. 4-3. CoPc and CoPc-A compared for CO_2RR to CO. (a) Cobalt phthalocyanine (CoPc); (b) cobalt(II) octaalkoxyphthalocyanine (CoPc-A); (c) CoPc and CoPc-A are deposited onto chemically converted graphene (CCG). The CoPc is more tightly packed and undergoes a higher degree of aggregation compared to CoPc-A. (d) The current density j_{Total} is larger (more negative) for CoPc-A. (e) The corresponding CO production, measured as CO mass current density, is also increased for CoPc-A compared to CoPc. Figure adapted from ref. 28.

Research into CoPc accelerated greatly with the demonstration of grafted CoPc to catalyze CO_2 to CH_3OH in a single cascading reaction. Wu et al. presented their findings of a methanol product with 44% faradaic efficiency by fixing CoPc to carbon nanotubes (CNTs).[14] A high level of CoPc dispersion was necessary to achieve selectivity toward methanol, further suggesting that CoPc aggregation must be limited to achieve a selective reaction toward methanol. The catalytic activity was shown to decrease over time due to the Pc itself being reduced and degraded. This catalyst degradation was minimized by appending electron-donating amino ligands to the Pc ring,

which kept the catalyst intact over the course of the reaction. This finding demonstrates the importance of catalyst engineering and the flexibility of the CoPc catalyst itself.

The effects of CoPc aggregation have also been studied using density functional theory (DFT). A study by Chen et al. compared the reactivity of a CoPc monomer and a CoPc stacked dimer as models for dispersed and aggregated CoPc, respectively.[29] The results of their study showed that only the monomer species allowed for the reaction of CO to CH_3OH, whereas the dimer system was only capable of CO desorption. The proposed mechanism for the CoPc monomer (**Fig. 4-4a**) starts with CoPc-CO^- and proceeds with a second reduction to CoPc-CO^{2-} followed by protonation to CoPc-CHO^-, after which further reaction to CH_3OH can occur. The dimer, however, does not offer a preferred path for protonation after double reduction (**Fig. 4-4b**). This finding is rationalized by observing that doubly reduced CoPc dimer is similar to two singly reduced CoPc monomers, and the reduction of the dimer past 2– requires too negative a potential. Therefore, the dimerization of CoPc effectively prevents the further reduction of CO to CH_3OH. This computational study also predicts that reduction to $CoPc^{2-}$ is required as part of the reaction path to CH_3OH, but this is still a topic of active discussion and investigation among researchers.

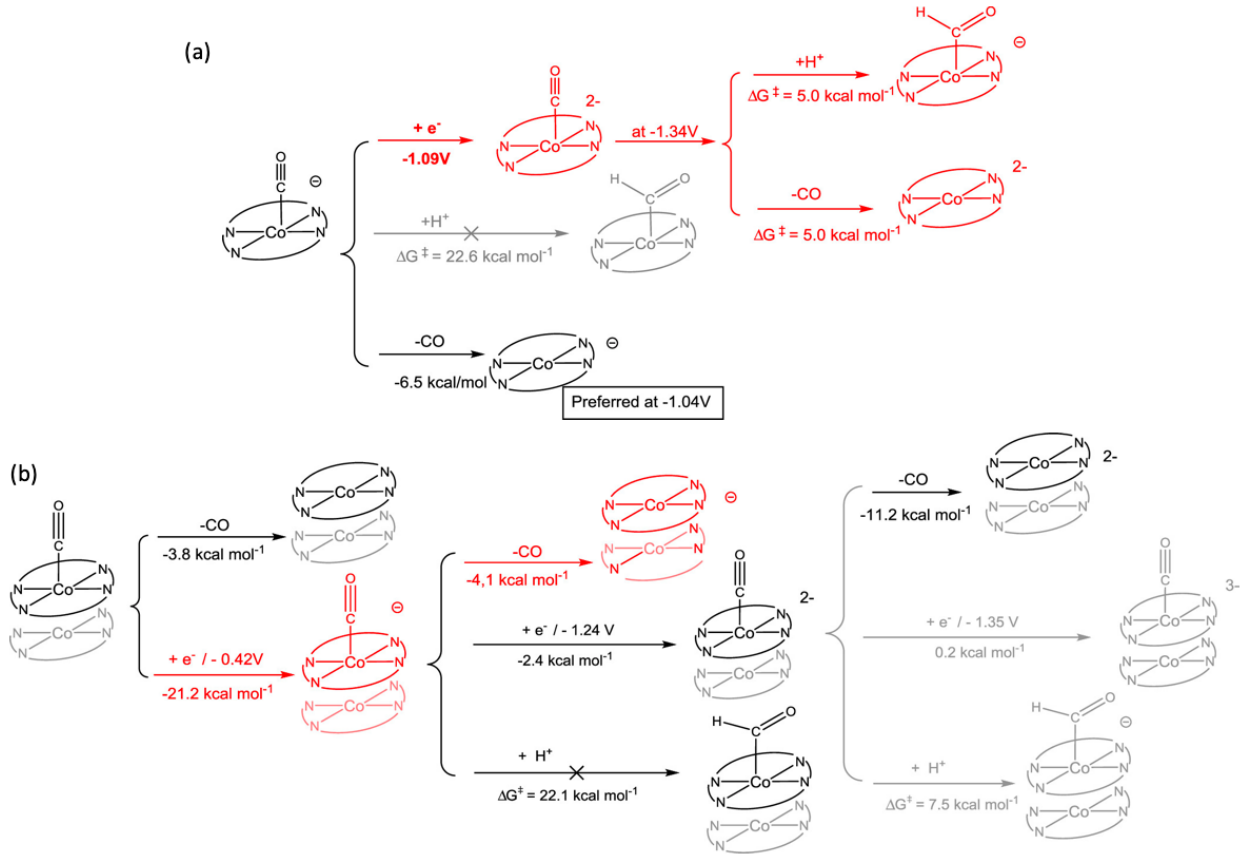

Fig. 4-4. Possible mechanisms for CO_2RR beyond CoPc-CO^-. (a) On the CoPc monomer, CO can either desorb (bottom path) or be reduced further to 2– and then protonated (top red path). Protonation at 1– is not preferred (middle grey path) (b) For CoPc dimers, only CO desorption is possible. Reduction to 2– (red path) still does not favor protonation. Figure adapted from ref. 29.

Another recent example of modified CoPc research involves the attachment of axial ligands and encapsulation within a polymer chain. Similar to the earlier cited work that incorporated CoPc within a polymer membrane,[27] Liu and McCrory have investigated the beneficial effects of CoPc encapsulated within P4VP.[30] They highlight three types of interactions that provide benefits for the polymer encapsulated CoPc, depicted in **Fig. 4-5a**. First, the axial coordination of CoPc with a pyridine ring of the polymer occurs in the primary coordination sphere (closest bonding atoms). The axial coordination offers a source of electron donation that aids in reducing CoPc for CO_2 conversion. Second is the interaction of another pyridine ring from a nearby polymer chain or a wrap-around of the same polymer chain. This secondary coordination sphere effect can stabilize

the reduced CO_2^- intermediate and lower the barrier for protonation. Thirdly, other pyridine rings along the length of the polymer can help relay protons to the active site for faster turnover.

A follow-up study by Rivera Cruz et al. provided a deeper investigation of the effects of axial coordination by a ligand molecule.[31] They studied a simplified version of the encapsulated CoPc by synthesizing ligand-modified CoPc molecules, with eight different ligands of varying σ-electron donor strength. Through studying these eight ligand-modified CoPC molecules the authors would deduce the impact of ligand-derived electron donation on the catalytic activity of CoPc. The eight different ligands chosen are referred to as L1 through L8 (**Fig. 4-5d**), where L1 = 1,3,5-triazine, L2 = pyrazine, L3 = pyridine, L4 = pyridazine, L5 = imidazole, L6 = 4-methylpyridine, L7 = 1-methyl imidazole, and L8 = 4-(dimethylamino)pyridine. The proposed reaction mechanism is shown in **Fig. 4-5b**. CoPc is first reduced before CO_2 adsorbs. The complex is then protonated to form $*CO_2H$, followed by another reduction and protonation to form H_2O and *CO, which desorbs to complete the cycle. The findings showed an increase in CO_2RR activity with increasing σ-donor strength of the axial ligand (**Fig. 4-5c**). Using DFT, it was predicted that axial coordination has the effect of increasing the energy of the dz^2 orbital of Co, and that the experimentally observed activity increase is correlated to an increased extent of charge transfer from the reduced CoPc-L complex to adsorbed CO_2.

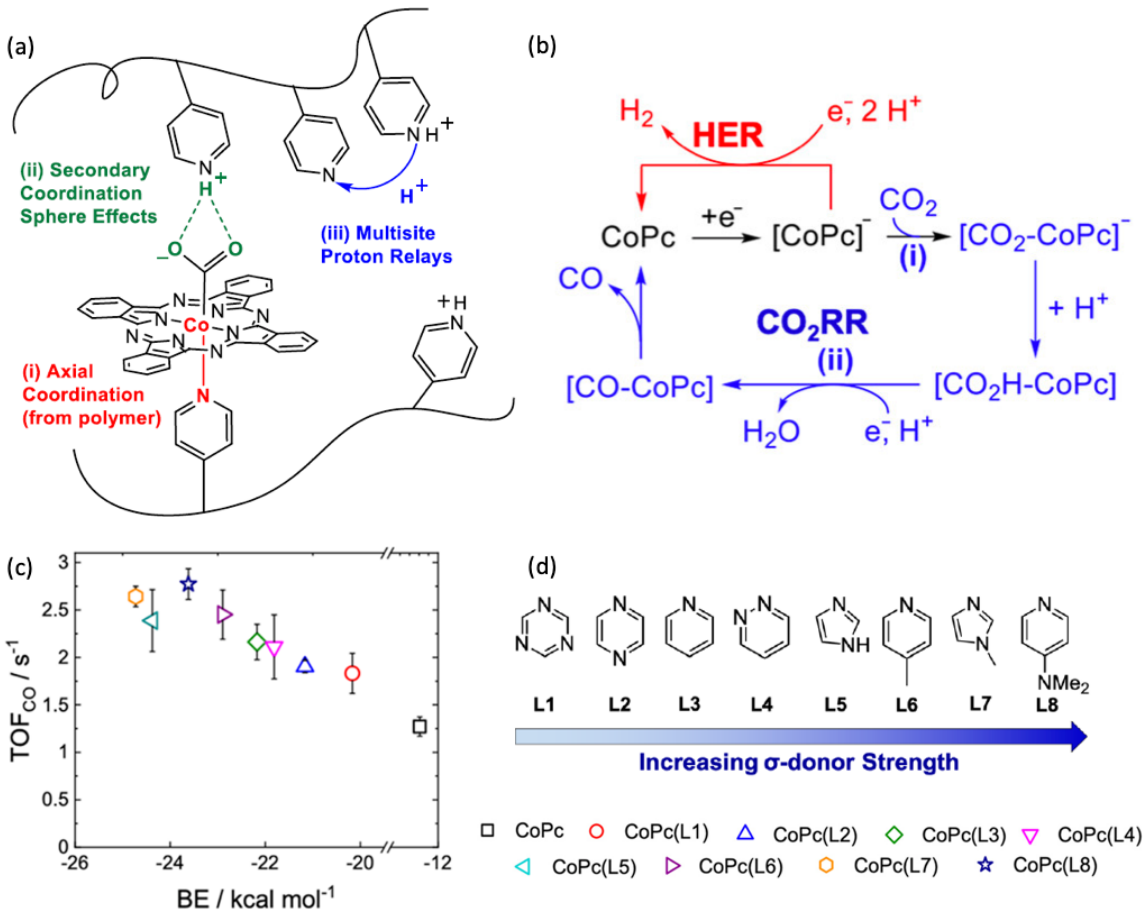

Fig. 4-5. CoPc modified by axial ligands. (a) Illustration of CoPc-P4VP highlighting the (i) axial coordination to the pyridyl groups from P4VP in the primary coordination sphere, (ii) H-bonding stabilization of reduced CO_2 intermediates in the secondary coordination sphere, and (iii) H^+ delivery via a multisite proton relay in the outer coordination sphere. (b) The proposed mechanism for CO_2RR to CO where CO_2 adsorption occurs at singly reduced $CoPc^-$. (c) Turnover frequency (TOF) trends positively with stronger CO_2 adsorption and increased electron donor strength of the ligand. (d) The eight ligands studied, in order of increasing σ-electron donor strength. Figure adapted from ref. 31.

This investigation of axial ligand effect on CoPc activity has demonstrated a benefit for the CO_2 reaction to CO, but it remains unclear if it can be modified to produce the more desirable CH_3OH product. Thus far the axial ligand modified CoPc catalyst has not been thoroughly investigated for methanation. The effect on CO_2 adsorption indicates that increased electron donation is beneficial for the initial CO_2 reduction step, but the same is not necessarily true for further reaction of CO to CH_3OH. Reaction selectivity is especially sensitive to the CO adsorption energy, because weak CO binding will allow CO to desorb and halt the reaction, while strong CO binding requires much higher potentials to react. For this reason, it is important to investigate the

effect of axial ligand coordination on the CO adsorption energy on CoPc. Furthermore, while there are several proposed mechanisms that involve different reduction levels of CoPc, it is unknown whether a certain reduction level would allow for these ligand-modified CoPc catalysts to produce CH_3OH.

For our own analysis, we have performed DFT calculations to compare the binding characteristics of CoPc modified with axial ligands for CO_2 adsorption and CO adsorption as a follow-up to the Rivera Cruz et al. study. The investigation of CO adsorption extends the current research to address the further reaction of CO to CH_3OH. We also examine the effect of reduction level of the CoPc molecule to see how the adsorption trends are affected.

4.3 Computational Methods

Density functional theory (DFT) calculations were conducted using the NWChem 7.0 software.[32] Catalyst models were built for CoPc with eight different ligands attached at the Co center, for a total of 9 different catalyst molecules (including the "no ligand" case). Ligands are named L1-L8 in order of increasing electron donor capability, similar to the prior study by Rivera Cruz et al. as shown in **Fig. 4-5d**.[31] (L1 = 1,3,5-triazine, L2 = pyrazine, L3 = pyridine, L4 = pyridazine, L5 = imidazole, L6 = 4-methylpyridine, L7 = 1-methyl imidazole, and L8 = 4-(dimethylamino)pyridine). The M11-L hybrid density functional and was used for the gas-phase geometry optimization of the CoPc-L systems.[33] The 6-31G** basis sets were employed for all atoms.[34–36] Preferred axial rotation positions were tested for each ligand using a range of starting points from 0º to 45º in 15º increments (based on the rotational symmetry of CoPc), and the relaxed position with the lowest energy result was chosen for each. Reduction levels of CoPc-L were modeled by specifying the total charge of the system. Adsorption energy calculations were

conducted by subtracting the electronic energies of the gas phase CoPc-L and adsorbate molecule energies from the energy of the CoPc-L-adsorbate complex.

4.4 Results and Discussion

We began by modeling the CoPc molecule at neutral charge in the gas phase. **Fig. 4-6** shows the geometry of relaxed CoPc (**Fig. 4-6a**) and the eight CoPc-L molecules that we modeled (**Fig. 4-6c–j**). All ligands prefer an axial rotation of about 45º relative to the Co-N bonds in CoPc, shown in **Fig. 4-6b**. This ligand orientation offers the least amount of steric strain between the CoPc N atoms and the nearest ligand H atoms. Our predictions agree with geometries presented in prior literature for these CoPc-L combinations.[31]

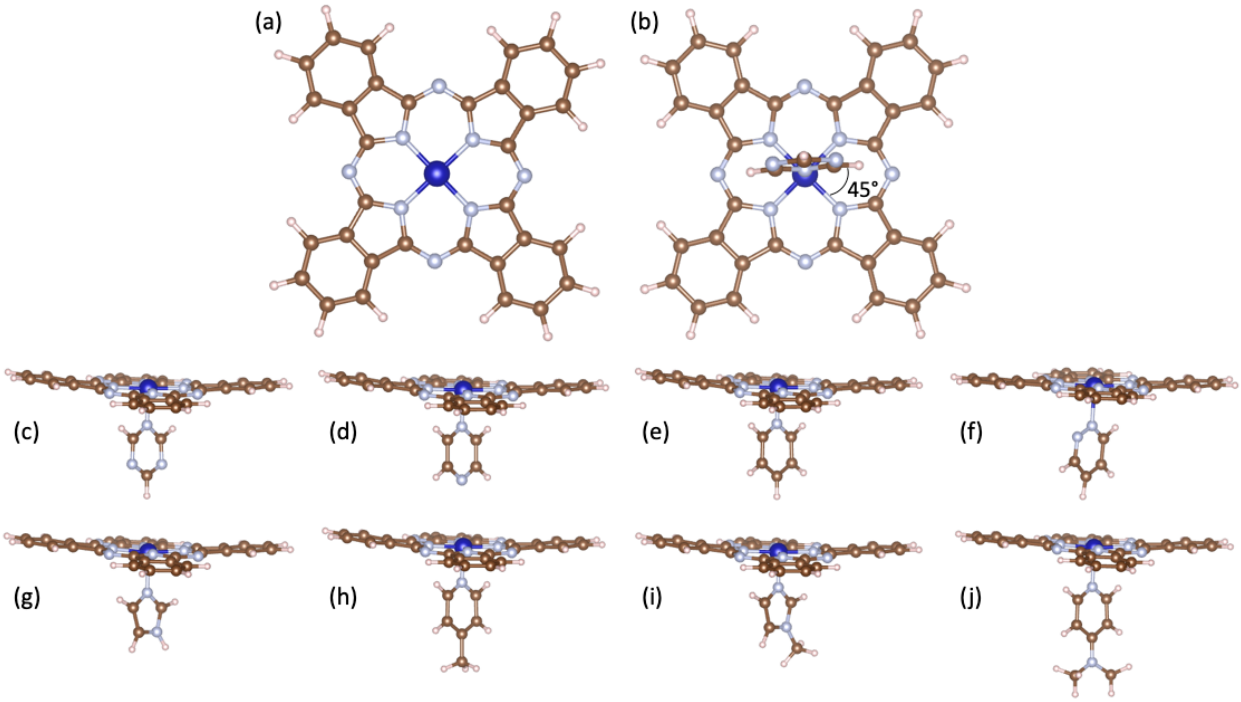

Fig. 4-6. Geometries of CoPc and CoPc-L molecules. (a) CoPc, top view; (b) CoPc-L1, bottom view, demonstrating the dihedral angle between the Co-N bond and the plane of the ligand ring is 45º. All ligands adopt approximately this same angle; (c) CoPc-L1 (1,3,5-triazine), side view; (d) CoPc-L2 (pyrazine), side view; (e) CoPc-L3 (pyridine), side view; (f) CoPc-L4 (pyridazine), side view; (g) CoPc-L5 (imidazole), side view; (h) CoPc-L6 (4-methylpyridine), side view; (i) CoPc-L7 (1-methyl imidazole), side view; (j) CoPc-L8 (4-(dimethylamino)pyridine), side view. Atom color legend: blue = Co; brown = C; gray = N; white = H.

There is a great benefit to calculating the binding strength of adsorbate molecules in the field of catalysis. Reactant binding strength can be related to other intermediate adsorbates through

linear scaling relations, and relative binding strengths are often correlated to reaction barriers through the use of Brønsted-Evans-Polanyi (BEP) relationships.[37,38] Furthermore, the reaction rate often peaks at an optimal adsorption energy of intermediate strength, with too strong binding causing an irreversible adsorption that poisons the catalyst, while too weak binding does not allow for further reaction on the surface, demonstrated by volcano plots and the Sabatier principle.[39,40] This is true for electrocatalytic CO_2 reduction to CH_3OH, which depends heavily on the adsorption strength of the *CO intermediate. If CO binds too weakly it desorbs, whereas if CO binds too strongly to the catalyst then the reaction will require very negative potentials that end up promoting the HER and thus decrease faradaic efficiency. With many important catalytic properties hinging on adsorption strength, we choose to focus our research on calculating this parameter for each CoPc-L catalyst. As the adsorption properties and reaction mechanism depend heavily on the reduction level of CoPc, we model each catalyst at three reduction levels, neutral CoPc, $CoPc^{-}$, and $CoPc^{2-}$. The adsorption energies presented here are directly calculated from DFT, and do not include corrections for entropy or enthalpy effects, zero-point energy, or solvation effects from the surrounding solvate. Still, as each of these effects will be of equal magnitude across all ligand combinations, we expect that the trends with respect to ligand electron donation strength will remain consistent. Future work should consider these effects for more quantitatively accurate predictions.

Fig. 4-7 depicts the DFT-calculated electronic adsorption energy of CO_2 (**Fig 4-7a**) and CO (**Fig 4-7b**) on each CoPc-L catalyst at each reduction level. More negative adsorption energies indicate a stronger bond. Geometries for CO_2 and CO adsorbed on CoPc-L1 are included as an example in **Fig. 4-8**. At the neutral state, CoPc does not bind CO_2 or CO very strongly regardless of ligand. CO_2 adsorption on bare CoPc is strongest at –0.17 eV, and the adsorption on ligand

modified catalysts ranges between –0.11 eV (CoPc-L2) to –0.14 eV (CoPc-L1), and there is no clear trend with respect to ligand electron donation. Similarly, CO adsorption on bare CoPc is strongest at –0.33 eV, and the adsorption on ligand modified catalysts ranges between –0.18 eV (CoPc-L4) to –0.11 eV (CoPc-L1), again with no clear trend with respect to ligand electron donation.

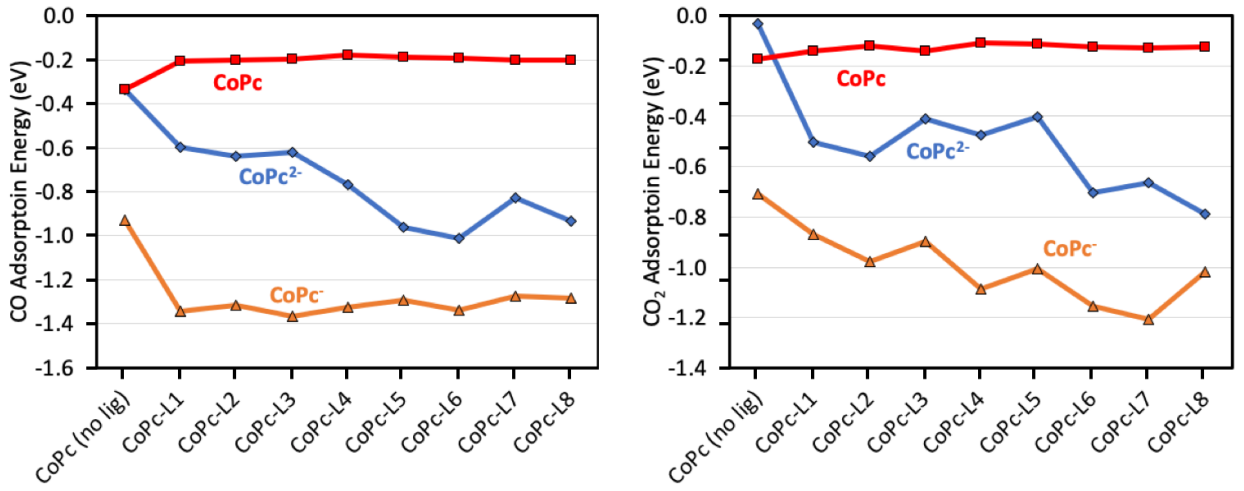

Fig. 4-7. Adsorption energy of CO_2 and CO to CoPc and CoPc(L) molecules. (a) CO_2 adsorption energy for neutral CoPc (red), $CoPc^-$ (orange), and $CoPc^{2-}$ (blue). (b) CO adsorption energy for neutral CoPc (red), $CoPc^-$ (orange), and $CoPc^{2-}$ (blue).

A more noticeable trend emerges for the singly and doubly reduced CoPc catalysts. Upon single reduction, the adsorption strength becomes much stronger for CO_2 and CO, but they follow opposite trends with respect to ligand electron donation. From L1 to L8, the CO_2 adsorption energy generally becomes more negative, with the weakest binding on CoPc-L1$^-$ at –0.87 eV and the strongest binding on CoPc-L7$^-$ at –1.21 eV. We can compare our results for CO_2 adsorption on CoPc-L$^-$ to the study by Rivera Cruz et al., since similar methodology and identical ligands were chosen.[31] Our results agree well, with all values deviating no more than 15% and following the same overall trend. When analyzing CO adsorption, the binding strength follows a trend of slightly weakening adsorption from L1 to L8, ranging from –1.36 eV for CoPc-L3$^-$ and –1.27 eV for CoPc-L7$^-$. Still, the trend for CO is not as pronounced on $CoPc^-$ systems as compared to CO_2. This

reversal of adsorption strength trend between CO_2 and CO presents an interesting phenomenon, where the linear scaling between CO and CO_2 adsorption is broken. If this trend extends outward to other ligands of more potent electron donation strength, one could choose a ligand that offers strong CO_2 adsorption but relatively weak CO adsorption. This strategy would be beneficial for halting the reaction at CO, but may not be desired for a full reaction to methanol where you would desire further CO conversion before desorption.

As for double reduction, the CO_2 and CO adsorption energies on $CoPc^{2-}$ are more moderate, lying between neutral CoPc and $CoPc^{-}$. Both adsorbates follow a trend of increasing strength with respect to ligand electron donation. From L1 to L8, CO_2 binding energy grows more negative from –0.50 eV (CoPc-L1^{2-}) to –0.79 eV (CoPc-L8^{2-}). Similarly, CO binding energy grows more negative from –0.60 eV (CoPc-L1^{2-}) to –0.94 eV (CoPc-L8^{2-}). The interatomic distances between Co and the adsorbed C atom shown in **Fig. 4-8** seem to correlate well with binding energy for CO, with the bond distance for CoPc-L1^{-} being shortest (strongest bond), followed by CoPc-L1^{2-} and CoPc-L1. The correlation does not carry for CO_2 adsorption, however, but there is not a significant amount of variation in bond distance for the three systems.

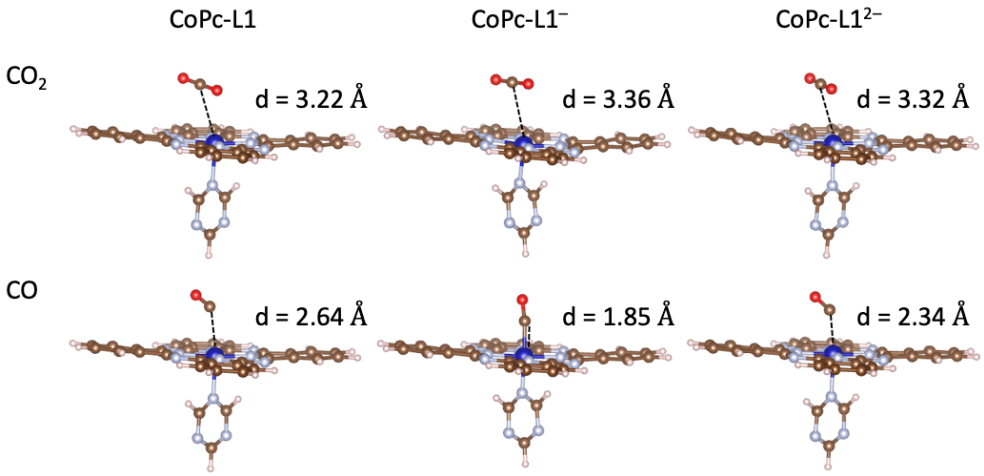

Fig. 4-8. Geometries of adsorbed CO_2 and CO on CoPc-L1. Geometries are given for each of the three reduction states, neutral, 1– and 2–. Interatomic distances between Co and the C atom of CO/CO_2 are given next to each bond.

More work is needed to know the preferred reduction state of CoPc that occurs during the reaction of CO to methanol, as has been explored for CO_2 to CO.[31] The reduction level at this stage of the overall mechanism would have a strong impact on the binding characteristics of *CO and later intermediates. Such a study would involve a reaction mechanism analysis for steps downstream of *CO to assess which reduction level is preferred and matches closest with experiment.

It is difficult to conclude the exact effect that these adsorption trends have on the overall reaction rate and selectivity to methanol, since much would depend on the rate-limiting step. In cases where the CO_2 adsorption is rate-limiting, then stronger binding of CO_2 would no doubt be beneficial. If downstream reaction steps are rate limiting, then the binding strength of CO may be more impactful. In most investigations of CoPc, the adsorption of CO_2 is shown to be rate limiting.[30,41,42] From experimental studies of similar catalysts, it was demonstrated that the addition of axial coordination to CoPc caused a change in rate-limiting step from CO_2 adsorption to a subsequent mechanism step.[30,31] This finding was attributed to the increased binding energy of CO_2 on CoPc-L^- compared to $CoPc^-$, which we have also reproduced with our own data. Since these prior studies demonstrated that the addition of axially coordinated ligands improved CO_2 reduction performance in part due to stronger CO_2 binding at the singly reduced state, it follows that the weaker adsorption on $CoPc^{2-}$ would not be beneficial. Furthermore, since double reduction of CoPc would require a higher reduction potential to achieve, it risks promoting the competing HER ahead of CO_2RR.

4.5 Conclusions

From our analysis, we can confirm that increased electron donation from the ligand does correlate with improved CO_2 adsorption capability for singly reduced CoPc, but has a slight reverse trend

for CO adsorption upon single reduction. The magnitude of both CO_2 and CO adsorption is higher for CoPc-L^- than for CoPc-L^{2-} or neutral CoPc-L, and this has been demonstrated to benefit CO_2 reduction in other research.[31] We would recommend a ligand choice that satisfies the requirement for high CO_2 adsorption strength and still has the desired CO adsorption capability. Future work should investigate what the ideal CO adsorption strength is for this catalyst to produce methanol, examining how further reaction steps are sensitive to the change in adsorption from the ligand choice. Additional research could also be conducted for ligands with even more electron donation capability to see if the trend extends beyond the observed range.

Mechanistic analysis with microkinetic modeling would help elucidate the sensitivity of downstream reaction steps to the CO_2 and CO adsorption strength. By modeling each step of several proposed reaction mechanisms, the calculated apparent activation barriers and turnover frequencies can be compared to experimentally observed current densities to evaluate the feasibility of each mechanism. This would uncover not only the effect of the ligand on CO2RR but also the role of different reduction levels at different steps of the reaction.

This work investigated only the axial coordination aspect of a polymer-grafted CoPc catalyst. Ultimately, a more accurate model of CoPc grafted to a polymer chain would require a combination of more sophisticated modeling techniques. The CoPc-polymer complex could be modeled using molecular dynamics simulations to observe the preferred degree of interaction between CoPc and the polymer at locations distant from the grafting site. Then these local interactions can be modeled separately in a DFT model that includes explicit water molecules capable of H-bonding and proton shuttling. The inclusion of proton relay could be conducted by a combined molecular dynamics and DFT approach, finding statistically significant H_2O/pyridine conformations using molecular dynamics, and sampling rare events with DFT to find the proton

transfer barrier between adjacent pyridine rings. We hope that our work lays a groundwork for future investigation of these related research problems.

4.6 References

(1) Nitopi, S.; Bertheussen, E.; Scott, S. B.; Liu, X.; Engstfeld, A. K.; Horch, S.; Seger, B.; Stephens, I. E. L.; Chan, K.; Hahn, C.; Nørskov, J. K.; Jaramillo, T. F.; Chorkendorff, I. Progress and Perspectives of Electrochemical CO2 Reduction on Copper in Aqueous Electrolyte. *Chem. Rev.* **2019**, *119* (12), 7610–7672. https://doi.org/10.1021/acs.chemrev.8b00705.

(2) Gu, Z.; Shen, H.; Shang, L.; Lv, X.; Qian, L.; Zheng, G. Nanostructured Copper-Based Electrocatalysts for CO2 Reduction. *Small Methods* **2018**, *2* (11), 1800121. https://doi.org/10.1002/smtd.201800121.

(3) Lees, E. W.; Mowbray, B. A. W.; Parlane, F. G. L.; Berlinguette, C. P. Gas Diffusion Electrodes and Membranes for CO2 Reduction Electrolysers. *Nat Rev Mater* **2022**, *7* (1), 55–64. https://doi.org/10.1038/s41578-021-00356-2.

(4) Gabardo, C. M.; O'Brien, C. P.; Edwards, J. P.; McCallum, C.; Xu, Y.; Dinh, C.-T.; Li, J.; Sargent, E. H.; Sinton, D. Continuous Carbon Dioxide Electroreduction to Concentrated Multi-Carbon Products Using a Membrane Electrode Assembly. *Joule* **2019**, *3* (11), 2777–2791. https://doi.org/10.1016/j.joule.2019.07.021.

(5) Nie, X.; Luo, W.; Janik, M. J.; Asthagiri, A. Reaction Mechanisms of CO2 Electrochemical Reduction on Cu(111) Determined with Density Functional Theory. *Journal of Catalysis* **2014**, *312*, 108–122. https://doi.org/10.1016/j.jcat.2014.01.013.

(6) Walsh, J. J.; Neri, G.; Smith, C. L.; Cowan, A. J. Water-Soluble Manganese Complex for Selective Electrocatalytic CO2 Reduction to CO. *Organometallics* **2019**, *38* (6), 1224–1229. https://doi.org/10.1021/acs.organomet.8b00336.

(7) Cometto, C.; Chen, L.; Anxolabéhère-Mallart, E.; Fave, C.; Lau, T.-C.; Robert, M. Molecular Electrochemical Catalysis of the CO2-to-CO Conversion with a Co Complex: A Cyclic Voltammetry Mechanistic Investigation. *Organometallics* **2019**, *38* (6), 1280–1285. https://doi.org/10.1021/acs.organomet.8b00555.

(8) Zhang, S.; Fan, Q.; Xia, R.; Meyer, T. J. CO2 Reduction: From Homogeneous to Heterogeneous Electrocatalysis. *Acc. Chem. Res.* **2020**, *53* (1), 255–264. https://doi.org/10.1021/acs.accounts.9b00496.

(9) Lin, S.; Diercks, C. S.; Zhang, Y.-B.; Kornienko, N.; Nichols, E. M.; Zhao, Y.; Paris, A. R.; Kim, D.; Yang, P.; Yaghi, O. M.; Chang, C. J. Covalent Organic Frameworks Comprising Cobalt Porphyrins for Catalytic CO2 Reduction in Water. *Science* **2015**, *349* (6253), 1208–1213. https://doi.org/10.1126/science.aac8343.

(10) Hod, I.; Sampson, M. D.; Deria, P.; Kubiak, C. P.; Farha, O. K.; Hupp, J. T. Fe-Porphyrin-Based Metal–Organic Framework Films as High-Surface Concentration, Heterogeneous Catalysts for Electrochemical Reduction of CO2. *ACS Catal.* **2015**, *5* (11), 6302–6309. https://doi.org/10.1021/acscatal.5b01767.

(11) Costentin, C.; Savéant, J.-M. Homogeneous Molecular Catalysis of Electrochemical Reactions: Catalyst Benchmarking and Optimization Strategies. *J. Am. Chem. Soc.* **2017**, *139* (24), 8245–8250. https://doi.org/10.1021/jacs.7b02879.

(12) Zhang, B.; Asakura, H.; Zhang, J.; Zhang, J.; De, S.; Yan, N. Stabilizing a Platinum1 Single-Atom Catalyst on Supported Phosphomolybdic Acid without Compromising Hydrogenation Activity. *Angewandte Chemie* **2016**, *128* (29), 8459–8463. https://doi.org/10.1002/ange.201602801.

(13) Yang, F.; Song, P.; Liu, X.; Mei, B.; Xing, W.; Jiang, Z.; Gu, L.; Xu, W. Highly Efficient CO2 Electroreduction on ZnN4-Based Single-Atom Catalyst. *Angewandte Chemie International Edition* **2018**, *57* (38), 12303–12307. https://doi.org/10.1002/anie.201805871.
(14) Wu, Y.; Jiang, Z.; Lu, X.; Liang, Y.; Wang, H. Domino Electroreduction of CO2 to Methanol on a Molecular Catalyst. *Nature* **2019**, *575* (7784), 639–642. https://doi.org/10.1038/s41586-019-1760-8.
(15) Liu, X.; Li, B.-Q.; Ni, B.; Wang, L.; Peng, H.-J. A Perspective on the Electrocatalytic Conversion of Carbon Dioxide to Methanol with Metallomacrocyclic Catalysts. *Journal of Energy Chemistry* **2022**, *64*, 263–275. https://doi.org/10.1016/j.jechem.2021.04.059.
(16) Liu, Y.; Li, F.; Zhang, X.; Ji, X. Recent Progress on Electrochemical Reduction of CO2 to Methanol. *Current Opinion in Green and Sustainable Chemistry* **2020**, *23*, 10–17. https://doi.org/10.1016/j.cogsc.2020.03.009.
(17) Keeratithivakorn, P.; Tunhoo, B.; Thiwawong, T.; Nukeaw, J. CoPc/CdS Hybrid Photovoltaic Device. *Advanced Materials Research* **2010**, *93–94*, 570–573. https://doi.org/10.4028/www.scientific.net/AMR.93-94.570.
(18) Kao, P.-C.; Chu, S.-Y.; You, Z.-X.; Liou, S. J.; Chuang, C.-A. Improved Efficiency of Organic Light-Emitting Diodes Using CoPc Buffer Layer. *Thin Solid Films* **2006**, *498* (1), 249–253. https://doi.org/10.1016/j.tsf.2005.07.120.
(19) Kumar, P.; Kumar, A.; Sreedhar, B.; Sain, B.; Ray, S. S.; Jain, S. L. Cobalt Phthalocyanine Immobilized on Graphene Oxide: An Efficient Visible-Active Catalyst for the Photoreduction of Carbon Dioxide. *Chemistry – A European Journal* **2014**, *20* (20), 6154–6161. https://doi.org/10.1002/chem.201304189.
(20) Iliev, V.; Alexiev, V.; Bilyarska, L. Effect of Metal Phthalocyanine Complex Aggregation on the Catalytic and Photocatalytic Oxidation of Sulfur Containing Compounds. *Journal of Molecular Catalysis A: Chemical* **1999**, *137* (1), 15–22. https://doi.org/10.1016/S1381-1169(98)00069-7.
(21) İşci, Ü.; Afanasiev, P.; Millet, J.-M. M.; Kudrik, E. V.; Ahsen, V.; Sorokin, A. B. Preparation and Characterization of μ-Nitrido Diiron Phthalocyanines with Electron-Withdrawing Substituents: Application for Catalytic Aromatic Oxidation. *Dalton Trans.* **2009**, No. 36, 7410–7420. https://doi.org/10.1039/B902592H.
(22) Karandikar, P.; Chandwadkar, A. J.; Agashe, M.; Ramgir, N. S.; Sivasanker, S. Liquid Phase Oxidation of Alkanes Using Cu/Co-Perchlorophthalocyanine Immobilized MCM-41 under Mild Reaction Conditions. *Applied Catalysis A: General* **2006**, *297* (2), 220–230. https://doi.org/10.1016/j.apcata.2005.09.012.
(23) Yue, Z.; Ou, C.; Ding, N.; Tao, L.; Zhao, J.; Chen, J. Advances in Metal Phthalocyanine Based Carbon Composites for Electrocatalytic CO2 Reduction. *ChemCatChem* **2020**, *12* (24), 6103–6130. https://doi.org/10.1002/cctc.202001126.
(24) Chang, Q.; Liu, Y.; Lee, J.-H.; Ologunagba, D.; Hwang, S.; Xie, Z.; Kattel, S.; Lee, J. H.; Chen, J. G. Metal-Coordinated Phthalocyanines as Platform Molecules for Understanding Isolated Metal Sites in the Electrochemical Reduction of CO2. *J. Am. Chem. Soc.* **2022**, *144* (35), 16131–16138. https://doi.org/10.1021/jacs.2c06953.
(25) Kapusta, S.; Hackerman, N. Carbon Dioxide Reduction at a Metal Phthalocyanine Catalyzed Carbon Electrode. *J. Electrochem. Soc.* **1984**, *131* (7), 1511. https://doi.org/10.1149/1.2115882.

(26) Lieber, C. M.; Lewis, N. S. Catalytic Reduction of Carbon Dioxide at Carbon Electrodes Modified with Cobalt Phthalocyanine. *J. Am. Chem. Soc.* **1984**, *106* (17), 5033–5034. https://doi.org/10.1021/ja00329a082.
(27) Abe, T.; Yoshida, T.; Tokita, S.; Taguchi, F.; Imaya, H.; Kaneko, M. Factors Affecting Selective Electrocatalytic Co2 Reduction with Cobalt Phthalocyanine Incorporated in a Polyvinylpyridine Membrane Coated on a Graphite Electrode. *Journal of Electroanalytical Chemistry* **1996**, *412* (1), 125–132. https://doi.org/10.1016/0022-0728(96)04631-1.
(28) Choi, J.; Wagner, P.; Gambhir, S.; Jalili, R.; MacFarlane, D. R.; Wallace, G. G.; Officer, D. L. Steric Modification of a Cobalt Phthalocyanine/Graphene Catalyst To Give Enhanced and Stable Electrochemical CO_2 Reduction to CO. *ACS Energy Lett.* **2019**, *4* (3), 666–672. https://doi.org/10.1021/acsenergylett.8b02355.
(29) Chen, X.; Wei, D.; Ahlquist, M. S. G. Aggregation and Significant Difference in Reactivity Therein: Blocking the CO2-to-CH3OH Reaction. *Organometallics* **2021**, *40* (17), 3087–3093. https://doi.org/10.1021/acs.organomet.1c00431.
(30) Liu, Y.; McCrory, C. C. L. Modulating the Mechanism of Electrocatalytic CO2 Reduction by Cobalt Phthalocyanine through Polymer Coordination and Encapsulation. *Nat Commun* **2019**, *10* (1), 1683. https://doi.org/10.1038/s41467-019-09626-8.
(31) Rivera Cruz, K. E.; Liu, Y.; Soucy, T. L.; Zimmerman, P. M.; McCrory, C. C. L. Increasing the CO2 Reduction Activity of Cobalt Phthalocyanine by Modulating the σ-Donor Strength of Axially Coordinating Ligands. *ACS Catal.* **2021**, *11* (21), 13203–13216. https://doi.org/10.1021/acscatal.1c02379.
(32) Valiev, M.; Bylaska, E. J.; Govind, N.; Kowalski, K.; Straatsma, T. P.; Van Dam, H. J. J.; Wang, D.; Nieplocha, J.; Apra, E.; Windus, T. L.; de Jong, W. A. NWChem: A Comprehensive and Scalable Open-Source Solution for Large Scale Molecular Simulations. *Computer Physics Communications* **2010**, *181* (9), 1477–1489. https://doi.org/10.1016/j.cpc.2010.04.018.
(33) Peverati, R.; Truhlar, D. G. M11-L: A Local Density Functional That Provides Improved Accuracy for Electronic Structure Calculations in Chemistry and Physics. *J. Phys. Chem. Lett.* **2012**, *3* (1), 117–124. https://doi.org/10.1021/jz201525m.
(34) Petersson, G. A.; Bennett, A.; Tensfeldt, T. G.; Al-Laham, M. A.; Shirley, W. A.; Mantzaris, J. A Complete Basis Set Model Chemistry. I. The Total Energies of Closed-shell Atoms and Hydrides of the First-row Elements. *J. Chem. Phys.* **1988**, *89* (4), 2193–2218. https://doi.org/10.1063/1.455064.
(35) Petersson, G. A.; Al-Laham, M. A. A Complete Basis Set Model Chemistry. II. Open-shell Systems and the Total Energies of the First-row Atoms. *J. Chem. Phys.* **1991**, *94* (9), 6081–6090. https://doi.org/10.1063/1.460447.
(36) Rassolov, V. A.; Pople, J. A.; Ratner, M. A.; Windus, T. L. 6-31G* Basis Set for Atoms K through Zn. *The Journal of Chemical Physics* **1998**, *109* (4), 1223. https://doi.org/10.1063/1.476673.
(37) Bronsted, J. N. Acid and Basic Catalysis. *Chem. Rev.* **1928**, *5* (3), 231–338. https://doi.org/10.1021/cr60019a001.
(38) Evans, M. G.; Polanyi, M. Inertia and Driving Force of Chemical Reactions. *Trans. Faraday Soc.* **1938**, *34* (0), 11–24. https://doi.org/10.1039/TF9383400011.
(39) Sabatier, P. *La catalyse en chimie organique*; C. Béranger, 1920.
(40) Ooka, H.; Huang, J.; Exner, K. S. The Sabatier Principle in Electrocatalysis: Basics, Limitations, and Extensions. *Frontiers in Energy Research* **2021**, *9*.

(41) Ren, X.; Liu, S.; Li, H.; Ding, J.; Liu, L.; Kuang, Z.; Li, L.; Yang, H.; Bai, F.; Huang, Y.; Zhang, T.; Liu, B. Electron-Withdrawing Functional Ligand Promotes CO2 Reduction Catalysis in Single Atom Catalyst. *Sci. China Chem.* **2020**, *63* (12), 1727–1733. https://doi.org/10.1007/s11426-020-9847-9.
(42) Zhu, M.; Ye, R.; Jin, K.; Lazouski, N.; Manthiram, K. Elucidating the Reactivity and Mechanism of CO2 Electroreduction at Highly Dispersed Cobalt Phthalocyanine. *ACS Energy Lett.* **2018**, *3* (6), 1381–1386. https://doi.org/10.1021/acsenergylett.8b00519.

Chapter 5

Conclusion and Outlook

Parts of this chapter were adapted from E. Musa, F. Doherty, and B. R. Goldsmith, "Accelerating the structure search of catalysts with machine learning*." Curr. Opin. Chem. Eng.*, 2021, **35**, 100771.

5.1 Summary

The goal of the research presented in this dissertation was to elucidate the trends of single-atom catalyst activity and selectivity for CO_2 reduction through density functional theory modeling, especially focusing on the effects of catalyst structure at the atomic level. We explored single-atom catalyst systems for CO_2 reduction in the areas of thermal catalysis, plasma catalysis, and electrocatalysis. This section summarizes the principal contributions of this dissertation.

- In Chapter 2, we explored the mechanism for the thermocatalytic reverse water gas shift reaction (RWGSR, $CO_2 + H_2 \rightleftharpoons CO + H_2O$) catalyzed by rhodium single atoms supported on titania (Rh_1/TiO_2). By investigating the potential candidates for single atom active sites, three mechanisms were explored in further detail using microkinetic modeling. The main findings suggested that a reaction mechanism involving oxygen vacancies within the TiO_2 support offers a more favorable energy pathway for CO_2 reduction than a pristine TiO_2 surface. We also compared the single atom to different models of supported nanoclusters of varying size (Rh_2 – Rh_8). We hypothesized that there would be a distinct change in

behavior based on cluster size that would determine the selectivity toward either RWGSR or methanation. Indeed, we found that single atoms are uniquely selective toward RWGSR over methanation due to weak binding of CO and limited availability for binding additional H_2 for further hydrogenation.

- In Chapter 3, we examined the effect of plasma-induced surface charge on the CO_2 reduction reaction catalyzed by supported single atoms. By modeling the CO_2 adsorption strength and dissociation barriers for six different single metal atoms on both reducible and irreducible supports, we showed a strong increase in CO_2 adsorption and a lowering of dissociation barriers across the board for all metals and supports due to the excess charge. The amount of charge on the single metal atom correlated with the increase in CO_2 adsorption strength and a decrease in CO_2 dissociation barrier, indicating that single-atom/support systems that adopt a greater charge from low temperature plasma demonstrate beneficial properties for CO_2 reduction. Our results and analysis give better understanding of how catalyst surface charging could enable manipulation of surface coverages and intrinsic kinetics.
- In Chapter 4, we investigated the capability of cobalt phthalocyanine (CoPc) to catalyze the CO_2 reduction reaction as a ligand-modified electrocatalyst. We modeled CoPc with eight different ligands of varying electron donor strength at three different reduction levels to determine the trend with CO_2 and CO adsorption. The results for CO adsorption show a reverse trend with respect to ligand electron donation strength compared to adsorption of CO_2. This shows that a careful choice of ligand must be made that optimizes for strong CO_2 adsorption and a moderate CO adsorption in order to optimize for methanol selectivity.

Each chapter explored a different energetic driving force for the reduction of CO_2 via single atom catalysts, but there are several common themes that can be taken from each. The importance of catalyst geometry, and especially electronic structure, is a prominent connection between the research findings of each chapter. Electronic structure of the active catalyst site plays a key role in determining the binding of reactants and key intermediates, which in turn affects activity and selectivity. In the case of single atoms compared to nanoclusters, the limited ability for single atoms to bind additional hydrogen results in their selectivity toward RWGSR. For plasma catalysis and electrocatalysis, the delivery of extra electrons to the active sight strengthens the binding of CO_2 and facilitates CO_2 reduction. In each case, further control over the catalyst geometry and electronic structure can enable researchers to tune the precise chemistry of these catalysts.

5.2 Extension of Current Research

While the work presented in this dissertation has clarified several key mechanistic aspects of single-atom catalysis for CO_2 reduction that were previously unknown, there is still much to explore for this environmentally relevant reaction. This section will provide an overview of the possible extensions of the work presented in this dissertation.

Chapter 2 demonstrated how in depth mechanistic analysis of thermocatalytic CO_2 conversion is highly dependent on the modeling of the catalyst structure and the inclusion of defects in the model. The single atom mechanism that allowed for oxygen vacancy formation outperformed the other two mechanisms and compared more closely with experimentally observed turnover frequency. Future work in this project area would include a similar treatment for the nanocluster model, conducting a full mechanistic analysis of CO_2 to CH_4. The cluster models should be assessed under reaction conditions, allowing for cluster restructuring under relevant temperature and pressure.[1] Support defects should also be considered, allowing for additional

binding configurations for adsorbates interacting with the support surface. There is also a recognized phenomenon of strong metal-support interactions (SMSI) that can create an overlayer of oxide from the support on top of the metal cluster.[2,3] This SMSI overlayer has been shown to lower overall activity and reverse the selectivity trend for nanoclusters, now showing a preference for CO production instead of CH_4.[4,5] Modeling this SMSI overlayer is an ongoing challenge with some promising early results,[6,7] but further research in this area is needed to connect the SMSI structure to catalytic properties of interest.

Chapter 3 elucidated the significant impact of plasma-induced surface charge on single-atom catalyst characteristics. Still, this only explores one effect of plasma-surface interactions that likely occur during the CO_2 reduction reaction. Other work has focused on different individual effects of plasma enhanced catalysis, such as the presence of radicals that can undergo Eley-Rideal reactions,[8] or the effect of excited vibrational states that lower activation barriers for dissociation reactions.[9] No model to date has included all these effects together, and there are still other interactions that have yet to be explored closely. With the ultimate goal being a multiscale model that captures a wide range of plasma effects, we must work toward this by accurately modeling additional interactions and combining them to judge their relative impact.[10] **Fig. 5-1** illustrates the concept of such a multi-scale model that can be developed for plasma catalysis. The model would not only explore the atomic scale interactions that we have mentioned in this dissertation, but also a macroscale model of plasma fluid within the reactor and a mesoscale model of the catalyst pores. The combination of these scales working together is a complex problem that will require advancements in our current computational capacity, but ongoing improvements to highly parallel computing show that such a proposition is likely possible in the future.

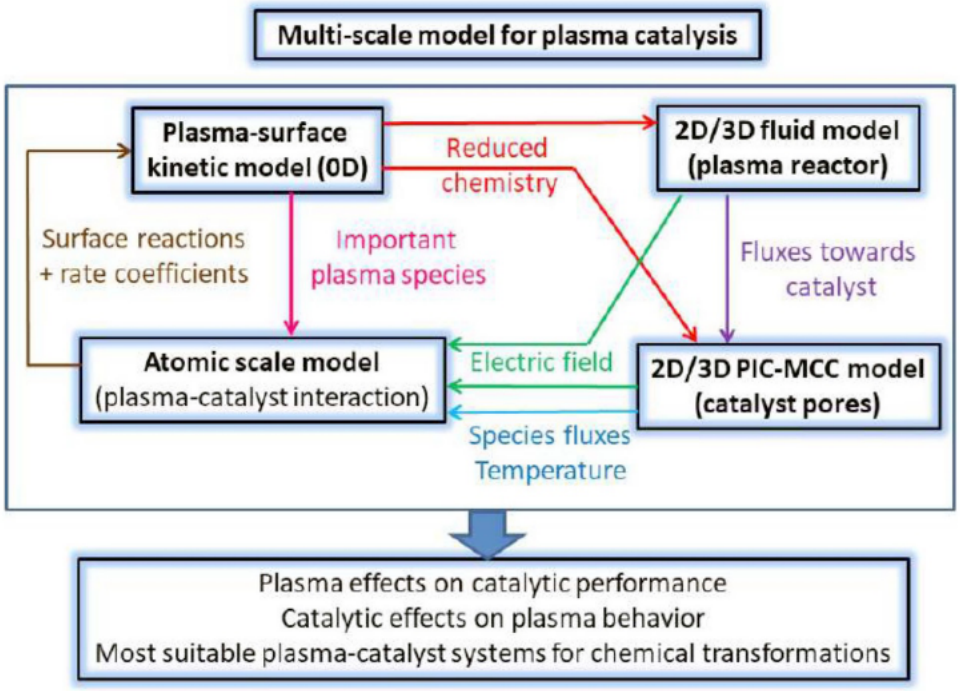

Fig. 5-1. Concept of an ultimate multi-scale model of plasma catalysis. The complexity of plasma catalysis is captured by a series of interacting models of different scale, including surface kinetics, atomic scale geometries, plasma fluid flow within the reactor, and plasma interactions within catalyst pores. Image adapted from ref. 10.

Chapter 4 examined the effect of ligand electron donation and reduction level on the CoPc catalyst for CO_2 electroreduction. Future work should investigate what the ideal CO adsorption strength is for this catalyst to produce methanol, examining how further reaction steps are sensitive to the change in adsorption from the ligand choice. Additional research could also be conducted to extend the ligand investigation beyond the observed range of electron donation strength to see what trends emerge for CO adsorption. Furthermore, a more accurate model of CoPc grafted to a polymer chain would help investigate the combined effects of axial coordination, intermediate stabilization from nearby polymer segments, and proton relay from distant parts of the polymer chain to the active site. The CoPc-polymer complex could be modeled using molecular dynamics simulations to observe the preferred degree of interaction between CoPc and the polymer at locations distant from the grafting site. Then these local interactions can be modeled separately in a DFT model that includes explicit water molecules capable of H-bonding and proton shuttling.

5.3 Catalyst Structure Explored Through Modeling and Machine Learning

Developing improved catalytic processes for CO_2 conversion will require advances in controlling and understanding single atom structures under reaction conditions. Advanced synthesis approaches are needed to develop catalysts with well-defined active sites to clarify structure-performance relationships for target reactions and improved stability for practical applications. It is also valuable to be able to compare single atoms to nanoclusters of varying size, and determining accurate models for the structure of nanoclusters under reaction conditions remains a challenging task. Theoretical modeling approaches continue to improve for studying single atom and nanocluster stability under reaction conditions, but the field of predictive synthesis of single atoms and nanoclusters to guide experiments is still developing. Sophisticated techniques such as *ab initio* molecular dynamics[11,12] and grand canonical Monte Carlo[13,14] allow for a wide range of exploration of catalyst surfaces and morphologies exposed to reactants, but these techniques are computationally demanding. Accurately predicting the thermodynamically favored structures of catalysts is difficult due to the relatively high computational expense of accurate quantum mechanical methods and the high dimensionality of the potential energy surface for these catalyst structures.

To address these challenges, researchers are utilizing fast, inexpensive machine learning (ML) calculations with structure-search workflows to complement quantum mechanical calculations and expedite the identification of relevant catalytic structures.[15–18] For example, **Fig. 5-2** shows a representative ML-assisted structure search workflow. Structure-search algorithms (**Fig. 5-2a**) can combine with surrogate ML models (**Fig. 5-2b**) trained on data generated by high-fidelity QM calculations to rapidly predict energies and forces of structures with relatively high accuracy (**Fig. 5-2c**), enabling researchers to model larger, more complex catalytic systems. Once

catalyst structures are identified, reaction mechanisms can be predicted to test mechanistic hypotheses, examine plausible active sites, and compare with experiment (**Fig. 5-2d**).

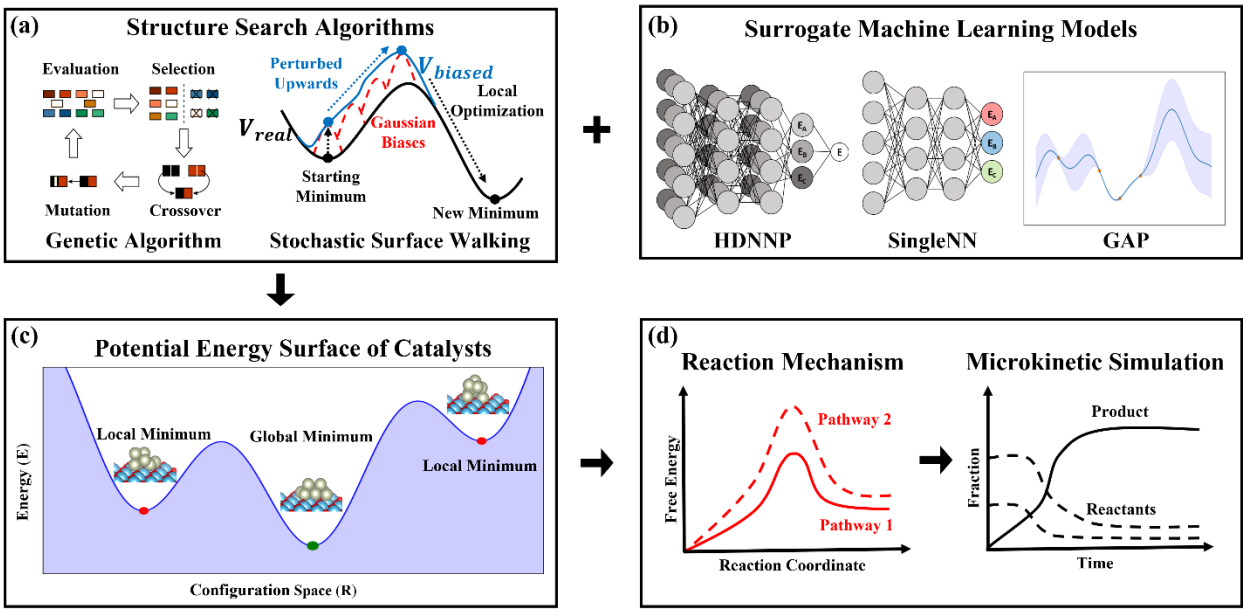

Fig. 5-2. Representative structure-search workflow aided by a surrogate machine learning model. (a) Structure-search algorithms like genetic algorithms (GA) and stochastic surface walking (SSW) can combine with (b) surrogate machine learning models such as High Dimensional Neural Network Potential (HDNNPs), Single Neural Network (SingleNNs), or Gaussian Approximation Potential (GAPs) to (c) accelerate the identification of stable or metastable catalyst structures, which is a prerequisite for (d) accurately modeling reaction mechanisms and performing first-principles microkinetic simulations. Panel (d) adapted from ref. 19.

Although ML can accelerate the structure search of catalytic systems, there are multiple interconnected challenges associated with improving the accuracy, reliability, and extensibility of ML models for computational catalysis. Dataset construction is a fundamental aspect of any application involving ML, though increasing the efficiency of assembling new datasets and utilizing existing ones is especially important in catalysis, as data is generally scarce due to the high computational expense of quantum mechanical calculations and difficulty in high-throughput experimentation. Furthermore, the amount of needed training data grows with the size and complexity of systems being studied. Approaches to address this persistent issue involve techniques such as transfer learning[20,21] and active learning.[22,23] Another approach is to identify the domain of applicability (i.e., regions in the feature space where the model's predictions can be

trusted). Identifying domains of applicability can help validate whether a model trained on a particular dataset can accurately predict the properties of the system under study.[24]

When searching structures of materials using machine learned potentials (MLPs), new environments are explored that may fall outside of the domain of applicability of the MLP model, even with due diligence in creating the training and validation dataset. Identifying and controlling the error of ML predictions is necessary to avoid predictions that are inaccurate and detrimental to the structure search. MLPs that calculate prediction uncertainties more transparently help quantify the accuracy of both interpolative and extrapolative predictions. Additionally, knowledge of model uncertainty enables intelligent sampling of the search space to gather more data when utilized in an active learning scheme. Physical laws can also be incorporated into ML architectures to improve accuracy.[25,26]

Many MLPs and descriptors scale combinatorically or exponentially in cost with the number of unique elements being treated. This unfavorable computational scaling and the rapid growth of the number of distinct local environments with system size lessen the benefit of ML over quantum mechanical methods for complex reactive systems. Active learning strategies help minimize the computational cost of collecting information of relevant chemical environments and transfer learning can take advantage of pre-existing data to reduce training requirements. However, these methods do not reduce the number of relevant chemical environments themselves. Model architectures like SingleNN, which require fewer tunable parameters to consider many unique elements, help to reduce the scaling cost of ML predictions for complex systems. Different descriptor frameworks that are agnostic to elemental identity (e.g., representing local environments as expansions of electronic density)[27] can also improve ML model construction for datasets involving many unique elements and increase model transferability.

5.4 Final Remarks

In this chapter I have presented some natural extensions to the work shown in this dissertation. Still, there are many avenues of growth in the field of computational catalysis modeling that are set to be explored in the coming decades. This area of research continues to grow at a rapid pace, and the combination of clever algorithms and machine learning promises to accelerate our pace of catalyst design and discovery. My hope is that this work has provided a small stepping stone for other researchers in the field, and that our combined efforts may make a positive impact by solving our world's most pressing environmental challenges through advancements in engineering and technology.

5.5 References

(1) Zhai, H.; Alexandrova, A. N. Fluxionality of Catalytic Clusters: When It Matters and How to Address It. *ACS Catal.* **2017**, *7* (3), 1905–1911. https://doi.org/10.1021/acscatal.6b03243.

(2) Strong Electrostatic Adsorption of Metals onto Catalyst Supports. In *Catalyst preparation: Science and Engineering*; Regalbuto, J. R., Ed.; Taylor & Francis: Boca Raton, 2007.

(3) Shaikhutdinov, S. Strong Metal–Support Interaction and Reactivity of Ultrathin Oxide Films. *Catal Lett* **2018**, *148* (9), 2627–2635. https://doi.org/10.1007/s10562-018-2499-9.

(4) Li, S.; Xu, Y.; Chen, Y.; Li, W.; Lin, L.; Li, M.; Deng, Y.; Wang, X.; Ge, B.; Yang, C.; Yao, S.; Xie, J.; Li, Y.; Liu, X.; Ma, D. Tuning the Selectivity of Catalytic Carbon Dioxide Hydrogenation over Iridium/Cerium Oxide Catalysts with a Strong Metal–Support Interaction. *Angewandte Chemie International Edition* **2017**, *56* (36), 10761–10765. https://doi.org/10.1002/anie.201705002.

(5) Matsubu, J. C.; Zhang, S.; DeRita, L.; Marinkovic, N. S.; Chen, J. G.; Graham, G. W.; Pan, X.; Christopher, P. Adsorbate-Mediated Strong Metal–Support Interactions in Oxide-Supported Rh Catalysts. *Nature Chemistry* **2017**, *9* (2), 120–127. https://doi.org/10.1038/nchem.2607.

(6) Beck, A.; Huang, X.; Artiglia, L.; Zabilskiy, M.; Wang, X.; Rzepka, P.; Palagin, D.; Willinger, M.-G.; van Bokhoven, J. A. The Dynamics of Overlayer Formation on Catalyst Nanoparticles and Strong Metal-Support Interaction. *Nat Commun* **2020**, *11* (1), 3220. https://doi.org/10.1038/s41467-020-17070-2.

(7) Gao, J.; Sawant, K. J.; Miller, J. T.; Zeng, Z.; Zemlyanov, D.; Greeley, J. P. Structural and Chemical Transformations of Zinc Oxide Ultrathin Films on Pd(111) Surfaces. *ACS Appl. Mater. Interfaces* **2021**, *13* (29), 35113–35123. https://doi.org/10.1021/acsami.1c07510.

(8) Engelmann, Y.; van 't Veer, K.; Gorbanev, Y.; Neyts, E. C.; Schneider, W. F.; Bogaerts, A. Plasma Catalysis for Ammonia Synthesis: A Microkinetic Modeling Study on the Contributions of Eley–Rideal Reactions. *ACS Sustainable Chem. Eng.* **2021**, *9* (39), 13151–13163. https://doi.org/10.1021/acssuschemeng.1c02713.

(9) Mehta, P.; Barboun, P. M.; Engelmann, Y.; Go, D. B.; Bogaerts, A.; Schneider, W. F.; Hicks, J. C. Plasma-Catalytic Ammonia Synthesis beyond the Equilibrium Limit. *ACS Catal.* **2020**, *10* (12), 6726–6734. https://doi.org/10.1021/acscatal.0c00684.

(10) Bogaerts, A.; Tu, X.; Whitehead, J. C.; Centi, G.; Lefferts, L.; Guaitella, O.; Azzolina-Jury, F.; Kim, H.-H.; Murphy, A. B.; Schneider, W. F.; Nozaki, T.; Hicks, J. C.; Rousseau, A.; Thevenet, F.; Khacef, A.; Carreon, M. The 2020 Plasma Catalysis Roadmap. *J. Phys. D: Appl. Phys.* **2020**, *53* (44), 443001. https://doi.org/10.1088/1361-6463/ab9048.

(11) Tuckerman, M. E. Ab Initio Molecular Dynamics: Basic Concepts, Current Trends and Novel Applications. *J. Phys.: Condens. Matter* **2002**, *14* (50), R1297–R1355. https://doi.org/10.1088/0953-8984/14/50/202.

(12) Kresse, G.; Hafner, J. Ab Initio Molecular Dynamics for Liquid Metals. *Physical Review B* **1993**, *47* (1), 558–561.

(13) Deng, Y.; Roux, B. Computation of Binding Free Energy with Molecular Dynamics and Grand Canonical Monte Carlo Simulations. *J. Chem. Phys.* **2008**, *128* (11), 115103. https://doi.org/10.1063/1.2842080.

(14) Ramsahye, N. A.; Maurin, G.; Bourrelly, S.; Llewellyn, P. L.; Devic, T.; Serre, C.; Loiseau, T.; Ferey, G. Adsorption of CO2 in Metal Organic Frameworks of Different Metal Centres:

Grand Canonical Monte Carlo Simulations Compared to Experiments. *Adsorption* **2007**, *13* (5), 461–467. https://doi.org/10.1007/s10450-007-9025-5.
(15) Schlexer Lamoureux, P.; Winther, K. T.; Garrido Torres, J. A.; Streibel, V.; Zhao, M.; Bajdich, M.; Abild-Pedersen, F.; Bligaard, T. Machine Learning for Computational Heterogeneous Catalysis. *ChemCatChem* **2019**, *11* (16), 3581–3601. https://doi.org/10.1002/cctc.201900595.
(16) Zhai, H.; Alexandrova, A. N. Ensemble-Average Representation of Pt Clusters in Conditions of Catalysis Accessed through GPU Accelerated Deep Neural Network Fitting Global Optimization. *J. Chem. Theory Comput.* **2016**, *12* (12), 6213–6226. https://doi.org/10.1021/acs.jctc.6b00994.
(17) Tong, Q.; Gao, P.; Liu, H.; Xie, Y.; Lv, J.; Wang, Y.; Zhao, J. Combining Machine Learning Potential and Structure Prediction for Accelerated Materials Design and Discovery. *J. Phys. Chem. Lett.* **2020**, *11* (20), 8710–8720. https://doi.org/10.1021/acs.jpclett.0c02357.
(18) Yang, Y.; Jiménez-Negrón, O. A.; Kitchin, J. R. Machine-Learning Accelerated Geometry Optimization in Molecular Simulation. *J. Chem. Phys.* **2021**, *154* (23), 234704. https://doi.org/10.1063/5.0049665.
(19) Xu, J.; Cao, X.-M.; Hu, P. Perspective on Computational Reaction Prediction Using Machine Learning Methods in Heterogeneous Catalysis. *Phys. Chem. Chem. Phys.* **2021**, *23* (19), 11155–11179. https://doi.org/10.1039/D1CP01349A.
(20) Cai, C.; Wang, S.; Xu, Y.; Zhang, W.; Tang, K.; Ouyang, Q.; Lai, L.; Pei, J. Transfer Learning for Drug Discovery. *J. Med. Chem.* **2020**, *63* (16), 8683–8694. https://doi.org/10.1021/acs.jmedchem.9b02147.
(21) Hutchinson, M.; Antono, E.; Gibbons, B.; Paradiso, S.; Ling, J.; Meredig, B. Overcoming Data Scarcity with Transfer Learning. *arXiv:1711.05099* **2017**.
(22) Tran, K.; Ulissi, Z. W. Active Learning across Intermetallics to Guide Discovery of Electrocatalysts for CO2 Reduction and H2 Evolution. *Nat Catal* **2018**, *1* (9), 696–703. https://doi.org/10.1038/s41929-018-0142-1.
(23) Lookman, T.; Balachandran, P. V.; Xue, D.; Yuan, R. Active Learning in Materials Science with Emphasis on Adaptive Sampling Using Uncertainties for Targeted Design. *npj Comput Mater* **2019**, *5* (1), 21. https://doi.org/10.1038/s41524-019-0153-8.
(24) Sutton, C.; Boley, M.; Ghiringhelli, L. M.; Rupp, M.; Vreeken, J.; Scheffler, M. Identifying Domains of Applicability of Machine Learning Models for Materials Science. *Nat Commun* **2020**, *11* (1), 4428. https://doi.org/10.1038/s41467-020-17112-9.
(25) Xu, J.; Cao, X.-M.; Hu, P. Accelerating Metadynamics-Based Free-Energy Calculations with Adaptive Machine Learning Potentials. *J. Chem. Theory Comput.* **2021**, acs.jctc.1c00261. https://doi.org/10.1021/acs.jctc.1c00261.
(26) Shuaibi, M.; Sivakumar, S.; Chen, R. Q.; Ulissi, Z. W. Enabling Robust Offline Active Learning for Machine Learning Potentials Using Simple Physics-Based Priors. *Mach. Learn.: Sci. Technol.* **2021**, *2* (2), 025007. https://doi.org/10.1088/2632-2153/abcc44.
(27) Lei, X.; Medford, A. J. A Universal Framework for Featurization of Atomistic Systems. *arXiv:2102.02390 [physics]* **2021**.